University of California,
Irvine

Fast-ion D_α Measurements and Simulations in DIII-D

Dissertation

submitted in partial satisfaction of the requirements
for the degree of

Doctor of Philosophy

in Physics

by

Yadong Luo

Dissertation Committee:
Professor William W. Heidbrink, Chair
Professor Liu Chen
Professor Roger D. McWilliams

2007

The dissertation of Yadong Luo
is approved and is acceptable in quality
and form for publication on microfilm:

____

____

____

Committee Chair

University of California, Irvine
2007

Dedicated to my grandfather, Yuanchao Luo

Table of Contents

List of Figures

List of Tables

Acknowledgments

I could not have carried out this reseach without the help and advice of many people. First and foremost, I am deeply indebted to my thesis advisor, Dr. Bill Heidbrink, for his tremendous insight, assistance, and guidance throughout the entire project. He played a leading role in developing the simulation code. He devoted a large amount of time to data analysis and taught me to understand the physics. Whenever I needed help, he was always there and happy to help me whether or not it is his responsibility. I still remember that he drove down to DIII-D to move dozens of lead bricks for me. He also made my life at UCI much more enjoyable by inviting me to play soccer. We played together numerous times. I can proudly say that Ph.D. didn't wear me down and instead, I was in better shape than ever at the time of graduation.

Special thanks go to Keith Burrell, who is an expert pretty much on everything. Whenever I turned to him with questions, I always got answers right away. Among the various contributions he made on this project, he guided me in designing and assembling of the instrument.

I would like to thank David Kaplan for implementing the software and assisting me in running the instrument. Punit Gohil helped me settle down and get started in DIII-D . He trained me in running the water hoses for the cooling system and the fat cable bundles on the ceiling. He also contributed in the calibration. Wayne Solomon made useful changes on the simulation code and looked up many specifics regarding fibers, cameras, and calibrations for me. After I moved back to UC, Irvine, he played a major role in running the diagnostic. Neil brooks was very kind and made many helpful suggestions. Mickey Wade did the calibration in the vessel when there was a very high radiation dose. Ted Strait shielded me from the burdens of large facility bureaucracy. Rejean Boivin was always encouraging me and made all this happen. Bob Pinsker made significant contributions in doing the ICH experiments. Ron Bell provided insight on spectroscopy, especially spectrometers. I am also indebted to George Mckee, Bob Harvey, Jim Lynch, Jim Kulchar, Will Carrig, Dan Thomas, C.-L. Hiesh, Daniel Finkenthal, Rich Groebner and the entire DIII-D team for their assistance.

From Irvine, I would like to thank Emil Ruskov for his various contributions. He participated in the project from the very beginning. He set up CVS for the simulation code and made the code much more user friendly. He did an outstanding job of investigating the simulation sensitivity on plasma parameters. He served as a TRANSP expert and made numerous TRANSP runs and FIDA runs. Prof. Chen was on my dissertation committee and I learned tremendously from several indepth discussions with him. Prof. Lin's classes were very helpful. Prof. Mcwilliams was very kind and I benefited a lot from his big lab. He carefully read my thesis and made many comments, which greatly improved the thesis. I also appreciate the help I got from fellow graduate students Deyong Liu, Liangji Zhao, and Yang Zhang.

Last but certainly not least, I am extremely grateful for the support from my grandfather, my parents, my wonderful wife and from the rest of my family. For all your encouragement, care, love and prayers, thank you so much. I could never have done this without you.

This work was supported by the U.S. Department of Energy Subcontract No. SC-G903402 and Contract No. DE-FC02-04ER54698.

CURRICULUM VITAE
Yadong Luo

EDUCATION

2007 Ph.D. in Physics, University of California, Irvine

2003 M.S. in Physics, University of California, Irvine

2001 B.S. in Physics, University of Science and Technology of China, Hefei

AWARDS AND HONORS

2005 Faculty Endowed Fellowship

2002 Marco Vekic Memorial Award

PUBLICATIONS

W. W. Heidbrink, N. N. Gorelenkov, Y. Luo, M. A. Van Zeeland, R. B. White, M. E. Austin, K. H. Burrell, G. J. Kramer, M. A. Makowski, G. R. McKee, R. Nazikian, and the DIII-D team. "Central flattening of the fast-ion profile by Alfvén eigenmodes", Phys. Rev. Lett. (2007) submitted

Y. Luo, W. W. Heidbrink, K. H. Burrell, E. Ruskov, and W. M. Solomon, "Fast-ion D_α measurements and simulations in quiet plasmas". Phys. Plasmas (2007) submitted

W. W. Heidbrink, Y. Luo, K. H. Burrell, R. W. Harvey, R. I. Pinsker, and E. Ruskov. "Measurements of fast-ion acceleration at cyclotron harmonics using Balmer-alpha spectroscopy". Plasma Phys. Control. Fusion **49** (2007) 1457-1475

C.M. Greenfield, M. Murakami, A.M. Garofalo, E.J. Doyle, J.R. Ferron, M.R. Wade, M.E. Austin, S.L. Allen, K.H. Burrell, T.A. Casper, J.C. DeBoo, P. Gohil, I.A. Gorelov, R.J. Groebner, W.W. Heidbrink, A.W. Hyatt, G.L. Jackson, R.J. Jayakumar, K. Kajiwara, C.E. Kessel, J.E. Kinsey, J.Y. Kim, R.J. La Haye, L.L. Lao, J. Lohr, T.C. Luce, Y. Luo, M.A. Makowski, D. Mazon, G.R. McKee, M. Okabayashi, T.H. Osborne, C.C. Petty, T.W. Petrie, R.I. Pinsker, R. Prater, P.A. Politzer, H. Reimerdes, T.L. Rhodes, A.C.C.

Sips, J.T. Scoville, W.M. Solomon, G.M. Staebler, H.E. St. John, E.J. Strait, T.S. Taylor, A.D. Turnbull, M.A. Van Zeeland, G. Wang, W.P. West, L. Zeng and the DIII-D Team. "Progress towards high-performance steady-state operation on DIII-D". Fusion Engineering and Design **81** (2006) 2807-2815

Y. Luo, W. W. Heidbrink, K. H. Burrell, D. H. Kaplan, and P. Gohil. "Measurement of the D_α spectrum produced by fast ions in DIII-D". Rev. Sci. Instrum. **78** (2007) 033505

W. W. Heidbrink, R. E. Bell, Y. Luo, and W. Solomon. "Fast-ion D-alpha diagnostic for NSTX". Rev. Sci. Instrum. **77** (2006) 10F120

R.I. Pinsker, M. Porkolab, W.W. Heidbrink, Y. Luo, C.C. Petty, R. Prater, M. Choi, D.A. Schaffner, F.W. Baity, E. Fredd, J.C. Hosea, R.W. Harvey, A.P. Smirnov, M. Murakami and M.A. Van Zeeland. "Absorption of fast waves at moderate to high ion cyclotron harmonics on DIII-D". Nucl. Fusion **46** (2006) S416-S424

M. Murakami, M. R. Wade, C. M. Greenfield, T. C. Luce, J. R. Ferron, H. E. St. John, J. C. DeBoo, W. W. Heidbrink, Y. Luo, M. A. Makowski, T. H. Osborne, C. C. Petty, P. A. Politzer, S. L. Allen, M. E. Austin, K. H. Burrell, T. A. Casper, E. J. Doyle, A. M. Garofalo, P. Gohil, I. A. Gorelov, R. J. Groebner, A. W. Hyatt, R. J. Jayakumar, K. Kajiwara, C. E. Kessel, J. E. Kinsey, R. J. La Haye, L. L. Lao, A. W. Leonard, J. Lohr, T. W. Petrie, R. I. Pinsker, R. Prater, T. L. Rhodes, A. C. C. Sips, G. M. Staebler, T. S. Taylor, M. A. Vanzeeland, G. Wang, W. P. West, L. Zeng, and the DIII-D Team. "Progress toward noninductive, high beta conditions in DIII-D". Phys. Plasmas **13** (2006) 056106

M. E. Austin, K. H. Burrell, R. E. Waltz, K. W. Gentle, P. Gohil, C. M. Greenfield, R. J. Groebner, W. W. Heidbrink, Y. Luo, J. E. Kinsey, M. A. Makowski, G. R. McKee, R. Nazikian, C. C. Petty, R. Prater, T. L. Rhodes, M. W. Shafer, and M. A. Van Zeeland. "Core barrier formation near integer q surfaces in DIII-D". Phys. Plasmas **13** (2006) 082502

W. W. Heidbrink, K. H. Burrell, Y. Luo, N. A. Pablant, and E. Ruskov. "Hydrogenic fast-ion diagnostic using Balmer-alpha light". Plasma Phys. Control. Fusion **46** (2004) 1855-1875

Y. Luo, W. W. Heidbrink, and K. H. Burrel. "Design of a D-alpha beam-ion profile diagnostic". Rev. Sci. Instrum. **75** (2004) 3468

W. W. Heidbrink, E. Fredrickson, N. N. Gorelenkov, A. W. Hyatt, G. Kramer, and Y. Luo. "An Alfvén eigenmode similarity experiment". Plasma Phys. Control. Fusion **45** (2003) 983-997

INVITED PRESENTATION

"Measurement of the fast-ion distribution function utilizing D_α spectroscopy in DIII-D"
16th Topical Conference on High-Temperature Plasma Diagnostic
Williamsburg, Virginia 2006

Abstract of the Dissertation

Fast-ion D_α Measurements and Simulations in DIII-D

By

Yadong Luo

Doctor of Philosophy in Physics

University of California, Irvine, 2007

Professor William W. Heidbrink, Chair

The fast-ion D_α diagnostic measures the Doppler-shifted D_α light emitted by neutralized fast ions. For a favorable viewing geometry, the bright interferences from beam neutrals, halo neutrals, and edge neutrals span over a small wavelength range around the D_α rest wavelength and are blocked by a vertical bar at the exit focal plane of the spectrometer. Background subtraction and fitting techniques eliminate various contaminants in the spectrum. Fast-ion data are acquired with a time evolution of ~ 1 ms, spatial resolution of ~ 5 cm, and energy resolution of ~ 10 keV. A weighted Monte Carlo simulation code models the fast-ion D_α spectra based on the fast-ion distribution function from other sources. In quiet plasmas, the spectral shape is in excellent agreement and absolute magnitude also has reasonable agreement. The fast-ion D_α signal has the expected dependencies on plasma and neutral beam parameters. The neutral particle diagnostic and neutron diagnostic

corroborate the fast-ion D_α measurements. The relative spatial profile is in agreement with the simulated profile based on the fast-ion distribution function from the TRANSP analysis code. During ion cyclotron heating, fast ions with high perpendicular energy are accelerated, while those with low perpendicular energy are barely affected. The spatial profile is compared with the simulated profiles based on the fast-ion distribution functions from the CQL Fokker-Planck code. In discharges with Alfvén instabilities, both the spatial profile and spectral shape suggests that fast ions are redistributed. The flattened fast-ion D_α profile is in agreement with the fast-ion pressure profile.

Chapter 1

Introduction

1.1 Fusion energy

In a world where energy needs are rapidly growing beyond the available supply capacity, scientists from around the world are working to harness fusion energy, the power of the sun and stars and use this resource to meet the planet's rising demands. To produce fusion energy, the fuels must be heated to temperatures of 100 million $^{\circ}C$ and held at high pressure long enough. Confining fuels at such a high temperature is challenging, yet accomplishable in three different ways [1]. The sun confines the fuels by gravity. The equatorial surface gravity of the sun is 28 times as strong as that of the Earth. Unfortunately, this gravity technique does not work on the "tiny" Earth. Inertial confinement fusion uses powerful energy beams, such as lasers, to compress and heat the fuels. Magnetic confinement fusion uses strong magnetic fields to confine the fuels, heated by ohmic heating and other means. The problem of producing useful fusion energy on Earth is sufficiently difficult that in over 50 years of research the only man-made fusion device which had produced more energy than it consumed is the hydrogen bomb. Among various fusion reactions, the fusion of deuterium and tritium (Eq. 1.1) is the most promising. It yields 17.6 MeV of energy, but requires a relatively low temperature of 20 million $^{\circ}C$ to overcome the Coulomb barrier. The deuterium fuel can be derived from water which is abundant and available everywhere. Tritium can be produced from lithium, which is plentiful in the earth's crust.

$$D + T \Rightarrow \alpha(3.5\ MeV) + n(14.1\ MeV) \tag{1.1}$$

1.2 Tokamak

The tokamak [2] is one of several types of magnetic confinement devices and the leading candidate for producing fusion energy, reflected in the design of the next generation ITER device. It is a doughnut-shaped machine producing a toroidal magnetic field for confining a plasma. It was invented in the 1950s by Soviet physicists Igor Yevgenyevich Tamm and Andrei Sakharov. The tokamak is characterized by azimuthal symmetry and the use of the plasma current to generate the helical component of the magnetic field necessary for stable equilibrium.

In an operating fusion reactor, part of the energy released will serve to maintain the plasma temperature as fresh deuterium and tritium are introduced. However, in the startup of a reactor, the plasma will have to be heated by other means to its operating temperature of greater than 10 keV. Since the plasma is an electrical conductor, it is possible to heat the plasma by inducing a current through it. The heating caused by the induced current is called ohmic heating. The heat generated depends on the resistance of the plasma and the current. But as the plasma temperature rises, the resistance decreases and ohmic heating becomes less effective. To obtain high temperatures, additional heating methods must be used. Neutral plasma heating and radio-frequency heating are two of the main auxilliary heating methods in tokamaks. Neutral beam injection involves the introduction of high energy atoms into the ohmically-heated, magnetically-confined plasma. The atoms are ionized as they pass through the plasma and are trapped by the magnetic field. The energetic ions then transfer part of their energy to the plasma particles in repeated collisions, increasing the plasma temperature. Radio-frequency heating utilizes high-frequency electromagnetic waves generated by gyrotrons. If the waves have the correct frequency and polarization, their energy can be transfered to the charged particles in the plasma, which in turn collide with other plasma particles, thus increasing the temperature of the bulk plasma. Various RF heating techniques exist including electron cyclotron heating (ECH) and ion cyclotron heating (ICH).

1.3 DIII-D

The experimental research presented in this thesis was conducted on the DIII-D tokamak located at the DIII-D National Fusion Facility in San Diego, California. This section describes the facility as it was in 2004 and 2005, when the data in this thesis were taken. DIII-D is a non-circular cross-section tokamak with major radius $R_0 = 1.66$ m, minor radius $a = 0.66$ m, and plasma chamber elongation of 2.1 with toroidal magnetic field of up to 2.2 T at R_0 [3]. The tokamak operates in a wide range of configurations including single null and double dull divertors. The maximum plasma current I_p is presently 2.5 MA. To heat the plasma above the ohmic level ($\gtrsim$1.0 keV), there are seven neutral beams, a 110 GHz ECH system, and a Fast Wave (FW) system (60-120 MHz). The beams inject 45-81 keV deuterium beam ions in the direction of the plasma current at tangency radii (the distance between the center and the beam centerline) of 0.76 m (for the so-called “right” sources) and 1.15 m (for the “left” sources) providing up to 20 MW of heating power. Typically, one FW transmitter couples 0.7-1.0 MW at 60 MHz into plasmas.

The other FW transmitters couple up to 2 MW of power at 113-117 MHz. The 110 GHz ECH system is powered by a mixture of short pulse ($\sim$ 2 s) gyrotrons from Gycom and long pulse gyrotrons ($\sim$ 10 s) from CPI providing a maxium power of 4.5 MW. Table 1.1 lists the primary parameters for DIII-D .

Table 1.1: Plasma parameters of the DIII-D tokamak as of May 2005.

Parameter	DIII-D Capability
Major Radius (R)	1.67 m
Minor Radius (a)	$\lesssim$0.67 m
Vertical Elongation (κ)	1.0-2.6
Aspect Ratio (ϵ)	2.5-5.3
Toroidal Field (B_T)	0.6-2.2 T
Plasma Current (I_p)	$\lesssim$2.5 MA
Ohmic Heating Power (P_{ohm})	$\lesssim$1.0 MW
Neutral Beam Power (P_{inj})	$\lesssim$20 MW
ICH Power (P_{ICH})	$\lesssim$3 MW
ECH Power (P_{ECH})	$\lesssim$4.5 MW
Electron Temperature ($T_e(0)$)	$\lesssim$6 keV
Electron Density (n_e)	$\lesssim 1.0 \times 10^{20}\ cm^{-3}$
Ion Temperature ($T_i(0)$)	$\lesssim$17 keV

The DIII-D tokamak has long been recognized as being one of the best-diagnosed magnetic fusion experments [4]. Among over 50 individual systems, many of them have been utilized for this work. Electron Cyclotron Emission (ECE) [5] and Thomson scattering [6] measure electron temperature. Thomson scattering and CO_2 interferometers [7] measure electron density. Charge exchange recombination (CER) [8] spectroscopy measures ion temperature, rotation velocity, and carbon density. We usually assume that carbon is the dominant impurity species. A survey spectrometer measures impurity concentration. Visible filter scopes measure edge

D_α signal monitoring edge localized modes (ELMs). An extensive suite of techniques can provide fluctuation measurements, including ECE, Beam Emission Spectroscopy (BES) [9], CO_2 interferometer, reflectometer [10], and Mirnov coils. Motional Stark polarimeter (MSE) [11] measure plasma current profiles. The DIII-D fast-ion diagnostics are discussed in §1.5.

A set of software is used regularly for this project. TRANSP [12] is a time-dependent transport analysis code for tomamak experiment. It classically calculates fast-ion distribution functions, which provide the input for the fast-ion D_α (FIDA) simulation code in quiet plasmas. GAProfiles makes spline fits to experimental profile data that are required for TRANSP and the FIDA simulation data. EFIT [13] is an equilibrium code that translates measurements from plasma diagnostics into useful information like plasma geometry, stored energy, and current profiles.

1.4 Fast ions

A typical tokamak contains thermal electrons, thermal ions, and fast ions that have energies much higher than the thermal ion temperature. The velocity distribution function of thermal particles is described by a shifted Maxwellian distribution function characterized by a rotation velocity $\mathbf{V}_j$, a temperature T_j, and a density n_j. Fast ions are not in thermal equilibrium and they do not conform to a Maxwellian distribution [14]. The fast ion distribution function is a general function of $f(\mathbf{v}, \mathbf{r}, t)$. In analytical modeling, a slowing-down distribution is often employed for some types of fast ions [15]. In tokamaks, fast ions are generated by fusion reactions, by neutral beam injection, and by RF acceleration [14]. Fast ions created in nuclear reactions have a well defined initial energy. The spatial distribution is centrally peaked since both the density and the temperature peak on axis. The angular distribution is nearly isotropic. Rf acceleration of fast ions occurs in the perpendicular direction around the resonance layer. Hydrogenic fast ions created by neutral beam injection have three energy components (known as the full energy, the half energy, and the third energy components, respectively). The initial pitch angle depends on the injection angle of neutral beams.

Diagnosis of the fast-ion population is important because the fast ions are often a major source of energy, momentum, and particles for the plasma. Moreover, the fast-ion pressure and driven current can have a significant impact on macroscopic stability properties. Although dilute populations of fast ions often behave classically, intense populations can drive instabilities that redistribute or expel the fast ions from the plasma [14]. This is often the case in experiments in the DIII-D tokamak, where anomalous fast-ion diffusion rates of approximately 0.3 m^2/s are inferred commonly in discharges with neutral beam injection [16].

1.5 Existing fast-ion diagnostics

Table 1.2 compares existing fast-ion diagnostics in use worldwide with the new diagnostic technique discussed in this thesis. Neutrons, 3 MeV protons, and fusion gammas are fusion products. It is often desirable to distinguish thermonuclear reactions from the beam-plasma and beam-beam reactions produced by fast ions [14]. The lost ion detector, as its name suggests, measures escaping fast ions from the plasma. The neutral particle analyzers (NPA) measure neutralized fast ions (reneutrals) by charge exchange reaction. The collective Thomson scattering (CTS)

Table 1.2: Comparisons of fast-ion diagnostics

Technique	**Velocity resolution**	**Approximate achieved spatial resolution**	**Approximate achieved temporal resolution**
Neutrons	Weights high energies	$\gtrsim$10 cm chord averaged	$\sim 10\ \mu s$
3 MeV protons	Weights high energies	$\gtrsim$10 cm orbit averaged	$\sim$ 1 ms
Fusion gammas	Weights high energies	$\sim$ 5 cm chord averaged	$\lesssim$10 ms
Lost ions	Good	Lost ions only	$\sim 1\ \mu s$
Neutrals	Excellent	Depends on neutrals	$\sim 10\ \mu s$
Scattering	Good	$\sim$ 10 cm	$\sim$ 1 ms
FIDA	Good	$\sim$ 1 cm	$\sim$ 1 ms

diagnostic [17] measures the scattered wave by electrons surrounding fast ions. High power millimeter-waves are required for this diagnostic.

Several of these diagnostics were already implemented on DIII-D (Fig. 1.1). A plastic scintillator that is cross-calibrated to an absolutely-calibrated fission counter measures the volume-averaged 2.5 MeV neutron rate [18]. Spatially-resolved measurements of the fast ions are obtained in two ways. A compact electrostatic neutral particle analyzer (NPA) measures the active charge exchange signal at R=1.95 m [19]; the analyzer detects perpendicular 50-keV neutrals from a vertical volume that is determined by the vertical extent of the modulated neutral beam (Fig. 6.1). The second spatially-resolved diagnostic relies on motional Stark effect (MSE) [20] measurements of the internal magnetic field. The profile of the total plasma pressure p_{tot} is obtained from EFIT [13] reconstructions of the MHD equilibrium that are consistent with the MSE data, with magnetics data, and with

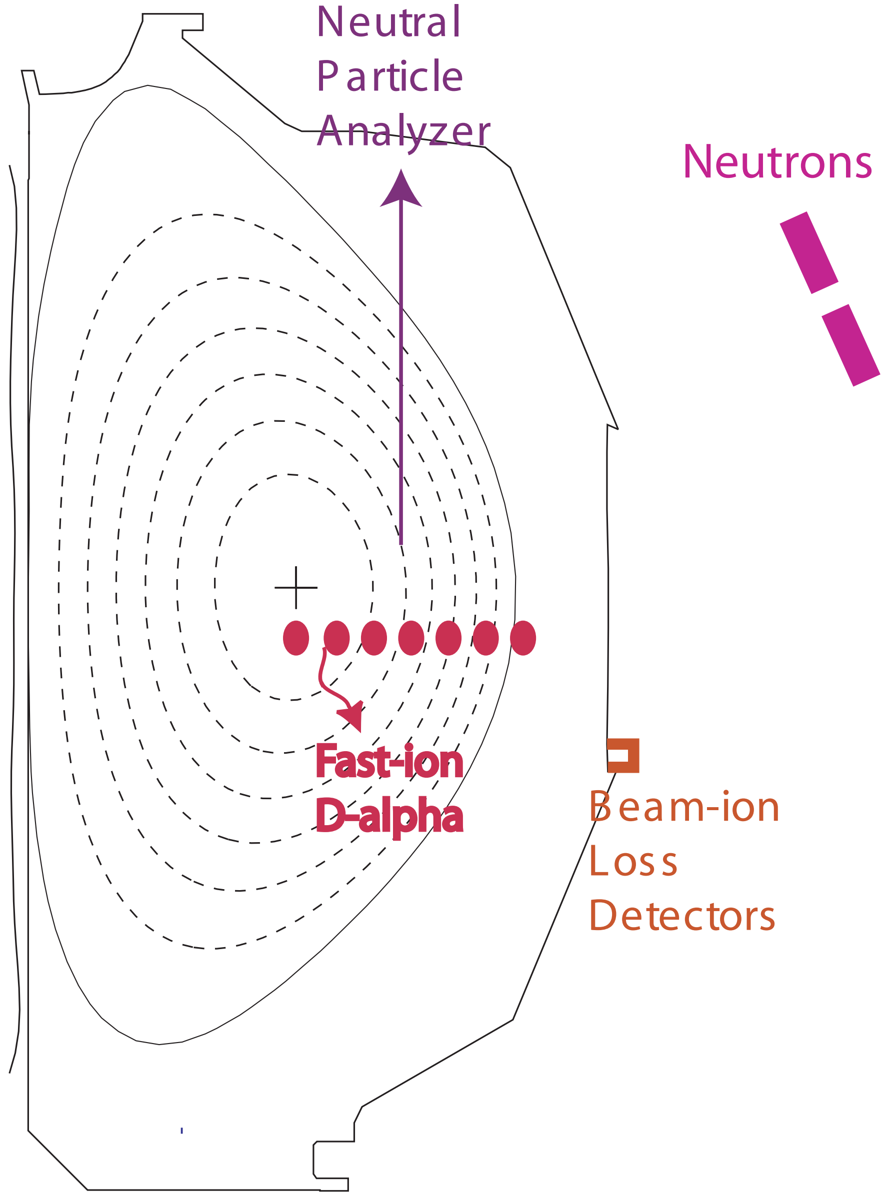

Figure 1.1: The DIII-D fast-ion diagnostics shown in the vertical cross section.

isotherms of the electron temperature as measured by an electron cyclotron emission (ECE) [5] diagnostic. The thermal pressure p_{th} from T_e [5, 6], n_e [6, 7], T_i, and carbon density measurements is subtracted from the MHD pressure profile to obtain the fast-ion pressure profile p_f [21, 22]. With the assumption that the carbon and deuterium temperatures are both T_i and that the plasma is quasineutral with carbon the dominant impurity, the fast-ion pressure p_f is

$$p_f = p - n_e T_e - (n_e - 6n_C)T_i - n_C T_i, \tag{1.2}$$

where p is the total pressure from EFIT and n_C is the carbon density. The uncertainty in fast-ion pressure δp_f is

$$\delta p_f = [(\delta p)^2 + (T_e + T_i)^2(\delta n_e)^2 + n_e^2(\delta T_e^2 + \delta T_i^2) + 25n_C^2 \delta T_i^2 + 25T_i^2 \delta n_C^2]^{1/2}. \tag{1.3}$$

The uncertainty is affected by the uncertainty in the total pressure and the uncertainty in thermal pressure. The uncertainty in p_{th} is readily computed by propagating the estimated random errors in the thermal density and temperature measurements. The uncertainty in p_{tot} is more difficult to quantify because systematic errors in the EFIT equilibrium construction exceed the errors associated with MSE, ECE, and magnetics measurement errors. The terms involving δp and δn_e usually are dominant. For the cases shown in this thesis, the absolute uncertainty in the fast-ion pressure is $\sim 20\%$ (with δp_{tot} and δn_e making the dominant contributions), while the relative uncertainty when comparing the profiles with and without ICH (Chapter 6) is $\sim 10\%$. The primary fast-ion diagnostic is FIDA, which is discussed in this thesis.

1.6 Thesis organization

This thesis consists of eight chapters. Chapter 1 serves as a brief introduction to the background. The first section of Chapter 2 discusses the diagnostic concept and challenges, which were published by Heidbrink et al. in 2004 in Plasma Physics and Controlled Fusion [23]. The second section of chapter 2 describes the instruments. The initial design of the instruments was published by Luo et al. in 2004 in Review of Scientific Instruments [24]. In 2007, Luo et al. published a paper in Review of Scientific Instruments [25] with detailed discussion of the instrument. Chapter 3 presents the data analysis procedure, signal level, and signal to noise issues [25]. Chapter 4 introduces the simulation code [23],which predicts the FIDA spectra based on existing fast-ion distributions. The sensitivity study results of simulated FIDA signal on plasma parameters were published by Luo et al. in 2007 in Physics of Plasmas [26]. Chapter 5, 6, and 7 presents FIDA measurements in quiet plasmas, during high harmonic ICH, and in plasmas with instabilities, respectively. The quiet plasma results were published by Luo et al. [26]. The ICH results were published by Heidbrink et al. in 2007 in Plasma Physics and Controlled Fusion [27]. The results with instabilities have been submitted by Heidbrink et al. to Physical Review Letters [28]. Finally, the thesis concludes with a chapter (Chapter 8) devoted to summaries and future work.

Chapter 2

FIDA diagnostic

2.1 Diagnostic concept

In neutral-beam-heated tokamak plasmas, as deuterium fast ions circulate the device, they can pass through a neutral beam, where some fast ions neutralize by charge exchanging with the injected neutrals or halo neutrals (warm neutrals around the neutral beam). Some of the reneutrals (neutralized fast ions) are in excited states. After traveling a distance in a straight line, the excited state may decay by emitting a photon,

$$D^0 + D^+ \Rightarrow D^+ + D^{0*} \Rightarrow D^+ + D^0 + \gamma. \tag{2.1}$$

D_α light, which is the transition from the $n = 3$ to $n = 2$ energy level, has a rest wavelength of 656.1 nm. It is visible and can easily be measured with a standard spectroscopic system. The Doppler shift of the D_α line depends on the velocity component of the reneutral along the viewing line at the time of emission. As a result, a particular wavelength in the spectrum corresponds to fast ions with a particular velocity component along the viewing line and arbitrary velocity components in the other orthogonal directions.

Figure 2.1(a) illustrates the relevant atomic processes. The first reaction is the charge exchange reaction with an injected or halo neutral that converts a fast ion

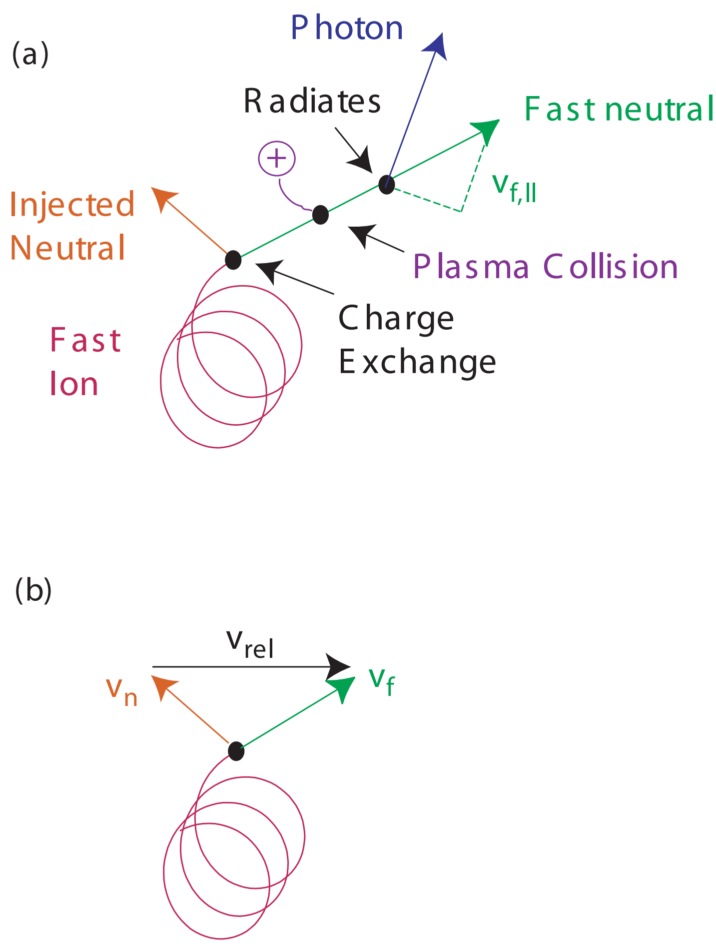

Figure 2.1: (a) Three types of atomic processes in the emission of a photon by a fast ion. The first reaction is a charge-transfer event between an orbiting fast ion and an injected neutral or halo neutral. The second set of reactions are changes in energy levels caused by collisions between the reneutrals and the plasma. The third reaction is the atomic transition that produces the measured photon. The Doppler shift of this photon is determined by the component of the fast-ion velocity in the direction of observation, $v_{f,\|}$. (b) The probability of the initial charge-exchange reaction depends on the relative velocity between the fast ion and the injected neutral, $v_{rel} = |\mathbf{v}_f - \mathbf{v}_n|$.

into a reneutral. After a reneutral is created, its energy level can change. Many processes are involved: collisional excitation, deexcitation, and ionization with electrons, deuterons, and impurities, as well as radiative transitions. The transition of interest is the $n = 3 \rightarrow 2$ radiative transition.

The detection of Balmer-alpha light is widely applied. Balmer-alpha light from the plasma edge is measured on virtually all magnetic fusion devices as a monitor of plasma recycling and transport and to determine the relative abundances of different hydrogenic species [29]. The spatial profile of Balmer-alpha light from injected neutrals is used to measure the deposition of the neutral beams in the plasma [30, 31], the spectrum is used to detect magnetic [32] and electric fields [33, 34] through Stark splitting, and fluctuations in the emission are related to fluctuations in the electron density [35]. Balmer-alpha light from neutralized thermal ions by charging exchange with an injected beam provides information on the local ion temperature [36, 37] and deuterium density [31, 38]. In both astronomy and plasma physics Balmer-alpha radiation is also known as H_α light or, in the case of deuterium atoms, D_α .

Conceptually, the use of D_α light to diagnose a fast deuterium population is similar to the diagnosis of fast helium populations using charge exchange recombination spectroscopy [39]. Fast helium populations during ^{3}He neutral beam injection were measured on JET [40, 41]. Alpha particles produced in deuterium-tritium reactions were measured on the Tokamak Fusion Test Reactor (TFTR) [42, 43].

The intrinsic spatial resolution of this technique is determined by the mean-free path of the reneutrals. Note that the situation is different than for charge-exchange recombination spectroscopy of ions with $Z > 1$ [44]. An impurity ion with $Z > 1$ that gains an electron remains charged and continues to orbit in the magnetic field. Ions can travel on curved paths from one neutral beam source into a sightline that views a different source [44] (the so-called "plume" effect). In contrast, a reneutral travels in a straight line until it is reionized or lost. Since reneutrals from distant sources are unconfined they tend to disperse rapidly.

Figure 2.2 shows a simulation of the expected signal from a monoenergetic population of 80-keV/amu fast ions with a uniform velocity distribution in pitch that are randomly launched from one cell. The contours are displayed in the plane perpendicular to the injected neutral beam. The intensity from this localized source decreases rapidly with distance from the source. Three factors affect the spatial resolution. First, the emission intensity from an isotropic source of unattenuated, steadily-radiating particles decreases as the square of the radius r from the source. The decrease with distance shown in Fig. 2.2 is faster than r^{-2}, however, because the radiating fast neutrals can be ionized through collisions. The mean-free path for reionization is comparable to the attenuation length for injected neutrals, i.e., ~ 30 cm for a typical DIII-D plasma. A more important length is the mean-free path associated with the lifetime of the $n = 3$ state, $v_f \tau_{3\to2} \simeq 6.1$ cm ($v_f \simeq 2.8 \times 10^6$ m/s, $\tau_{3\to2} \simeq 2.2 \times 10^{-8}$ s). The actual mean-free path in the plasma is shorter than this vacuum value because the effective lifetime of the $n = 3$ state is shortened by collisions. Consequently, the intrinsic spatial resolution is ~ 1 cm. Some neutrals that are reexcited to the $n = 3$ state contribute a weak signal at the 0.1% level out to distances of 20-50 cm, however.

It should be noted that, from the standpoint of atomic physics, the Lyman alpha

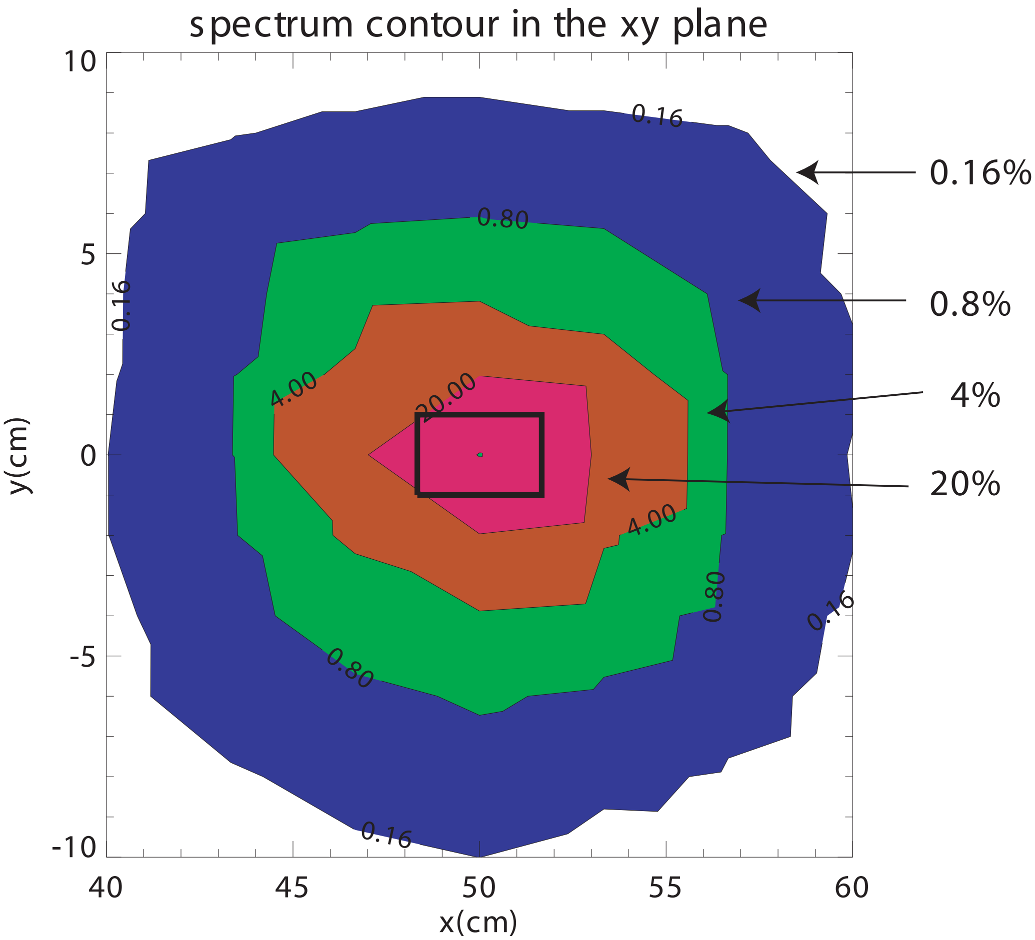

Figure 2.2: Spatial distribution of the D_α light produced by a monoenergetic distribution of 80 keV/amu fast ions with uniform pitch that originate randomly in a single cell (rectangular box at center). A plane perpendicular to the direction of the injected source is shown. Contours of constant emission are given.

transition is superior to the Balmer alpha transition. The lifetime is shorter, so $v_f \tau_{2\to 1} = 0.6$ cm in vacuum. Moreover, the charge exchange cross section from the ground state to the $n = 2$ state is much larger than to the $n = 3$ state, so the line is brighter and uncertainties in the excited state fractions [45] have a smaller impact on the interpretation of the signal. The advantage of the Balmer alpha transition is purely technical: although it is is possible to design a high throughput ultraviolet diagnostic [46], detection is simpler in the visible.

For spectroscopic measurements of either fast helium ions or fast hydrogenic ions, avoiding the bright emission from other sources is a major challenge. There are several populations of hydrogenic neutrals in a typical tokamak plasma [47] (Fig. 2.3). Near the plasma edge, there are populations of relatively cold neutrals from the walls and divertor that are excited in the plasma periphery. These edge neutrals radiate brightly near the unshifted wavelength of the Balmer-alpha transition (at 656.1 nm for D_α). The penetration distance of edge neutrals into the bulk plasma is approximately the geometric mean of the mean-free path for ionization and the mean-free path for charge exchange, which is only a few centimeters in a typical tokamak.

Neutrals injected from neutral beam lines are the second major population. The velocities of these neutrals are determined by the accelerating grids of the neutral beam source. There are three discrete energies: the neutrals with the full acceleration voltage, neutrals with one-half of the acceleration voltage, and neutrals with one-third of the acceleration voltage. The small divergence of the neutral beam source implies that both the direction of the velocity vector and the spatial extent of the injected neutrals is well-defined. Because of their large velocity (2.8×10^6 m/s

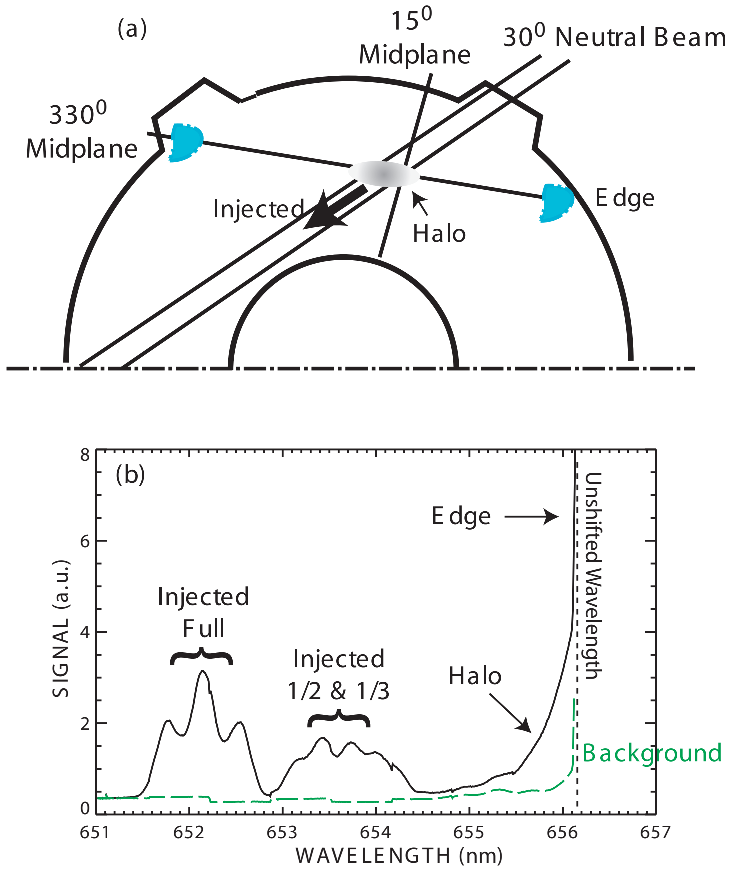

Figure 2.3: (a) Plan view of the DIII-D tokamak showing the modulated neutral beam source and the two sightlines for the data in this paper. Injected neutrals are in the beam "footprint," warm halo neutrals are in a cloud around the injected beam, and cold edge neutrals are near the walls of the chamber. (b) Spectrum for the fiber that views the 30° modulated beam from the 330° midplane port when the beam is on (black) and off (dashed). The contributions to the spectrum of the injected, halo, and edge neutrals are indicated.

for an 80-keV deuteron), the Doppler shift of the D_α emission can be as large as 6 nm. In addition to the Doppler shift, there also is Stark splitting of the line associated with both the motional $\mathbf{v} \times \mathbf{B}$ Stark effect and with plasma electric fields. This splitting accounts for the ~ 1 nm spread of the three peaks in the full-energy D_α line in Fig. 2.3.

The injected neutrals ionize through electron-impact ionization with plasma electrons or through charge exchange with plasma ions. Because of the large electron-ion mass difference, in a charge exchange ("charge transfer") event with a deuterium ion, the velocities of the ion barely change [15], so the energetic injected neutral generates a neutral with the velocity of the thermal plasma ion. These warm neutrals can radiate promptly and they generally undergo several subsequent charge-exchange reactions before being ionized by electron impact. A warm, "halo" neutral population forms around the injected beam. The velocity distribution of this population is approximately the local velocity distribution of the plasma ions. For an ion temperature of $T_i = 5$ keV, the resulting Doppler shift of the D_α line is approximately 1.5 nm.

Upon ionization, injected neutrals form a population of fast ions. These fast ions circulate around the torus on orbits that are determined by their velocity and the confining magnetic field. On a longer timescale, Coulomb collisions with the plasma cause gradual deceleration and spreading of the velocity distribution. Because the duration of beam injection and the deceleration time are very long compared to characteristic orbital timescales, the toroidal dependence is lost and an axisymmetric, supra-thermal distribution f_f of fast ions is created that depends on four variables: the fast-ion energy E, the projection of the velocity vector onto the magnetic field, $v_\parallel/v$ (also called the "pitch"), and the radial and poloidal positions $\mathbf{r}$. When these fast ions orbit through an injected neutral beam, a small fraction of them undergo a charge-exchange reaction and become a deuterium atom. The goal of this technique is to extract information about f_f from the D_α light emitted by these atoms.

The spectrum in Fig. 2.3 highlights the difficulties with a naive implementation of this concept. These data are from a fiber that views a neutral beam source "tangentially" in the midplane (shown in Fig. 2.3(a)). Injected neutrals are traveling toward the fiber so the radiation is blue-shifted. The bright contributions from edge and halo neutrals on the blue-shifted side of the central peak are also evident. For these plasma conditions, the fast-ion population is traveling primarily in the direction of the injected beam with a broad distribution of energies and velocities, so a broad blue-shifted fast-ion "line" that spans the entire abscissa is expected. This line is relatively weak, however. The fast-ion signal is proportional to the fast-ion density n_f, while the halo signal is proportional to the thermal plasma density n_i. As a crude estimate of the spectral intensity $dI/d\lambda$, the ratio of fast-ion to halo signal is roughly $(n_f/n_i)\sqrt{T_i/E} \sim 10^{-3}$. This implies that the expected signal is smaller than typical backgrounds from bremsstrahlung and impurity radiation. Accurate background subtraction is essential for the success of this concept. Even with accurate background subtraction, detection of a fast-ion signal is problematic for the geometry shown in Fig. 2.3.

Fortunately, there are more favorable geometries. Figure 2.4 illustrates the situation for a fiber located above the heating beam. Because the injected neutrals travel horizontally, this geometry eliminates their Doppler shift. In contrast, the fast ions gyrate vertically in the magnetic field due to the perpendicular component of their velocity. They travel down during half of their cyclotron orbit and up during the other half, so a population of fast ions produces a spectrum with red- and blue-shifted wings. This effect is most pronounced for the idealized, monoenergetic distribution shown in Fig. 2.4 but the basic effect is present for more realistic distributions. With accurate background subtraction, the signal from fast ions is detectable.

Removing the background from visible bremsstrahlung and scattering is another challenge for a FIDA measurement. Visible bremsstrahlung spreads uniformly over the entire range of interest and scales as n_e^2. On the other hand, the FIDA signal decreases with increasing n_e. In a high density discharge in DIII-D, visible bremsstrahlung could be an order of magnitude stronger than the FIDA signal. Even in a typical low density discharge, the visible bremsstrahlung and FIDA signals are comparable. Thus, it is essential to do accurate background subtraction. This is achieved through modulation of the injected neutral beam in a steady plasma, which can be done routinely in DIII-D. In a transient plasma, changes in background must be monitored independently, as discussed in §3.1.

The relationship between the measured spectrum and the fast-ion distribution function is complicated by the energy dependence of the charge-exchange cross section. These effects have been the topic of extensive study within the context of charge exchange recombination spectroscopy; see, for example, Refs. [48, 49]. Ideally, an inversion algorithm would exist that relates the measured spectrum $dI/d\lambda$ to the desired quantity, the fast-ion distribution function $f_f(E, v_\parallel/v)$; it would be particularly convenient if the signal was linearly proportional to the

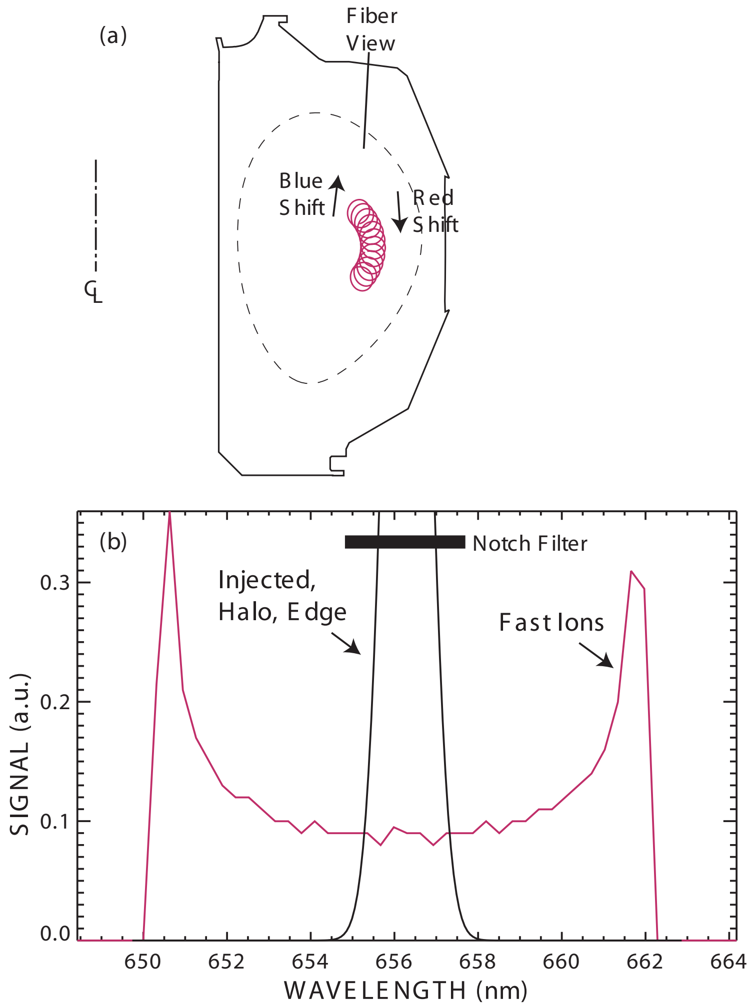

Figure 2.4: (a) Elevation of the DIII-D tokamak showing a typical plasma shape (dotted line) and the projection of a portion of a fast-ion orbit. If the fast ion neutralizes when it is gyrating up toward the fiber there is a blue shift; if it is gyrating down there is a red shift. (b) Spectrum produced by a monoenergetic population of perpendicular 80-keV deuterons, as calculated by a simple model that neglects atomic physics. For this geometry, the linewidths of the injected, halo, and edge neutrals are only a few nanometers.

fast-ion density but, unfortunately, this is not generally the case. Figure 2.5(a) shows the origin of the complexity. The neutralization rate is a strong function of the relative energy between the fast ion and the injected neutral, peaking at ~ 27 keV/amu. This implies that some velocities in the fast-ion distribution function are more likely to neutralize and contribute to the spectrum. The signal depends on two distinct pairs of velocities. The first pair is the relative speed between the injected neutral and the fast ion v_{rel} (Fig. 2.1(b)), which determines the probability of neutralization. The second pair is the fast-ion velocity and the velocity vector of the emitted photon, since the component of the fast-ion velocity in the direction of observation $v_{f,\|}$ determines the Doppler shift of the photon (Fig. 2.1(a)). The energy dependence of the charge-exchange cross section can distort the spectrum strongly, particularly if the sightline views parallel or antiparallel to the injected beam. Figure 2.5(b) compares the actual spectrum with the spectrum that would be produced if the neutralization rate was independent of energy. Fast ions traveling along the beam are selected preferentially while fast ions traveling against the beam hardly appear in the spectrum because their relative energy is too high. In contrast, this effect has little impact on a vertical view (Fig. 2.5(c)). In this case, the perpendicular component of the motion that determines the Doppler shift is generally perpendicular to the velocity vector of the injected neutrals, so little distortion of the spectrum occurs.

The spectral shape is distorted from fast-ion velocity distribution function because of the energy dependence of the cross sections. For a specific wavelength in the spectrum, the signal is from a collection of fast ions in velocity space. Figure 2.6 illustrates the relationship between the observed Doppler shift and the fast-ion

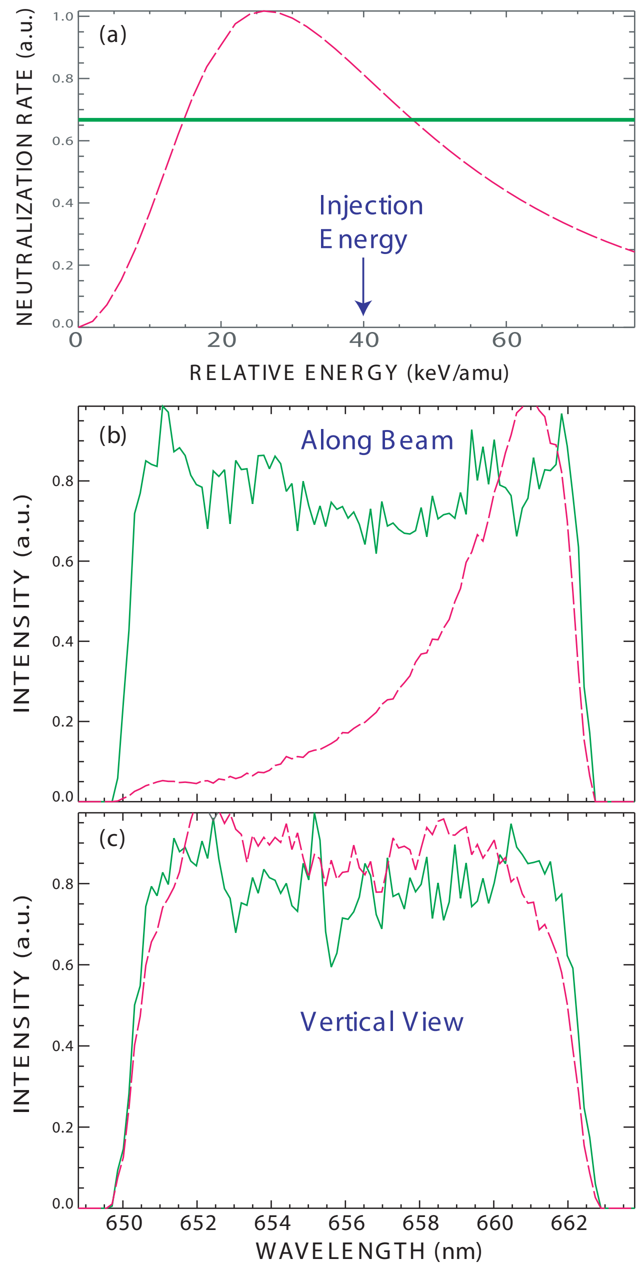

Figure 2.5: (a) Charge exchange reactivity versus relative energy (dashed line) and the constant reactivity used in the artificial simulation (solid line). (b) D_α spectrum from monoenergetic fast ions with a uniform distribution of pitch for a sightline that views antiparallel to the injected beam for the artificial (solid) and true (dashed) reactivity. (c) D_α spectrum from monoenergetic fast ions with a uniform distribution of pitch for a sightline that views the injected beam vertically from above.

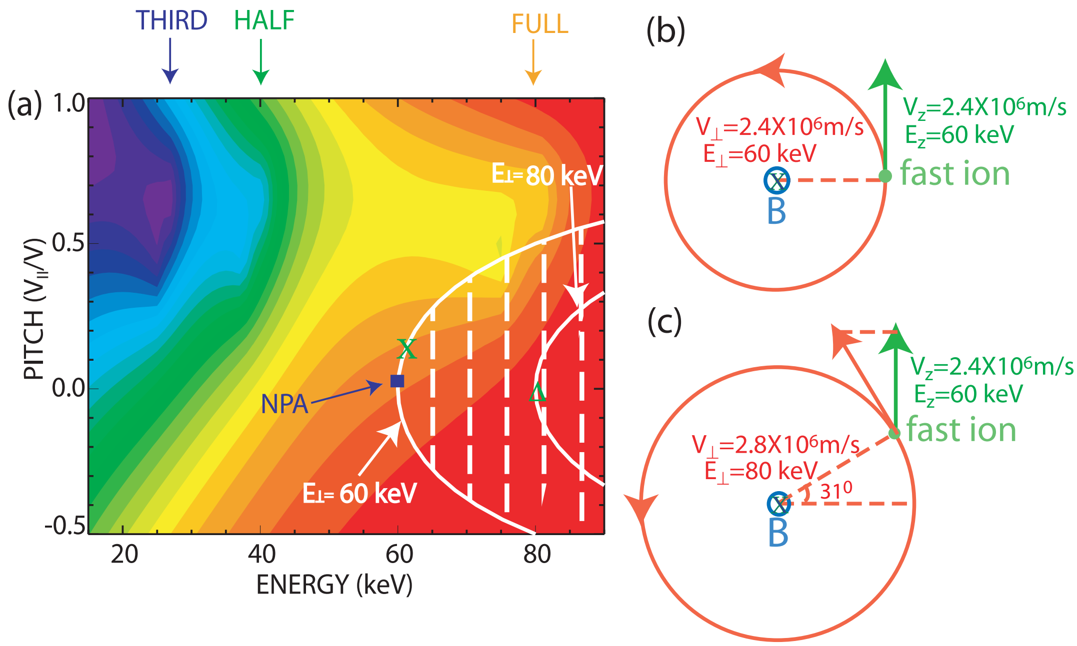

Figure 2.6: (a) Contour plot of the fast-ion distribution function from a local Fokker-Planck calculation. The two parabola like curves represent fast ions with 60 and 80 keV perpendicular energies, respectively. The green $\times(\triangle)$ indicates velocity coordinates that produce the gyro-orbit shown in panel (b) and (c). Fast ions in the white hatched region may have a vertical velocity of 2.4×10^6 m/s. The blue rectangle shows the velocity space of fast ions detected by a vertical NPA channel at 60 keV. (b) The gyro-orbit of any fast ion on the 60 keV perpendicular energy curve. The vertical energy (E_z)is labeled for a specific gyroangle. (c) The gyro-orbit of any fast ion on the 80 keV perpendicular energy curve. The vertical energy is labeled for a specific gyroangle.

distribution function. Because of the rapid gyromotion, in a strongly magnetized plasma, the fast-ion distribution function only depends upon two velocity coordinates. (The phase of the gyroangle is an ignorable coordinate.) A common choice of velocity coordinates is energy and the pitch of the velocity vector relative to the magnetic field. Figure 2.6(a) illustrates a typical fast-ion distribution in a beam-heated DIII-D discharge as a function of energy and pitch. Neutral beams inject deuterons with a particular angle with respect to the magnetic field at three distinct energies. Coulomb scattering decelerates the injected fast ions and scatters them in pitch, filling in the distribution. The Doppler shift of a FIDA proton provides information on one component of the fast-ion velocity vector. A reasonably straightforward interpretation of the signal is available for a vertical view. The measured velocity component is approximately perpendicular to both the injected beam and the magnetic field. Consider the Doppler shift that corresponds to a vertical velocity of 2.4×10^6 m/s in the direction of the detector. Figure 2.6(b) and 2.6(c) illustrate the gyromotion of two ions that could produce this Doppler shift. The minimum perpendicular energy that could produce this Doppler shift is 60 keV [Fig. 2.6(b)]; in this case, the ion produces the desired Doppler shift if it neutralizes just as it is travelling toward the detector (at the $0°$ gyroangle). The Doppler shift can also be produced by a higher energy ion; Figure 2.6(c) shows the gyrophase of an ion with a perpendicular energy of 80 keV that has the correct vertical velocity component if it neutralizes at a gyroangle of $31°$. In addition to the velocity components illustrated in Figs. 2.6(b) and 2.6(c), there is a third velocity component: the component parallel to the magnetic field. This component does not affect the perpendicular gyromotion, so as long as they have the correct perpendicular energy, particles with any value of parallel energy can also contribute light at the selected Doppler shift (as seen by the detector). In terms of energy E and pitch p, any ion that satisfies the equation

$$E = E_{\perp}/(1 - p^2) \tag{2.2}$$

can also contribute light at the selected Doppler shift. (Here $E_{\perp}$ is the perpendicular energy that corresponds to 60 keV in this example.) As illustrated in Fig. 2.6(a), any ions on the 60 keV perpendicular energy curve and in the enclosed hatched region can contribute to the selected wavelength as long as the charge exchange event happens at the proper gyroangle. Thus, for vertical views, the FIDA signal at a particular wavelength originates from an effective average over perpendicular energy.

2.2 Comparison of fast-ion diagnostics with repect to their resolution in velocity space

The different fast-ion diagnostics weight the fast-ion distribution function differently in velocity space (Fig. 2.7). Figure 2.7(a) shows the fast-ion distribution function calculated by TRANSP, $F(E,p)$, at the location of the $R = 180$ cm FIDA channel for a typical discharge in this thesis. [The definition of F employed by TRANSP includes the Jacobian so that $\int\int F(E,p)\,dE\,dp$ yields the fast-ion density.] For injection by the more-tangential Left beams, the distribution peaks near $p \simeq 0.6$ in

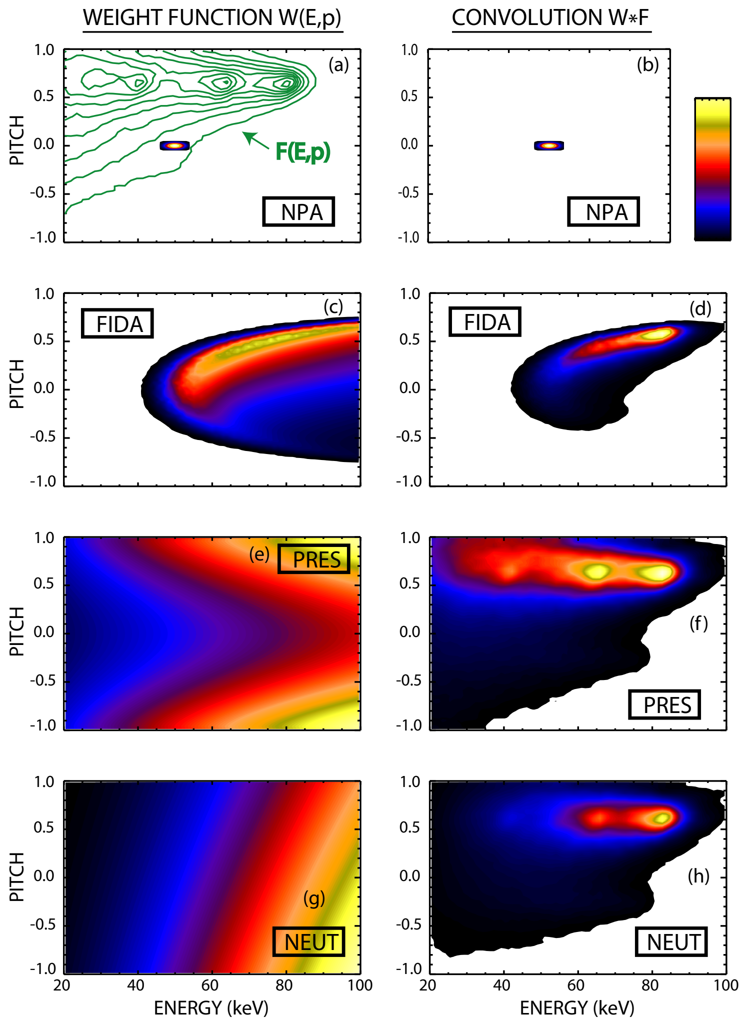

Figure 2.7: Contour plots of the velocity-space weight functions (left column) for the NPA, FIDA, p_f, and neutron diagnostics for discharge #122060 before the ICH. The bar graph in the upper right figure shows the linear color scale in normalized units. The upper left graph also shows the fast-ion distribution function $F(E, p)$ calculated by TRANSP at the location of the 180 cm FIDA channel. The right column shows contour plots of the product of the weight function with the TRANSP distribution function for the four fast-ion diagnostics. The FIDA graphs use the calculated injected neutral densities at 180 cm (full:half:third of 57%:26%:17%), include an approximate treatment of the instrumental resolution (Gaussian spread with $\sigma = 0.21$ nm), and assume $E_\lambda = 50$ keV. The neutron weight function is for beam-plasma reactions only and employs the measured ion temperature (5.0 keV) and toroidal rotation (2.1×10^7 cm/s). The weight function is negligible in the white regions.

the plasma center. It is convenient to describe the velocity-space weighting of the various diagnostics by a weight function, $W(E, p)$. The signal from the diagnostic is then $S = \int \int W(E, p) F(E, p)\, dE\, dp$.

The velocity-space weight function $W(E, p)$ for the FIDA diagnostic (Fig. 2.7(c)) depends on three factors: the minimum energy, the gyroangle weighting, and the probability of a charge-exchange reaction. Through the photon Doppler shift, a particular wavelength corresponds to a vertical energy E_λ. Once a value of E_λ is specified, the minimum energy that can contribute this vertical energy consists of a curve in velocity space [25]. For simplicity, we first consider a vertical view. This curve is $E = E_\lambda/(1 - p^2)$; this accounts for the approximately parabolic shape of the $W \neq 0$ region in Fig. 2.7(c). Within this region, the probability of emitting a photon with the specified wavelength is largest for ions near the minimum-energy boundary (because they spend a greater fraction of their gyromotion heading in the desired direction). This effect is symmetric in pitch and explains why the weight function peaks at the minimum-energy curve. The final effect is associated with the probability of a charge-exchange reaction. Reactions are more probable for fast ions that have a component of velocity in the direction of the injected neutral beam; the weight function is skewed toward positive values of pitch by this effect. Weight functions for other values of E_λ are qualitatively similar (not shown). As Fig. 2.7(d) shows, for a typical distribution function, the FIDA signal for $E_\lambda = 50$ keV is actually dominated by ions born near the injection energy and angle ($E \simeq 80$ keV; $p \simeq 0.6$).

Now, we generalize the expression to arbitrary viewing geometry. The unit vector from the measurement volume to the collection lens is $\hat{\lambda}$. Decompose this unit vector into components parallel and perpendicular to the magnetic field, $\hat{\lambda} = \lambda_{\|}\hat{b}_{\|} + \lambda_{\perp}\hat{b}_{\perp 1}$, where $\hat{b}_{\|}$ is a unit vector parallel to $\vec{B}$ and $\hat{b}_{\perp 1}$ is the unit vector perpendicular to $\vec{B}$ that is in the same plane as the sightline and $\hat{b}_{\|}$. (The third unit vector, $\hat{b}_{\perp 2}$ is perpendicular to this plane.) The fast ion has a velocity $\vec{v}$. Its velocity component along $\hat{\lambda}$ determines the Doppler shift $\Delta\lambda$, $(\hat{\lambda} \cdot \vec{v})/c = \Delta\lambda/\lambda_0$. ($\lambda_0$ is the unshifted wavelength and c is the speed of light.) The Doppler-shift velocity component is $\hat{\lambda} \cdot \vec{v} = \lambda_{\|}v_{\|} + \lambda_{\perp}v_{\perp 1}$. Here, $v_{\perp 1}$ is the component of the perpendicular velocity $\vec{v}_{\perp}$ that is along $\hat{b}_{\perp 1}$; this component rapidly changes because of the particle gyromotion. Straightforward algebra yields the minimum energy E of a fast ion that can produce a Doppler shift that corresponds to an energy E_{λ},

$$E = \frac{E_{\lambda}}{(\lambda_{\|}p + \lambda_{\perp}\sqrt{1-p^2})^2}, \tag{2.3}$$

where p is the fast-ion pitch $v_{\|}/v$. Note that for $\lambda_{\|} = 0, \lambda_{\perp} = 1$, this reduces to Eq. (2) of Ref. [25]. In (E, p) space, all particles to the left of the curve described by Eq. 2.3 have $W = 0$.

The minimum energy that can produce a given Doppler shift (Eq. 2.3) occurs when the perpendicular component of the fast-ion velocity is either parallel or anti-parallel to $\hat{b}_{\perp 1}$. For other values of the gyroangle φ, higher energy is needed to produce the observed Doppler shift. In terms of gyroangle, the fast-ion velocity component along $\hat{b}_{\perp 1}$ is $v_{\perp}\cos\varphi$. In the region of velocity space with sufficient energy to contribute to E_{λ}, the gyroangle of the fast ions that contribute is

$$\varphi = \cos^{-1}\{\frac{\pm\sqrt{E_{\lambda}/E} - \lambda_{\|}p}{\lambda_{\perp}\sqrt{1-p^2}}\}, \tag{2.4}$$

where the $+(-)$ sign is for a blue(red)-shifted photon. Since the gyromotion is uniform, all values of gyroangle are equally likely. However, since the velocity component along $\hat{b}_{\perp 1}$ is proportional to $\cos\varphi$, the relative contribution to the spectrum is greatest for ions with φ near zero or π, where the velocity component changes slowly. ("Wings" at maximal Doppler shifts is a familiar spectral feature produced by gyrating, monoenergetic particles; see, e.g., Ref. [50].) To derive the weight function associated with gyromotion, note that

$$\int_{\lambda_{min}}^{\lambda} W_{\varphi}(\lambda)\, d\lambda \propto \int_{0}^{\varphi} g(\varphi)\, d\varphi. \tag{2.5}$$

Here $g(\varphi)$ is the probability of finding the fast ion at a particular gyroangle, which is $g(\varphi) = 1/(2\pi)$ for uniform gyromotion. Differentiate Eq. 2.5 and use Eq. 2.4 to obtain the gyroangle weight function,

$$W_{\varphi} \propto (\sqrt{E}\sqrt{1-p^2}\sin\varphi)^{-1}. \tag{2.6}$$

Although Eq. 2.6 is a useful analytical description of W_{φ}, it is inconvenient for numerical work because it is singular at $\varphi = 0$. For numerical work, it is more convenient to calculate the fraction of particles that contribute to a particular energy bin of width δE_{λ}. The weight function W_{φ} is proportional to the range of gyroangles that can contribute to this energy bin, $W_{\varphi} \propto |\varphi_{max} - \varphi_{min}|$. The range of gyroangles is readily calculated using Eq. 2.4.

The final factor that contributes to the FIDA weight function is the probability of a charge-exchange reaction that converts a fast ion into a neutral in the $n = 3$ energy level, W_{cx}. This factor depends upon the relative velocity between the particular fast ion under consideration and all of the neutral populations associated with the diagnostic beam (full, half, and third energy components and the halo-neutral population). In addition, a full treatment must consider the energy-occupation levels of the various neutral populations and the cross section from each energy level to the $n = 3$ level. For a given point in (E, p) space, the gyroangles that can contribute to a specified E_λ are given by Eq. 2.4, so the relative velocity is readily determined for use in evaluation of the reactivities σv. For simplicity, halo neutrals and reactions from excited energy levels are neglected in the calculation of W_{cx} shown in Fig. 2.7. The total FIDA weight function is the product of W_φ and W_{cx}.

Figure 2.7 also shows the weight functions for the other diagnostics employed in this thesis. The neutral-particle analyzer has excellent energy resolution ($\sim 3\%$) and is narrowly collimated ($\sim 1°$), so the NPA essentially measures a point in velocity space (Fig. 2.7(a)). For the NPA, W is nearly a delta function at $E = 50$ keV and $p = 0$. As a result, the signal (Fig. 2.7(b)) comes from the same portion of velocity space as the peak in the weight function.

The weight function for the fast-ion pressure measurement is

$$W_{pres} \propto E(p^2 + \sqrt{1 - p^2}/2). \tag{2.7}$$

The weight function W extends throughout velocity space (Fig. 2.7(e)). Each ion contributes $E_\parallel + \frac{1}{2}E_\perp$ to the MHD pressure, so the weight function is larger for large $|p|$ than for small $|p|$. Convolution with a typical distribution function shows that the pressure measurement samples much of the distribution function, with the greatest contribution from full-energy beam ions (Fig. 2.7(f)).

In most of the plasmas in this thesis, the neutron rate is dominated by beam-plasma reactions. (For example, for the ICH-heated discharges in Chapter 6, TRANSP computes that $\sim 80\%$ of the reactions are from beam-plasma, while most of the remainder are from beam-beam reactions.) The weight function for beam-plasma neutron measurements depends on the relative velocity of the fast ions with the thermal deuterons. We assume that the distribution for the thermal deuterium is described by a drifting Maxwellian with temperature T_i and drift velocity v_{rot} in the $\hat{b}_{||}$ direction. $W_{neutron}$ is found by integrating the d-d reactivity σv over the thermal distribution function with (E, p) specified. Figure 2.7(g) shows the weight function for beam-plasma reactions. The weight increases rapidly with energy because the d-d fusion cross section increases rapidly with energy. The asymmetry in pitch is associated with plasma rotation: for a given fast-ion energy, the reaction probability is higher for a counter-going ion because the relative velocity between the fast ion and the thermal ions is larger. Because of the strong energy weighting, the neutron signal arises primarily from fast ions near the injection energy (Fig. 2.7(h)).

Comparison of the figures (right-hand column in Fig. 2.7) shows that, despite the substantial differences between the FIDA, pressure, and neutron measurements, the signals actually arise from the same region in velocity space. The NPA diagnostic is unique in sampling a region of the distribution far from the bulk. Of course, there is also an important distinction between diagnostics in configuration space: the NPA, FIDA, and pressure diagnostics are local measurements, while the neutron diagnostic is volume-averaged.

2.3 Hardware description

Figure 2.8 shows a schematic view of the FIDA system. The D_α light of reneutrals is emitted from the region of plasma traversed by the neutral beam. A lens (f/4.4) located at a port under the midplane collects and focuses light onto several optical fibers with a 1500 μm core diameter, each of which defines a viewing chord through the plasma. The observation volume of each chord can be approximated by a cylinder across the beam. The light travels along the optical fibers to a Czerny-Turner spectrometer (f/4, 1800 grooves/mm grating, and 300 mm focal length) with a fiber holder mounted around the entrance slit. The FIDA diagnostic is designed to accomodate two channels simultaneously with the ability to switch fibers between discharges. Fibers can be switched quickly at the fiber holder if necessary. At the exit plane of the spectrometer, the light is dispersed into a two dimensional pattern: vertically, the light is separated into two chords; horizontally, the light from each fiber is dispersed in wavelength (as indicated by the shading in the focal plane shown in Fig. 2.8). A vertical bar sitting on two horizontal translation stages on the exit focal plane blocks the portion of the spectrum with bright interfering signals that would otherwise saturate the detector. The blocking bar has a rectangular cross section 1 mm wide and 2 mm long. The bottom of the bar is threaded so that the bar can be rotated and has an adjustable blocking range between 1 and $\sqrt{5}$ mm. We typically block a 2 nm portion of the D_α range. Note that light diffraction by the blocking bar is negligible and even if it was substantial, it would not degrade the spectral resolution since the bar sits in the focal plane. The image on the exit focal plane is reduced by two camera lenses (85 and 50 mm focal lengths) coupled together by a macrocoupler and a step ring. A charge-coupled

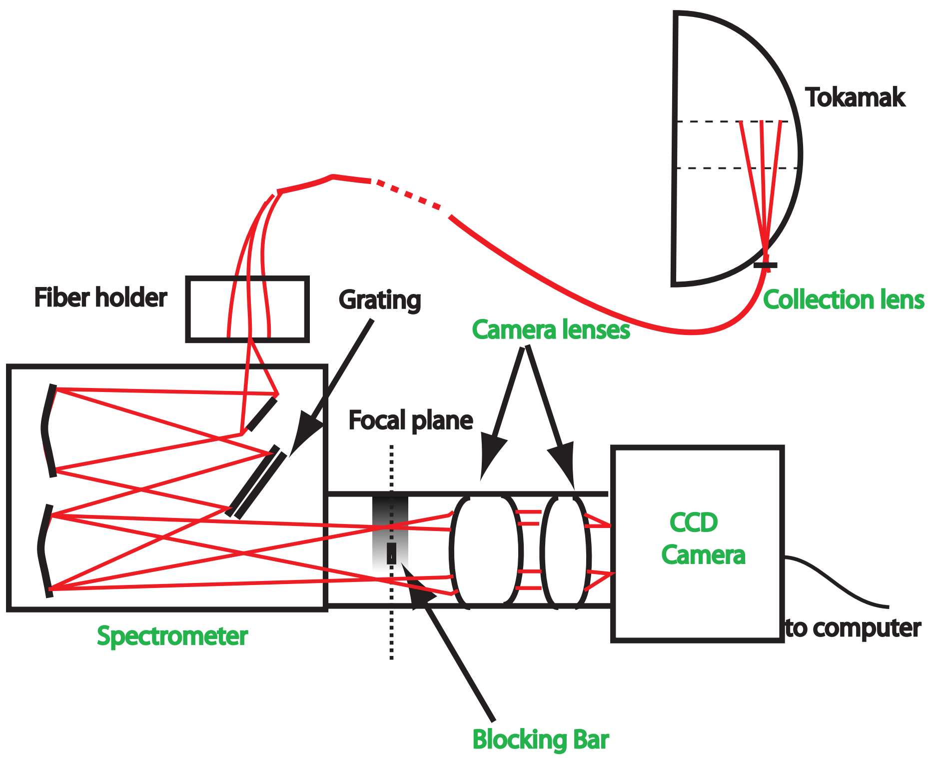

Figure 2.8: FIDA system schematic as viewed from above. The shaded rectangle represents the dispersion of wavelength.

device (CCD) camera (2.2 MHz, 14 bits) with its CCD chip ($8 \times 6\ mm^2$) on the focal plane of the second lens detects the light with 1 ms integration time. The CCD camera is surrounded by a radiation shielding box (discussed later). Electrical signals from the CCD chip are amplified, digitized, and transfered to a dedicated Windows personal computer (PC). The data are then transfered to a master Linux PC through Ethernet cable. Finally, they are archived to the DIII-D data server.

The FIDA diagnostic is designed with maxium light gathering power at the D_α wavelength, subject to the constraint of matching the optics on the tokamak. With an f/4.4 collection lens, fixed CCD chip width, and constant spectral resolution, the detected signal is independent of the f/number of the spectrometer if light loss from lens surfaces is ignored. However, if the f/number of the spectrometer does not match the f/number of the collection lens, two lenses are needed in front of the entrance slit to convert the f/number, which increases the complexity of the system and leads to loss of some portion of light. Thus a spectrometer of f/4 is optimal for the FIDA diagnostic. Another important specification of the spectrometer is the groove density of the grating in the spectrometer. Assuming constant spectral resolution, the higher the groove density, the wider the entrance slit can be, which translates into more signal detected. The groove density is subject to two constraints. The first one is dispersion. If dispersion is too high, we have trouble demagnifying the image to fit onto the CCD chip. Since the lowest f/number of readily available commercial lenses is f/1, the largest demagnification ratio we could achieve is 1/4 with f/4 and f/1 lenses. The second constraint is the optimum range of operation for the grating. Generally high groove density gratings are optimized fro short wavelength. Based on the above considerations, SpectraPro 300i from the

Acton Research Corporation (f/4, 1800 grooves/mm grating, and 300 mm focal length) was chosen.

The bright interfering signals around the rest D_α wavelength require an extremely high dynamic range for the detector, which usually comes at a very high cost. There are three possible solutions. A notch filter would be ideal and easy to integrate into the system (it could be put between the two camera lenses). The problem with this solution is that the width of the required filter is too narrow (2 nm). Such notch filters are not commercially available yet. Oversampling very rapidly could be a solution, but it would require unrealistic CCD speed. Moreover the camera readout noise would be huge if the camera ran so fast. A practical expedient is to use a blocking bar on the exit focal plane of the spectrometer. The bar is positioned to block the interfering light.

The image on the exit focal plane of the spectrometer is about 11 mm wide, which exceeds the width of the CCD chip (8 mm). Therefore an image reducer with a demagnification ratio of 8/11 or smaller is required between the spectrometer and the CCD camera. Although simple lenses do not have a flat focal plane, camera lenses are compound, multi-element lenses specifically designed to create a flat image on a piece of film or a flat CCD chip. Another advantage of camera lenses is that they are relatively inexpensive because of the mass consumer market. Theoretically either one single lens or a pair of lenses can serve as an image reducer, however two coupled lenses can substantially improve the quality of image. The two camera lenses are subject to three constraints. First, the ratio of the focal lengths of the lenses should be 8/11 or a little less to ensure that the fullD_α spectrum can be detected by the camera. Second, the first lens should be capable of collecting all the

D_α light coming out of the spectrometer. This means the lens should have an f/number equal to or lower than the f/number of the spectrometer (f/4). Third, the aperture of the second lens should be large enough to collect all of the light that comes out of the first lens. Nikkor 85 mm f/1.8 AF and Nikkor 50 mm f/1.4 AF meet the above requirements and are chosen for the image reducer.

The fast ion profile can change on ~ 1 ms timescale. Consequently the FIDA diagnostic is designed to have a minimum integration time of 1 ms. Another benefit of such a high temporal resolution is that data contaminated by ELMs (edge localized modes) can be identified and removed (as is discussed in § 3.1). Unfortunately it is hard to find a shutter capable of operating this fast. In order to take multiple spectra on a single CCD camera without a shutter, there have to be multiple readout nodes to read out the spectra separately to avoid cross talk. The CCD camera chosen is the $VelociCam^{TM}$ VC105A from $PixelVision^{TM}$ which has four readout nodes. It can take two spectra with one on the upper half of the CCD chip and one on the lower half of the CCD chip. If each spectrum can be reduced to half of the CCD width, the camera can take four spectra simultaneously. The FIDA diagnostic is designed to take two spectra to get more signal and facilitate the design of the blocking component. Since the vertical direction of each spectrum on the CCD chip contains no useful information, pixels on the vertical direction are binned together to improve the readout speed. In addition, since only a coarse spectral resolution is necessary, the serial direction bins by two. When operating under the above binning, a minimum integration of 0.33 ms is achieved, which exceeds the 1 ms requirement.

The CCD camera is very sensitive to neutron/γ radiation, especially γ rays.

Neutrons are produced by fusion reactions in the DIII-D plasma and the subsequent production of γ rays occurs by neutron capture in the surrounding structure. The FIDA camera is located outside the DIII-D neutron shield wall. To introduce further neutron/γ shielding, a shielding box [51] is put around the CCD camera. The shield has shielding material on five sides, with the spectrometer being on the sixth, open side which faces away from the tokamak. For each side, 15 cm of borated polyethylene and 5 cm of lead are used to absorb neutrons and g rays respectively. This provides about a factor of 40 reduction in the n/γ hits on the detector.

Three timing triggers are required for the FIDA diagnostic. The CCD camera trigger commands the camera to read out data. The camera is triggered every 1 ms during each shot to have a 1 ms integration time and every 10 ms between shots to keep the temperature of the camera stable. The camera is connected to the slave Windows PC. The slave PC is triggered a short time before each shot to start transferring data from the camera to the PC. The master Linux PC which remotely controls the camera also needs a trigger before each shot to get ready for transferring data from the slave PC to the master PC. The PCI-6601 timing card from National Instruments is inserted into the slave PC and configured to generate various trigger pulses. The PCI-6601 timer/counter has four counters. A timing pulse from the timing receiver, synchronized with DIII-D operations, provides input to the counters. The first counter is configured to generate retriggerable single pulses, which are input for the second counter. The second counter, which performs frequency shift keying, produces pulses every 1 ms during a shot and every 10 ms between shots. The output of the second counter serves as the camera trigger. The third counter, which is configured to generate retriggerable single pulses, provides the timing trigger for the slave PC. The timing trigger for the master PC can be generated similarly by the fourth counter. In reality, a timing pulse from the timing receiver is used to trigger the master PC directly.

The PCI timing card has significant advantages over CAMAC systems. The cost is greatly reduced and it requires little space. However, it introduces a timing jitter to the system as shown in Fig. 2.9(a) and (b). The signal in Fig. 2.9(a) indicates the status of operation with 1 being during a discharge and 0 being between discharges. Figure 2.9(b) shows the camera triggering signal, which is supposed to be every 10 ms between discharges and every 1 ms during a discharge. However, in reality, at the onset of transition of frequency, the counter does not start the 1 ms pulses immediately, instead, it finishes the current 10 ms pulse first. As a result, there is a timing jitter between -10 ms and 0 ms, which is unacceptable for the FIDA diagnostic. A smart way to decrease the timing jitter without replacing the timing system is to make the onset of transition of frequency earlier, for instance, at -70 ms, assuming beam is on at 0 ms. At -60 ms and beyond, the pulses are certain to be every 1 ms. Now a timing signal at a time, for example, -50.5 ms is sent to the slave PC to start transfering data from the camera to the PC. The first 50 time slices are discarded and the 51st time slice is considered to be at 0 ms in diagnostic time. In tokamak time, it can be anywhere between -0.5 ms and 0.5 ms. In another words, the timing jitter is between -0.5 ms and 0.5 ms, a great improvement over the -10 ms to 0 ms. Figure 2.9(c) and (d) illustrate two extreme cases with a timing jitter of -0.5 ms and 0.5 ms respectively.

In addition to the dedicated FIDA diagnostic discribed above, the CER Reticon system is sometimes shifted from its usual wavelength to the D_α transition to

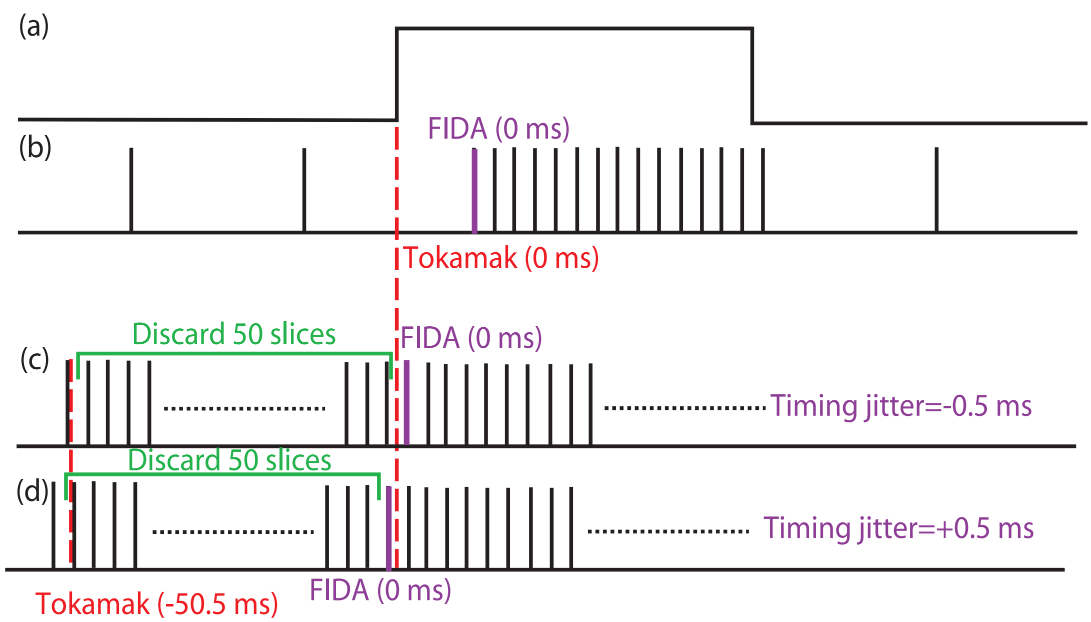

Figure 2.9: (a) the gate signal for generating pulses with different frequencies. High generates a pulse every 1 ms and low generates a pulse every 10 ms. (b) the pulses generated by the counter in reality. (c)an extreme case with a timing jitter of -0.5 ms. (d)the other extreme case with a timing jitter of 0.5 ms.

measure the FIDA signal. The Reticon system has two disadvantages: it measures only one third of the entire FIDA spectrum, usually the blue side which has fewer impurity contamimants (§3.1) and the quantum efficiency of the detector is merely $\sim 15\%$, in another words, the signal to noise ratio (SNR) is fairly poor. A common technique to improve the SNR of the Reticon measurements is to average over a large time window during steady plasma conditions. Despite the disadvantages, the Reticon system which consists of dozens of chords is very valuable for measuring the FIDA spatial profile. Figure 2.10 shows the fiber views for the data presented in this thesis. For all of the vertical views, the collection lens is located at a port under the midplane. Although the chords are designed to view the left beam, some of them do see a small portion of the right beam, especially the outer chords.

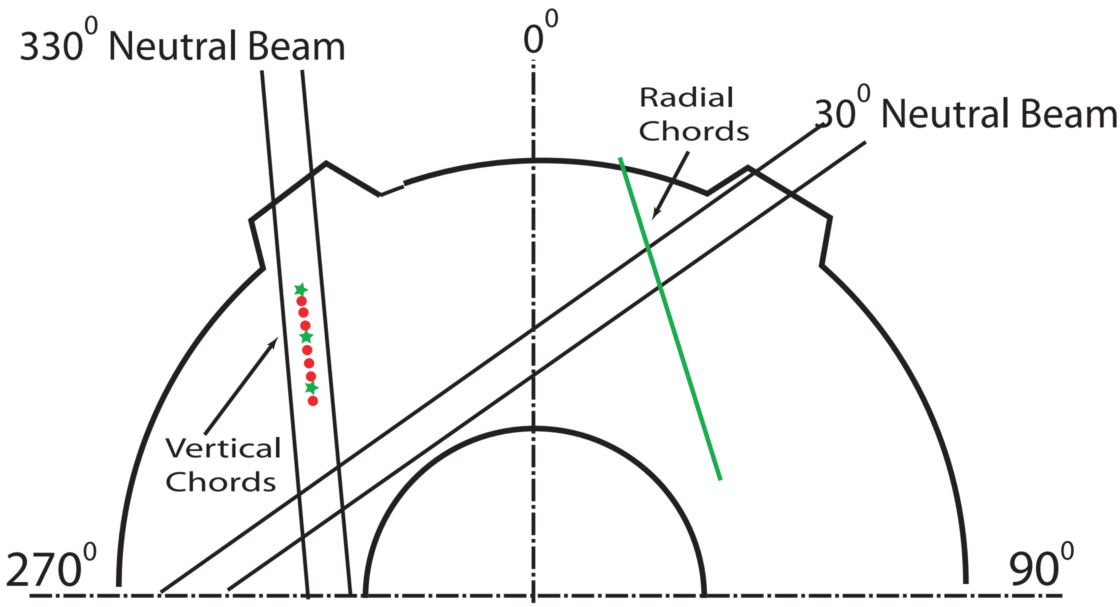

Figure 2.10: FIDA fiber views shown on the midplane. The fiber views for the dedicated system are shown in green, and those for the Reticon system in red. The beams in the figure are left beams.

Chapter 3

Data analysis

3.1 Extraction of the fast-ion signal from the raw spectrum

Figure 3.1(a) shows typical raw data. There are various contaminants in the spectrum. Impurity lines appear as bumps in the spectrum. Halo emission extends beyond the blocked wavelengths on both sides. Visible bremsstrahlung and scattered light are distributed over the entire spectrum and are most evident beyond the injection energy, where no fast-ion signal is expected in the absence of ion cyclotron heating. Finally, for some time slices, there are huge spikes caused by neutron or γ hits.

Although the CCD camera is placed inside the shielding box, neutrons and γ rays can penetrate to the CCD chip occasionally, especially when the discharge has a neutron rate in excess of 10^{15} n/s. Neutron/γ hits affect one pixel (or two pixels when the hit occurs on the boundary of pixels). They usually appear as huge spikes (at least hundreds of counts) that are readily identified and replaced by the average of the adjoining pixels. Small spikes caused by neutron/γ hits on the sharply rising or falling slope of halo emission are more challenging to detect; a special conditional statement in the analysis code identifies these hits.

As discussed in §2.3, a timing jitter exists for the FIDA diagnostic. Because we routinely perform beam-on and beam-off background subtraction, those time slices

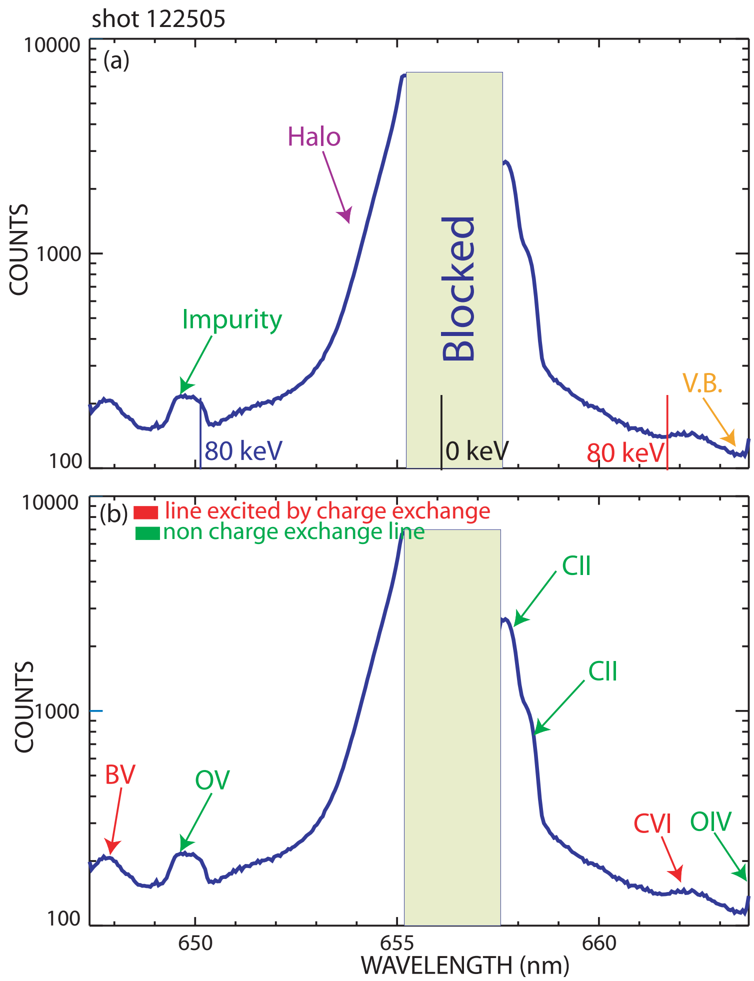

Figure 3.1: (a) Contaminants in the spectrum. A log plot is shown in order to make impurity lines, visible bremstrahlung and scattered light clearer. The central part of the spectrum is blocked by the blocking bar to avoid saturation. (b) Impurity lines in the spectrum.

with partial beam-on and beam-off periods (timing jitter contaminated time slices) must be removed first. For each beam-on or beam-off period, there is exactly one timing jitter contaminated time slice. If the timing jitter is negative, in other words, the diagnostic time is behind the tokamak time, each last beam-off time slice and each last beam-on time slice are removed. If the timing jitter is positive, each first beam-off time slice and each first beam-on time slice are removed. To quantitatively calculate the timing jitter, four time slices around the onset of the beam (two before and two after) are chosen. Because beam-on signals usually elevates considerably over beam-off signals. The signal increasing pattern and degree can reasonably estimate the timing jitter.

Figure 3.1(b) shows a detailed look at the impurity lines. There are six main impurity lines in the spectrum. The BV and CVI line are lines excited by charge exchange; they appear only when the FIDA beam is on. The OV line, the two CII lines and the OIV line are non charge exchange lines. They appear whether the beam is on or not, and therefore, they can be removed by beam modulation and timeslice subtraction.

Impurity lines are removed by fitting a theoretical response function to the data using the method of nonlinear least squares. Assuming a Maxwellian distribution function of the impurity, the impurity line is a Gaussian due to Doppler broadening (Both the Stark effect and the Zeeman effect are neglibible for the impurities). The theoretical response function is the convolution of the Gaussian line shape radiated by the impurity with the instrumental response. In general, convolution needs to be done numerically, however the convolution of two Gaussians is another Gaussian. This is the motivation for us to represent the instrumental response by the sum of a few Gaussians. The instrumental response data are taken by illuminating the fibers with a neon lamp. Because the neon is cold, Doppler broadening of such lines is negligible, thus the broadening observed in such a measurement is only due to instrumental effects. The asymmetry of the instrumental broadening (Fig. 3.2) is because of the nonideal instrument. We have determined empirically that the instrumental response function can be adequately represented by the sum of three Gaussians (Fig. 3.2),

$$I_i = \sum_{j=1}^{3} \frac{a_j}{\sigma_j \sqrt{2\pi}} e^{-\frac{(i-\mu_j)^2}{2\sigma_j^2}}. \tag{3.1}$$

Here, i denotes the pixel number, j denotes different Gaussians, a_j is the amplitude, σ_j is the standard deviation, and μ_j is the center location. Assuming the Gaussian line radiated by the impurity due to Doppler broadening is

$$I_i = \frac{a}{\sigma\sqrt{2\pi}} e^{-\frac{(i-\mu)^2}{2\sigma^2}}, \tag{3.2}$$

the theoretical response function for the impurity line is

$$I_i(a,\sigma,\mu) = \sum_{j=1}^{3} \frac{a_j a}{\sqrt{\sigma_j^2+\sigma^2}\sqrt{2\pi}} e^{-\frac{(i-\mu_j-\mu)^2}{2(\sigma_j^2+\sigma^2)}}. \tag{3.3}$$

The empirical approximation of a straight line suffices for the fast-ion contribution in the short spectral range that the impurity line spans,

$$I_i = c_1 + c_2 i. \tag{3.4}$$

The complete theoretical response function including impurity contribution and

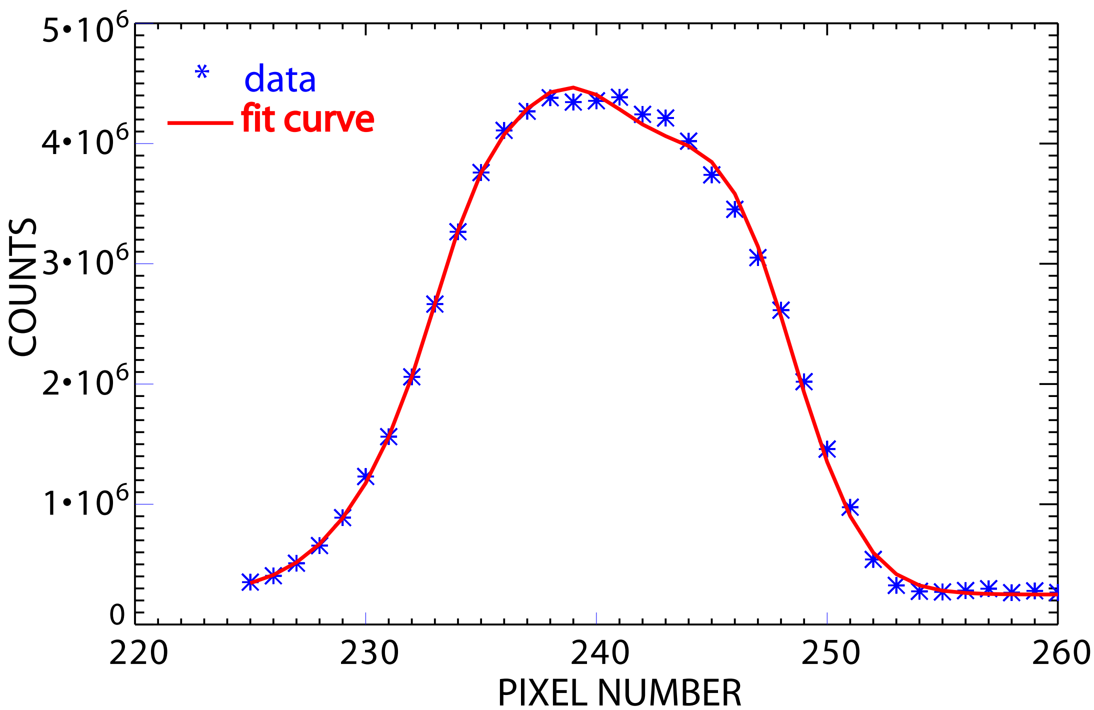

Figure 3.2: Spectrum from a calibration lamp showing the fitting of the instrumental response[Eq. 3.1].

fast-ion contribution is

$$I_i(a, \sigma, \mu, c_1, c_2) = \sum_{j=1}^{3} \frac{a_j a}{\sqrt{\sigma_j^2 + \sigma^2}\sqrt{2\pi}} e^{-\frac{(i-\mu_j-\mu)^2}{2(\sigma_j^2+\sigma^2)}} + c_1 + c_2 i. \tag{3.5}$$

This theoretical function with five free parameters is fitted to the experimental data by MPFIT[52], which uses the Levenberg-Marquardt technique[53, 54] and has the capability of imposing boundary constraints on parameter values. After the fitting is completed, the impurity line contribution [which is the three Gaussians in Eq. 3.5] is subtracted from the raw data (Fig. 3.3).

Theoretically, the halo signal can be removed using the same fitting technique since the halo signal can be modeled the same way as impurity lines; however, it is much harder to fit the halo signal. One difficulty is that the halo signal spans a much broader range than impurity lines and the central part is blocked. Another difficulty is that the fast ion contribution is substantial over the same range. Thus, building an accurate fast ion model is crucial. Unfortunately, no universal fast ion model exists since the line shape depends on plasma conditions. We employ an *ad hoc* three parameter polynomial as the fast ion model and get reasonable fits (Fig. 3.4). An empirical way to check the fitting quality is to compare the derived ion temperature converted from the standard deviation of the halo line with the CER measurement. For the discharge in Fig. 3.4, the derived ion temperature at the chord location is 6 keV, in very rough agreement with the CER measurement of carbon impurities of 4 keV. A rough estimate shows that the halo signal can only reach as far as 20 keV in the spectrum in a plasma with a temperature of 4 keV. This means that the fitting is not even necessary with moderate ion temperature plasmas since the low energy fast ions are not of particular interest. However, in

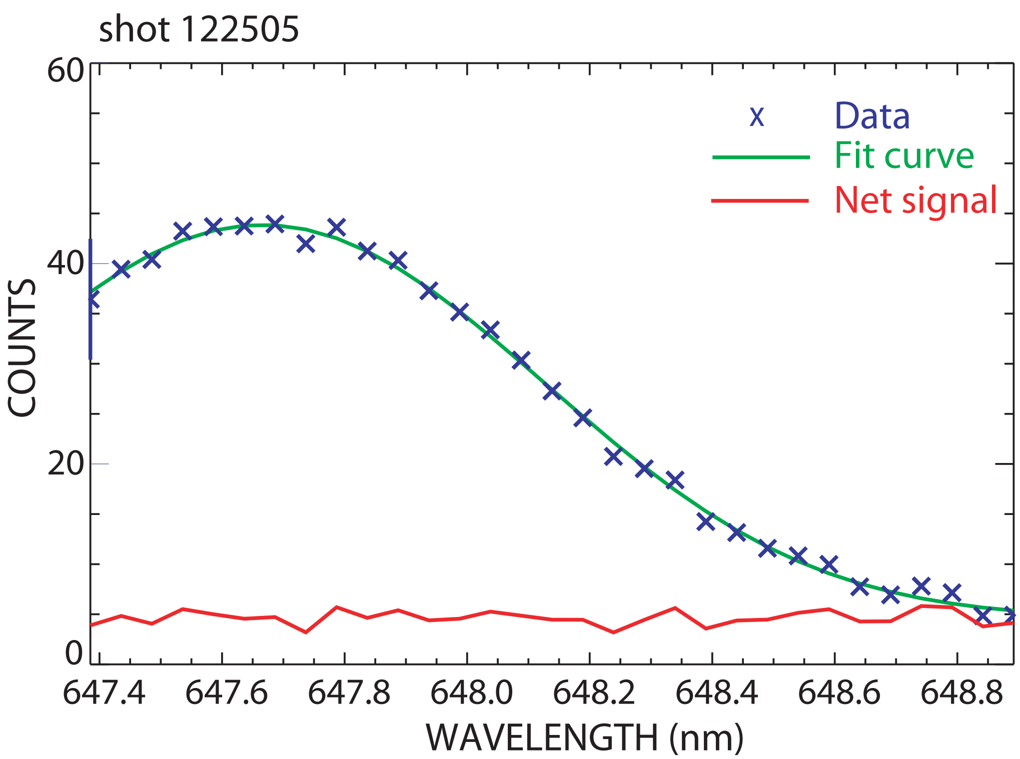

Figure 3.3: Fitting of the BV line. The fast-ion signal is near zero because this impurity line is in the wavelength range which corresponds to energies above the injection energy.

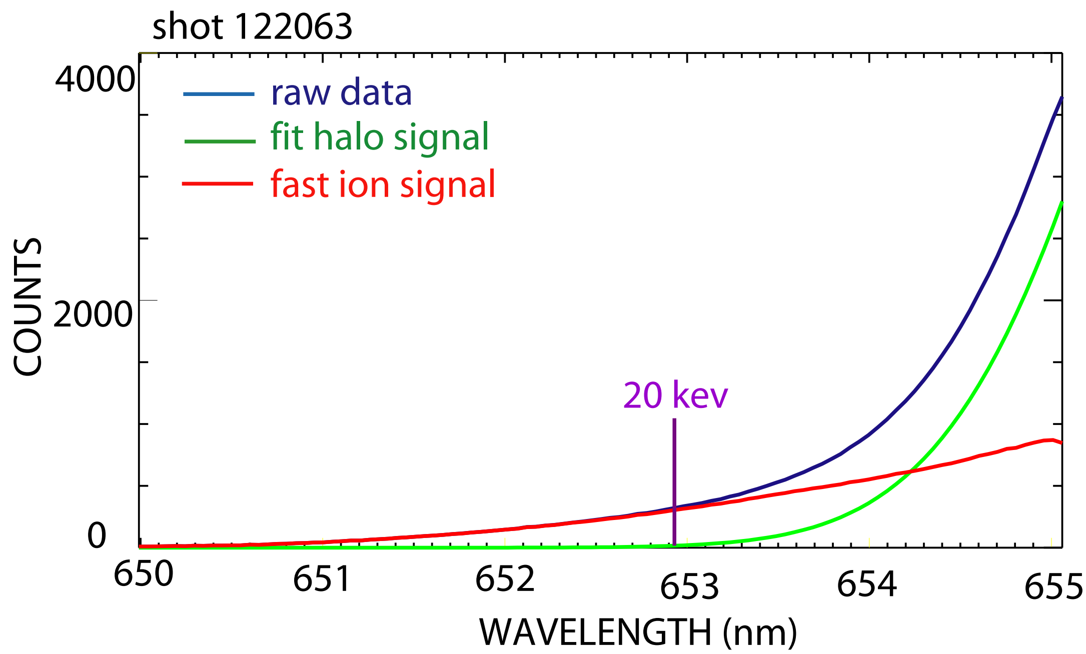

Figure 3.4: Fitting of halo signal. The result is shown as two components (halo contribution and fast-ion contribution). The line shows the wavelength corresponding to 20 keV energy. Beyond this line on the left side are higher energies. Plasma temperature at the chord location for this shot is 4 keV.

extremely high temperature plasmas, the halo signal can contaminate a larger range and halo fitting becomes important. Therefore, finding a good fast ion model would be beneficial.

Beam-on and beam-off subtraction is an important technique to remove contaminants in plasmas that evolve slowly relative to the time between beam pulses. Visible bremsstrahlung, some scattered light, and non charge exchange impurity lines are readily eliminated. As shown in Fig. 3.5, the four non charge exchange impurity lines completely disappear. Visible bremsstrahlung and scattered light are also well subtracted, as can be seen from the wings of the spectrum above the injection energy. This subtraction is usually done over a selected time window. To study fast ions in quiescent plasma, large windows (a few hundred milliseconds) are selected to improve the signal to noise ratio.

Background subtraction by beam modulation works well in many cases but, when there are rapid changes in background, it becomes problematic and special care is required. A common rapid background change for the FIDA diagnostic is caused by ELMs which occur in the high-confinement mode. Since the FIDA sightlines cross the plasma edge, it is not surprising that large ELMs can elevate the FIDA signal significantly through light that scatters off the blocking bar. One ELM can affect up to three time slices depending on the duration of the ELM. As a result, the affected time slices must be eliminated. ELMs are monitored by an independent edge D_α diagnostic at DIII-D . An edge D_α signal is integrated over every 1 ms, which is the FIDA integration time. Because of the timing jitter of the diagnostic, the edge D_α signal should be averaged in the diagnostic time instead of the tokamak time. Empirical absolute and relative thresholds are set to eliminate

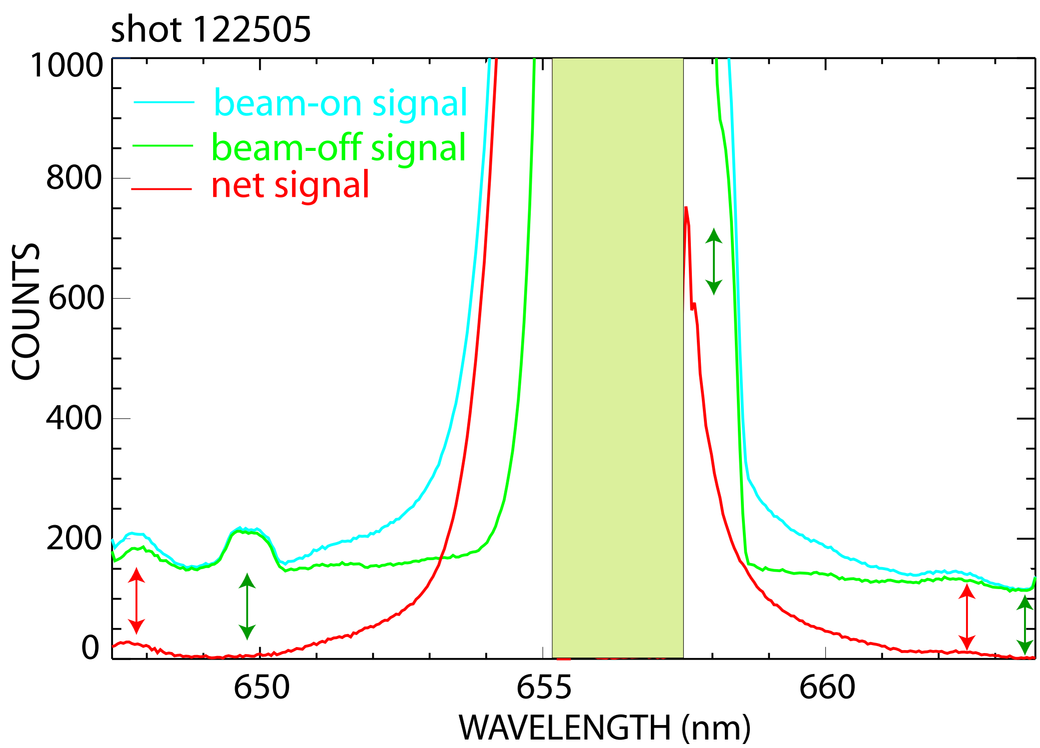

Figure 3.5: Background subtraction by means of beam modulation. The beam is modulated with 10 ms on and 10 ms off. The beam-on and beam-off signals in this figure are averaged over a 300 ms time window.

data contaminated by ELMs. This technique works well in steady-state H-mode plasmas with occasional ELMs.

After the background subtraction, there are two impurity lines remaining (BV and OVI). They are fit and removed from the spectrum, as described above. For plasmas with steady conditions, the combination of beam modulation, fitting of charge-exchange lines, and removal of time slices that are contaminated by occasional bursts of edge D_α light successfully extracts the fast-ion signal from the measured spectra.

On the other hand, the beam modulation technique is inadequate for transient plasmas. An important application of the FIDA diagnostic is to measure the effect of transient instabilities on the fast-ion distribution. These instabilities often expel particles or heat to the plasma edge, causing changes in background that can obscure the fast-ion contribution to the spectrum. Analysis of these plasmas requires removal of backgrounds from individual time slices. The first step of the analysis is to fit and remove the impurity lines, as described above. Next, we assume that visible bremsstrahlung and scattered cold D_α light are the dominant contributions to the remaining background, so

$$B = a_V V + a_D D, \tag{3.6}$$

where B is the background, V is the magnitude of the visible bremsstrahlung, D is the magnitude of the cold D_α light, and a_V and a_D are coefficients that may be functions of wavelength. (Spectra acquired without plasma show that electronic offsets are negligible.) To find a_V and a_D, a large database of background spectra (acquired when the FIDA beam is off) is assembled. Independent measurements of the level of the visible bremsstrahlung V and the cold D_α light D at the times of these spectra are obtained from other DIII-D diagnostics. (Ideally, these quantities would be available along the same sightline as the FIDA chords.) A multiple regression on these background signals yields a_V and a_D for each pixel. The results of this analysis are shown in Fig. 3.6(b). As expected, the fit coefficient a_V of the visible bremsstrahlung is nearly independent of pixel number, as the dependence of bremsstrahlung on wavelength is weak over this relatively small range of wavelengths. In contrast, the fit coefficient a_D for the cold D_α light is largest near the unshifted D_α line, indicating that scattered light is most important near the central line. Figure 3.6(b) also shows the reduced chi-squared χ_r^2 of the fit as a function of pixel number. For all wavelengths, χ_r^2 is much larger than unity, indicating that the simple model of Eq. 3.6 is unable to account for all of the observed variation in background. Investigation of different discharges shows that, on a particular discharge, the optimal fit coefficients a_V and a_D deviate systematically from the average fits. The likely explanation for this is that the available reference bremsstrahlung and D_α signals V and D have a different view of the edge plasma than the FIDA sightlines, so changes in the proportionality coefficients with plasma shape degrade the quality of the fits. Two other features of the χ_r^2 graph are noteworthy. First, the model does a poor job of fitting the background spectra near the blocking bar but this wavelength region is unimportant for fast-ion physics. Second, the value of χ_r^2 often jumps upward in the vicinity of impurity lines, suggesting slight imperfections in the impurity fitting. Overall, however, the fits are smooth and reasonable for the wavelengths of interest. For a typical low-density discharge ($n_e = 2 \times 10^{13}\ cm^{-3}$), approximately 65% of the

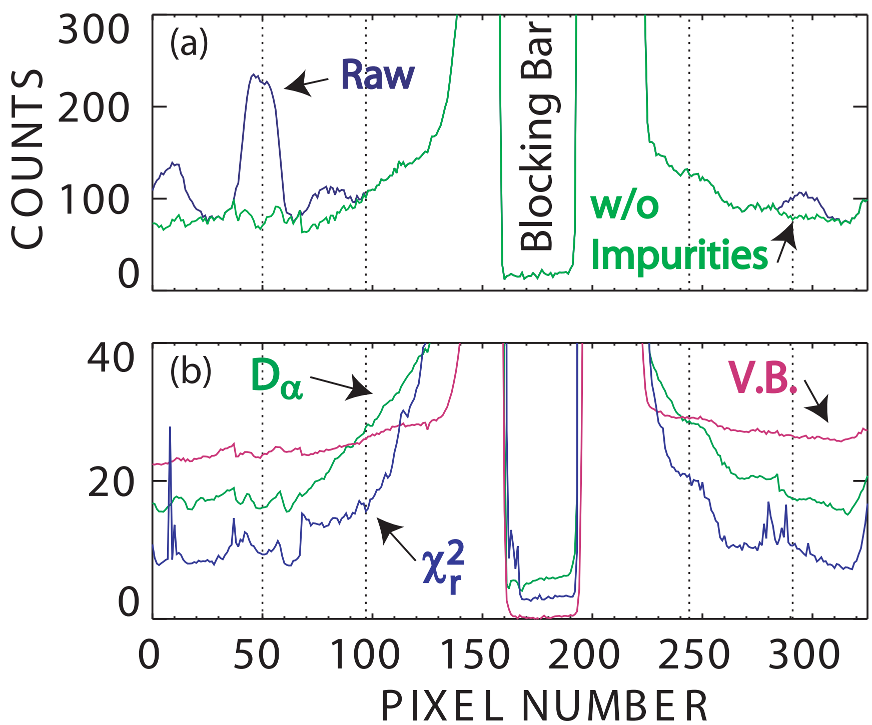

Figure 3.6: (a) A typical background spectrum before and after removal of the impurity lines. The data are from the discharge shown in Fig. 3.7 between 3141 ms and 3149 ms. (b) Fit coefficient a_V and a_D vs pixel number obtained from multiple regression on a database of over 4000 background spectra. Also shown is the reduced chi square of the fit. The dotted vertical lines indicate wavelengths that correspond to vertical energies of 30 and 80 keV.

background in the wavelengths of interest is contributed by scattered cold D_α light, with the remaining 35% attributable to visible bremsstrahlung. At higher densities, the visible bremsstrahlung becomes the dominant component of the background, since bremsstrahlung is proportional to n_e^2.

In an actual discharge with transient changes in background, the background for each pixel is taken as

$$B(\lambda, t) = c[a_V(\lambda)V(t) + a_D(\lambda)D(t)]. \tag{3.7}$$

The scale factor c, which is generally close to unity, is obtained from backgrounds near the time of interest in the particular discharge under investigation and partially corrects for the systematic variations in background associated with changes in plasma shape.

Figure 3.7 shows an example of dynamic background subtraction in the presence of a sawtooth crash. A rapid sawtooth crash occurs in less than 1 ms and redistributes fast ions [14] from the core of the plasma to outside the $q = 1$ surface; after the crash, the fast-ion density recovers on a relatively slow time scale ($\gtrsim$10 ms). In Fig. 3.7(a), the quick drop of the soft x-ray signal at 3157 ms indicates of sawtooth crash. The sawtooth causes a heat pulse to propagate from the plasma interior to the plasma edge, which causes a subsequent change in edge D_α and impurity light. Figure 3.7 (c) shows the spectra aquired by the central FIDA channel across this event. Comparison of the spectrum acquired just before the sawtooth crash (3156 ms) with the spectrum acquired just after the crash (3157 ms) shows a clear reduction in signal for wavelengths that correspond to E_λ of 30-80 keV. However, the subsequent spectra (3158 ms and 3159 ms) show that the

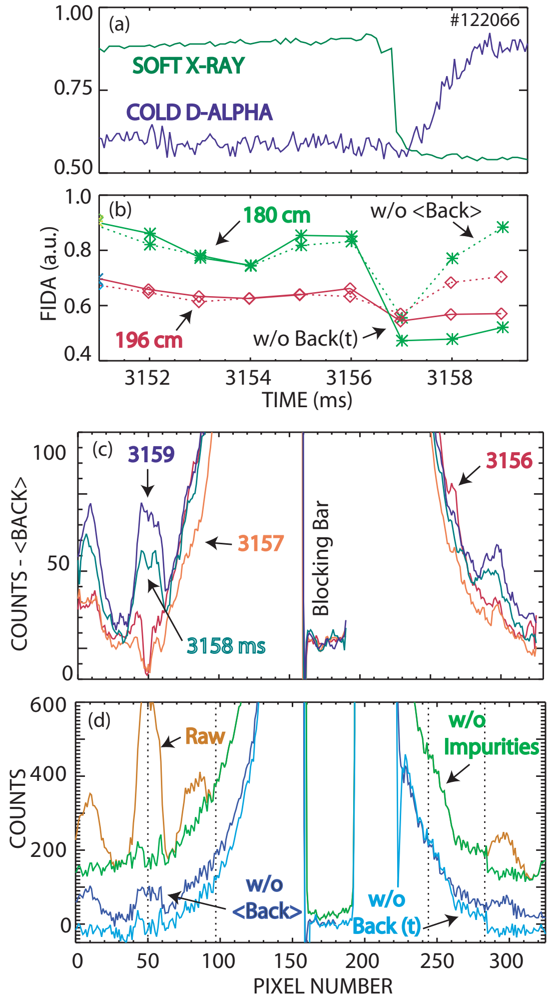

Figure 3.7: Time evolution of (a) soft x-ray signal and cold edge D_α signal and (b) FIDA signals from two chords after integration over wavelength. The solid lines employ dynamic background subtraction (Eq. 3.7), while the dashed lines use the background obtained from beam modulation. (c) Spectra from the central chord at four different times. The average background from the beam-off phase between 3141 and 3149 ms is subtracted from the raw spectra. (d) Spectra from the central chord at 3159 ms. The raw data, data with fitted impurity lines removed, data with the average background subtracted, and data with fitted impurity lines and dynamic background subtracted are all shown. Discharge conditions: line-average electron density of $2.0 \times 10^{13}\ cm^{-3}$; beam power of 3.8 MW.

impurity lines (and presumably the contribution from scattered D_α light) rise steadily as the heat pulse reaches the plasma edge.

The impact of various background-subtraction techniques is illustrated in Fig. 3.7(d) for the time slice at 3159 ms. If one uses the beam-modulation technique to correct the background, residual impurity lines appear in the spectrum; also, for wavelengths that correspond to E_λ greater than the injection energy, the signal is larger than zero, indicating contamination by scattered cold D_α light. In contrast, the procedure for correction of dynamic changes in background gives reasonable results. The impurity lines are successfully removed by fitting. Application of Eq. 3.7 makes the background above the injection energy close to zero and lowers the inferred fast-ion contribution to the signal but has a little effect on the portion of the spectrum dominated by thermal ions. The temporal evolution obtained by this background subtraction technique is also reasonable (Fig. 3.7(b)). If the average background obtained from beam modulation is employed, the inferred FIDA signal drops at the sawtooth crash but then instantly bounces back. This result is unphysical: previous measurements with, for example, neutron tomography [55] show that the fast-ion population recovers on the much slower time scale associated with beam fuelling. In contrast, with the dynamic background subtraction model, the signal from both channels drops and stays suppressed. The central FIDA channel drops by a factor of 2, while the FIDA channel that is just inside of the $q = 1$ surface drops $\sim 20\%$, which is consistent with the expected redistribution of fast ions. Prior to the sawtooth crash, when the signals are expected to be approximately constant in time, the variations are smaller with the beam-modulation technique but, overall, dynamic background subtraction is clearly superior.

In principle, the above data analysis procedure applies to the Reticon data too. In practice, the procedure can be simplified for the Reticon data. The Reticon system is very insensitive to neutron/γ hits and there are virtually no spikes caused by neutron/γ hits in the spectrum. Therefore, this step can be left out for the Retican data. Usually, the Reticon spectrometer is tuned to measure the middle part of the blue shift side, where there are no impurity lines from charge exchange and halo contribution is negligible. As a result, fittings of the impurity lines and halo emissions are not necessary for the Reticon data.

3.2 Signal level and signal-to-noise ratio

The spatial calibration and intensity calibration are done when the tokamak is vented to atmosphere. A spatial calibration is performed to determine the spatial location of FIDA measurements for each chord. First an alignment target is suspended inside the tokamak along the centerline of the viewed neutral beam. Then a neon lamp is placed on the fiber end away from the tokamak to shine backwards through the fiber and collection lens system. The spot where the light illuminates the alignment target is marked and measured. Next, an intensity calibration is completed to convert digitizer counts to number of photons. An integrating sphere source which illuminates over a broad wavelength range with a calibrated spectral radiance is placed on the spot from the spatial calibration and a spectrum is taken by the FIDA instrument with the same settings as for actual discharges.

The number of photons detected by the collection lens in each wavelength bin (pixel) for each chord during the intensity calibration is

$$P \approx L_\lambda A \cos\theta \Omega \Delta\lambda \Delta T \tag{3.8}$$

Where L_λ is the spectral radiance of the integrating sphere source in $photons.cm^{-2}.sr^{-1}.nm^{-1}.s^{-1}$, A is the source area viewed by the chord on the alignment target in cm^2, θ is the angle between the alignment target surface normal and the viewing direction, Ω is the solid angle subtended by the collection lens, $\Delta\lambda$ is the wavelength bin for the pixel in nm, and ΔT is the integration time in s. P is a function of wavelength or pixel since L_λ is a function of wavelength. The number of digitizer counts induced by the integrating sphere is the count difference between the intensity calibration shot and a dark shot. The conversion factor in photons per count is calculated by dividing the number of digitizer counts from the number of photons for each pixel. For the innermost vertical chord from the dedicated FIDA diagnostic, the conversion factor is approximately 180 for all the pixels.

The absolute signal level in terms of the number of photons can be determined by multiplying the number of digitizer counts by the conversion factor pixel by pixel and summing. It can also be estimated based on the fast-ion density, neutral density, atomic data, and geometric parameters. In order to compare the estimated signal level with experimental data, a discharge with a quiet plasma is selected. The fast-ion signal in digitizer counts is extracted from the raw data first as discussed in § 3.1. The measured signal level in photons is obtained by multiplying the fast-ion signal and the conversion factor. Since the middle portion of the spectrum is blocked, we only calculate the signal level beyond 20 keV. The result is 2.6×10^6 photons. This is the number of D_α photons from neutralized fast ions entering into the collection lens in 1 ms.

The signal in number of photons can be estimated independently by the following formula:

$$s \approx f_{>20} n_f n_n \langle \sigma v_{rel} \rangle V t \left(\frac{\nu_{3-2}}{\sum \nu_{3-n}}\right)\left(\frac{\Omega}{4\pi}\right), \tag{3.9}$$

where n_f is the fast-ion density and n_n is the neutral density. The factor $f_{>20}$ is the fraction of the fast-ion population with vertical energy greater than 20 keV. It depends on the fast-ion distribution function. The reactivity $\langle \sigma v_{rel} \rangle$ is the averaged rate coefficient for generating reneutrals in the $n = 3$ state, V is the observation volume, t is the integration time, ν_{3-2} is the radiative transition rate from $n = 3$ to $n = 2$, ν_{3-n} is the reaction rate from $n = 3$ to various states including both radiative transition and collisional transition, and Ω is the solid angle subtended by the collection lens. For the quiet discharge we have calculated the measured signal in photons for $f_{>20} \approx 11\%$, $n_f \approx 4.8 \times 10^{12}\ cm^{-3}$, $n_n \approx 1.4 \times 10^9\ cm^{-3}$, and $\langle \sigma v_{rel} \rangle \nu_{3-2} / \sum \nu_{3-n} \approx 1.0 \times 10^{-9}\ cm^3 s^{-1}$[56], so the estimated signal level is around 1.4×10^6 photons, which is reasonably close to the FIDA measurement. A more rigorous calculation of the signal level from the FIDA simulation code (Chapter 4) that includes all relevant atomic physics effect[23] gives 2.4×10^6 photons, agreeing very well with the FIDA measurement.

Both random errors and systematic errors appear in the FIDA measurements. Random errors include photo-electron noise, readout noise and dark noise. Photo noise refers to the inherent natural variation of the incident photon flux on each CCD pixel; it equals the square root of the number of collected electrons. The number of collected electrons is the product of the signal in digitizer counts and the gain, which is 2.93 electrons per count when the camera operates at high gain.

Readout noise refers to the uncertainty introduced during the process of quantifying the electronic signal on the CCD. It is about 15 electrons at a 0.5 MHz digitizing rate. Dark noise arises from the statistical variation of thermally generated electrons within the silicon layers comprising the CCD. It is reduced dramatically when operating at low temperatures and is proportional to the integration time. Since the PixelVision CCD camera is thermoelectrically cooled and the integration time is 1 ms, dark noise is negligible in the FIDA measurements. The signal to noise ratio (SNR) is given by,

$$SNR = \frac{gN_c}{\sqrt{gN_c + N_r^2}}, \tag{3.10}$$

where g is the gain, N_c is the digitizer counts, and N_r is the readout noise. The SNR is a function of wavelength. For the pixels on the two wings of the spectrum, N_c is on the order of 100 and photo-electron noise is comparable to readout noise. For the central pixels, N_c is on the order of 1000 and photo-electron noise becomes dominant. The above calculation is for raw data. For steady plasmas, the fast-ion signal is extracted by averaging beam-on and beam-off signals in a chosen time window and doing background subtraction. Assuming N_{on} is the average number of beam-on signals in counts, N_{off} is the average number of beam-off signals in counts, and N_t is the number of time slices averaged for beam-on and beam-off, the fast-ion signal in electrons is

$$S_{fi} = g(N_{on} - N_{off}). \tag{3.11}$$

The standard deviation of averaged beam-on signals in electrons is

$$\sigma(on) = \frac{\sqrt{gN_{on} + N_r^2}}{\sqrt{N_t}}. \tag{3.12}$$

The standard deviation of averaged beam-off signals in electrons is

$$\sigma(off) = \frac{\sqrt{gN_{off} + N_r^2}}{\sqrt{N_t}}. \tag{3.13}$$

Adding the above two contributions in quadrature, we obtain the standard deviation of the net signal (fast-ion signal), which is

$$\sigma(fi) = \sqrt{\frac{g(N_{on} + N_{off}) + 2N_r^2}{N_t}}. \tag{3.14}$$

The signal to noise ratio is

$$SNR = \sqrt{N_t}\frac{g(N_{on} - N_{off})}{\sqrt{g(N_{on} + N_{off}) + 2N_r^2}}. \tag{3.15}$$

Not surprisingly, the signal to noise ratio is better for the central pixels since the difference between the beam-on and beam-off counts is much larger. To improve the signal to noise ratio for a certain pixel, we can average our signal over a larger time window. However, the above formula assumes that there are only random errors. This holds true approximately in quiescent plasmas. In plasmas with instabilities, dynamic changes in background introduce systematic errors that invalidate large time windows. Systematic errors strongly depend on plasma conditions and should be addressed case by case.

An example of random errors in a quiescent plasma is shown in Fig. 3.8.

The dominant errors in the FIDA measurements are the uncertainties associated with background subtraction. When the FIDA "density" is shown, the uncertainty in calculation of the injected neutral density contributes additional uncertainty. The

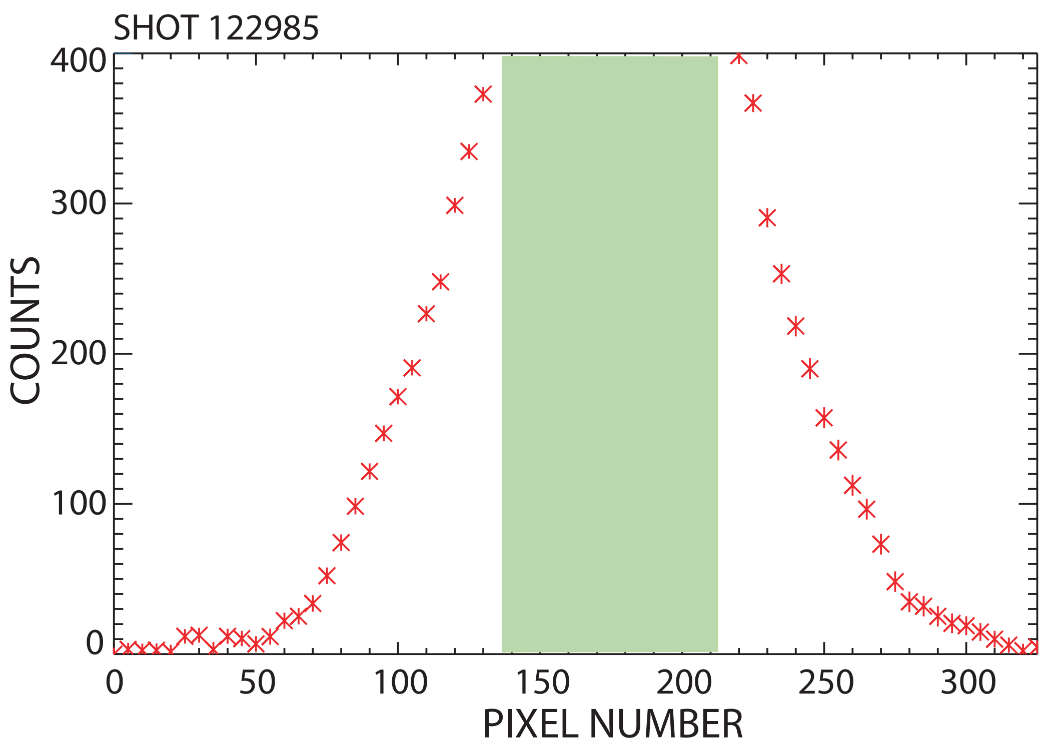

Figure 3.8: Random error bars. The error bars are calculated using Eq. 3.14 with $N_t = 10$.

error associated with background subtraction is readily calculated. The FIDA signal $S = T - B$, where T is the total signal and B is the background. An ensemble of N_T measurements of T are obtained when the diagnostic beam is on; these data have mean $\langle T \rangle$ and standard deviation σ_T. Similarly an ensemble of N_B measurements of B are obtained when the beam is off that have mean $\langle B \rangle$ and standard deviation σ_B. The FIDA signal is $\langle T \rangle - \langle B \rangle$ and the one-sigma error is $\sigma = \sqrt{\sigma_T^2 + \sigma_B^2}$. For the FIDA "density," this uncertainty is added in quadrature with the estimated error in the injected neutral density (typically 10%).

The FIDA relative profile measurements depend on six quantities: T_1, B_1, T_2, B_2, n_1 and n_2, where the subscripts represent the first and second time intervals for the measurements (with and without ICH) and n_1 and n_2 are the injected neutral densities. The relative signal is $S = (n_2/n_1)(\langle T_1 \rangle - \langle B_1 \rangle)/(\langle T_2 \rangle - \langle B_2 \rangle)$. The fractional uncertainty due to the background subtraction is

$$\frac{\sigma}{S} = [\frac{\sigma_{T1}^2 + \sigma_{B1}^2}{(\langle T_1 \rangle - \langle B_1 \rangle)^2} + \frac{\sigma_{T2}^2 + \sigma_{B2}^2}{(\langle T_2 \rangle - \langle B_2 \rangle)^2}]^{1/2}. \tag{3.16}$$

The uncertainty in the relative injected neutral density adds in quadrature, as before.

3.3 Common practices

The raw FIDA data are a two-dimensional array in pixels and time. Each pixel corresponds to a specific wavelength (λ), which translates into a velocity or energy (E_λ) through the Doppler shift formula. Note that E_λ is the energy component of the reneutral along the viewing line, instead of the total energy. The standard procedure discussed in § 3.1 of analyzing the FIDA data is applied as follows: First, unusable time slices are removed, for instance, those contaminated by edge localized modes (ELMs). Second, contaminated pixels by neutron/γ hits are replaced with an average of the neighboring pixels. After the above initial processing, background subtraction is essential to remove contaminants such as scattered light, visible bremsstrahlung, non charge-exchange impurity lines, etc. In quiet plasmas, we usually do background subtraction via beam modulation. A certain time window during which the plasma is steady is selected first. Then beam-on and beam-off spectra are averaged over the time window. The averaged beam-off spectrum is subtracted from the averaged beam-on spectrum next. The resultant spectrum has two impurity lines excited by charge exchange and the halo line, which are removed by fitting. The final spectrum is the pure FIDA spectrum that can be analyzed in various ways. A common practice is to average over a certain E_λ window to quantify the FIDA signal strength using a single number. The FIDA signal is proportional to the fast-ion density, the neutral density, and the averaged reaction rate because of the charge exchange reaction. The averaged reaction rate depends on the fast-ion velocity distribution function, which is determined by Coulomb collisions in quiet plasmas without RF heating. In such plasma conditions, the averaged reaction rate is insensitive to plasma conditions and can be assumed to be a constant. To generate a quantity that is proportional to the fast-ion density, we often divide the FIDA signal by the neutral density. We call this quantity FIDA density. The error bar associated with random errors can be estimated assuming the spectra are stationary in the selected time window. The standard deviations of the averaged beam-on signal and beam-off signal are calculated first based on the ensemble of the beam-on and beam-off time slices. The error bar is the square root of the sum of squares of the standard deviations.

Chapter 4

FIDA simulation code

4.1 Code structure

The FIDA diagnostic is a one-dimensional measurement in velocity space. It is theoretically impossible to convert the FIDA spectrum to a fast-ion distribution function [57]. Nevertheless, for a specific fast-ion distribution function, the FIDA spectrum can be predicted. The FIDA spectral shape is distorted with respect to the one-dimensional velocity space shape by various atomic rates, especially the charge exchange rate between fast ions and neutrals. Moreover, for each specific wavelength Doppler shift, a collection of fast ions with different energies and pitch angles contributes to the spectral intensity. The weighting in velocity space is complicated [27](§2.1). The complex nature of the problem of converting a fast-ion distribution to the FIDA spectrum makes simulation the only solution.

The simulation code begins with a steady state calculation of the beam and halo neutral distributions in real space, velocity space, and energy levels. Since the neutral beam source is modulated, only reactions with injected neutrals and halo neutrals are relevant. (Theoretically, the halo neutral distribution forms on a timescale that is much shorter than the typical 10 ms duration of the modulated beam pulse. Any changes in edge neutrals during a beam pulse are ignored.) Then, with this fixed background, a Monte Carlo calculation follows the spatial trajectories, energy level transitions, and radiated spectra of the neutralized fast ions.

There are many possible principle quantum numbers n and angular momentum states l available to the neutrals. The strong fine-structure mixing allows the assumption that the population of each quantum state may be grouped as a single population based on the principle quantum number [58]. The required cross sections and reactivities are available in the literature and in the Atomic Data and Analysis Structure (ADAS) compilation [59, 60]. Cross sections for the charge-exchange reactions between fast ions and neutrals in states $n = 1 - 4$ are given in ADAS [59]. (States with $n > 4$ are neglected in our calculations because these energy levels are sparsely populated and the cross sections seem uncertain.) Hydrogenic rates are evaluated using the relative velocity between the fast ion and the neutral, $|\mathbf{v}_f - \mathbf{v}_n|$, where $\mathbf{v}_f$ is the fast-ion velocity at the instant of neutralization (Fig. 2.1). Since the electron distribution function is Maxwellian and the electron thermal speed is much greater than the fastest neutrals, it is expedient to work directly with the reactivities $\langle\sigma v\rangle$ for electron collisions with neutrals. Expressions for electron impact ionization as a function of electron temperature T_e and energy level n appear in Ref. [61]. Formulas for electron excitation from one energy level to another are in Ref. [62]. A simplification is also possible for collisions with carbon. (Carbon is the principal impurity species in DIII-D .) In this case, the neutral speed is much greater than the carbon speed so the reactivity only depends on the fast-ion speed v_f. Impurity cross sections are listed in Eqs. 13-16 of Ref. [63]. Neutral collisions with hydrogenic ions are more demanding computationally. For these collisions, the speeds of the ions are often comparable to the neutral speed, so it is necessary to average the reactivity over the ion distribution function, which is assumed to be a drifted Maxwellian with temperature T_i and rotation velocity $\mathbf{v}_{rot}$. Equations 9 and 10 of Ref. [63] give the cross section for proton excitation and impact ionization from the ground state, while Ref. [64] contains cross sections for excitation from higher states. Combining the three species, a typical collisional excitation rate coefficient (for excitation from the ground state to the $n = 2$ state) is $Q_{12} = n_e \langle \sigma v \rangle_{12}^{coll,e} + n_d \langle \sigma v \rangle_{12}^{coll,d} + n_C \sigma_{21}^{coll,C} v_n$, where n_e, n_d, and n_C are the electron, deuteron, and carbon densities. For all species, deexcitation rates are derived from the principle of detailed balance, i.e., $\langle \sigma v \rangle_{u \to l} = (n_l^2/n_u^2) \langle \sigma v \rangle_{l \to u}$, where u and l represent the upper and lower quantum numbers, respectively. The radiative transition rates are given by the Einstein coefficients.

The structure of the simulation code is outlined in Fig. 4.1. Because neutrals travel in straight lines, a Cartesian grid is employed and is a great simplification relative to flux coordinates. There are several subroutines that are used both in the initial calculation of the beam neutral and halo neutral distributions and in the main fast-ion loop. One subroutine finds the neutralization rate to various quantum states for an ion that charge exchanges with a neutral in state n. A second basic subroutine calculates the track of a neutral through the Cartesian grid, returning the length of the track in each "cell." A third subroutine solves the time-dependent collisional-radiative equations [45] for the neutral density in each state, given initial state populations, the rates for collisional excitation and deexcitation, and the radiative transition rates. A fourth subroutine calculates the Stark [65] and Doppler shifts of emitted photons given the local electric and magnetic fields and the velocities of the neutral and the photon. (The detector is assumed to measure all emitted polarizations.)

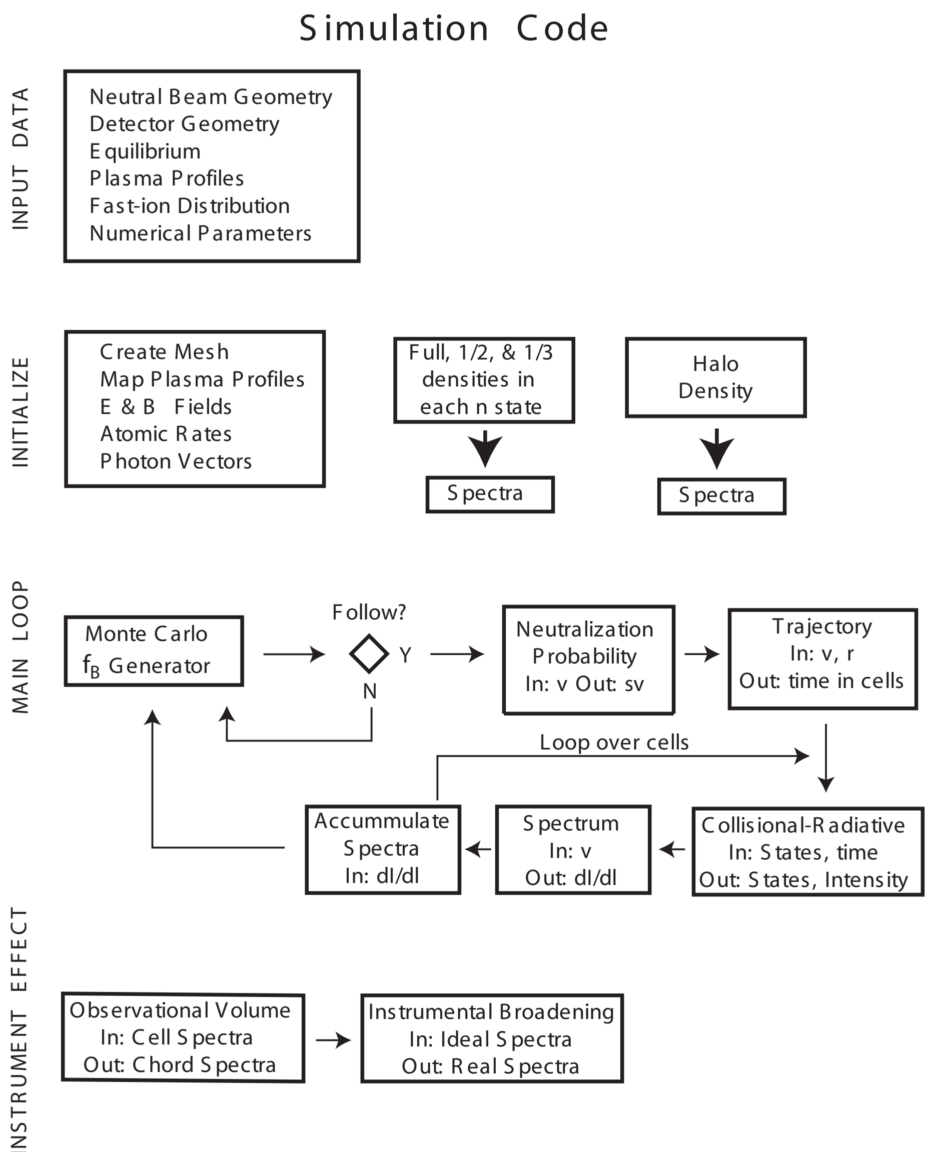

Figure 4.1: Flow diagram for the simulation code.

The geometry of the injected beam, the position of the detector, and the magnetic and electric fields calculated by the EFIT equilibrium code [13] are input to the code. Profiles of electron density and temperature, ion temperature and rotation, and carbon density as a function of flux surface are also given. The fast-ion distribution function f_f as a function of E, $v_{\parallel}/v$, and $\mathbf{r}$ is specified using, for example, an analytical model, a Fokker-Planck calculation [66], or a numerically produced distribution such as the TRANSP [12] code. The fast-ion distribution function from TRANSP is a function of zones spatially; however the FIDA simulation code requires the distribution function to be a function of grids established along the neutral beam. Each grid usually crosses several zones in TRANSP. To map the fast-ion distribution function, each grid is divided into smaller subgrids. If the center of a subgrid is in a zone, the entire subgrid is considered to be in that zone. The weight of each zone is the number of subgrids it contains divided by the total number of subgrids for the grid. The mapped fast-ion distribution function is the weighted sum of the distribution functions from all the zones. The integral of the mapped distribution function over energy and pitch is normalized to be the fast-ion density at the grid.

The code begins with a set of initial calculations. First a regular Cartesian mesh is established along the centerline of the injected beam. Then the plasma parameters and electric and magnetic fields are mapped from flux coordinates onto this mesh. Next, all atomic rates that do not depend on the neutral velocity are computed, such as the collisional ionization of neutrals by electrons. The direction of the velocity vector from each cell to the collection optics is also calculated. All of these quantities are stored in a large structure.

The next step is to calculate the neutral populations that will eventually charge exchange with the beam ions. Using the known beam geometry and divergence, the collisional-radiative equations for the injected neutrals are solved. The densities and velocities of the full, half, and third neutrals (each as a function of energy level n) are added to the structure that describes each cell. Charge-exchange events for the injected neutrals are the source of halo neutrals. A Monte-Carlo procedure calculates halo diffusion. If a charge exchange event happens in a cell, the particle is restarted with a new random velocity based on the local ion temperature and rotation. The neutral is followed until it ionizes. The energy occupation levels are approximated by the steady-state collisional-radiative balance. At the completion of the halo calculation, the halo densities (as a function of n) for each cell are stored.

After all of these preliminaries, the program enters the main loop, which is a weighted Monte Carlo routine. The product of fast-ion density n_f and the sum of injected neutral and halo neutral densities $\sum n_n$ has already been calculated as a function of position. This estimate of the probability of a reaction (which neglects the computationally intensive dependence of the reaction rate on the relative velocity) is used to determine how many fast neutrals to launch from each cell. The initial position of the fast neutral within the cell is selected randomly. The initial velocity is found using a Monte Carlo rejection test in the two dimensions that describe the velocity distribution (energy and pitch), the gyroangle is randomly generated, and the velocity vector is transformed into Cartesian coordinates. With the velocity now specified, the actual reaction rate of the fast ion with each of the neutral populations can be computed; the sum of these rates is the weight of this particular fast neutral. (In fact, each individual fast neutral represents the set of possible n states of neutrals along the selected trajectory.) The trajectory of the fast neutral through the cells is computed next. As the fast neutral travels through each cell, the time-dependent collisional-radiative balance between states is computed, including the number of D_α photons that are emitted. The spectrum of the emitted photons is also computed. Finally, the properly weighted spectrum is added to the accummulated spectra in each cell.

The output of the main program is the spectra from each cell. To simulate the signal from the actual instrument, two steps should be taken. The spectra from individual cells should be summed over the obervational volume for each chord first. Note that some cells are partially inside the observational volume. Concequently, weights between 0 and 1 based on the fraction of the cell volume inside the observational volume are assigned to those cells while summing. The second step is to artificially add instrumental broadening to the simulated chord spectra. The "real" spectra that can be compared with the measured spectra are the convolution of the simulated chord spectra from step one and the instrumental response function (Fig. 3.2).

Several benchmarks of the code were performed. Results in Mandl's thesis [67] checked several lower-level routines. To test the collisional-radiative model, the attenuation of the injected neutral beam was compared with an independent calculation [68]. The spectral calculation and the weighted Monte Carlo scheme were verified as follows. As part of our initial investigation of the feasibility of this concept, a simplified model of the expected spectra was developed that ignores atomic physics and assumes that the magnetic field is purely toroidal. Figure 2.4 shows a result calculated by this code.) To test our full simulation code, we replaced the magnetic field with a toroidal field and modified the cross sections to be independent of velocity. The resulting spectra were consistent with the output of the simple model.

4.2 Algorithms to improve running speed

The running time of the simulation code is proportional to the number of reneutrals launched and roughly scales as $\sqrt[3]{n_g}$ in which n_g is the number of grids established along the beam line. The multiple-dimension nature of the fast-ion distribution function requires a large number of reneutrals (usually 10 Ms) to be launched. n_g is determined by the volume of region of interest and the grid size. The largest grid size can be set around the intrinsic spatial resolution of the diagnostic which is ~ 5 cm.

With fixed number of reneutrals launched and number of grids, a few algorithms are employed to improve the running speed of the code. To decide exactly how many reneutrals should be launched in each cell based on the neutral distribution and the fast-ion distribution is very demanding computationally because of the dependence of the reaction rate on the relative velocity. The exact number of reneutrals is proportional to $n_n n_f \langle\sigma v\rangle$, where $\langle\sigma v\rangle$ is averaged over the velocity distribution of the neutrals and the velocity distribution of the fast ions. To simplify the calculation, $n_n n_f$ is used to estimate the number of reneutrals in each cell. The initial velocity is found using a Monte Carlo rejection test in the two dimensions that describe the velocity distribution. With the velocity now specified, the actual reaction rate of the fast ion can be computed; the reaction rate is assigned to be the weight of the particular neutral. With the number of reneutrals determined, the most time consuming part of the code is to form and solve the collisional-radiative differential equations. Most of the coefficients of the differential equations are the reaction rates of reneutrals with thermal ions, electrons and impurities. In general, reactivity $\langle\sigma v\rangle$ for collisions depends on the relative velocity. To simplify, we assume that $v_e \gg v_f \gg v_c$. For electron collisions with reneutrals, the reaction rate is merely a function of electron temperature, and for carbon collisions with reneutrals, the reaction rate is merely a function of reneutral velocity. However, for thermal ion collisions with reneutrals, the speeds of the ions are often comparable with the reneutral speed, which means the reaction rate should be averaged over the ion distribution function. The reaction rate is basically a function of ion temperature and reneutral energy relative to the plasma frame. In a naive way, the reaction rate is computed for each reneutral in each cell, which is redundant and very time consuming. A smart way is to calculate a table with reaction rate over all possible ion temperature and all possible re-neutral energy before hand. The table does not depend on any specific conditions, so it only needs to be done once. Then for each reneutral in each cell, the task is to pick up the right element in the table based on ion temperature and reneutral energy. In fact, this technique has improved the code speed dramatically. Although reactivity calculation for carbon collisions is not as computationally demanding, setting up a table for carbon with reaction rate as a function of reneutral energy turns out saving quite a bit running time. The core calculation in this code is to solve a set of ordinary differential equations in multiple time steps for each cell, which is accomplished by the fourth-order Runge-Kutta method. IDL does supply a rk4 subroutine, but surprisingly, a self-written rk4 subroutine outperforms the one provided by IDL. Because this routine is called millions of times, the effort is paid off. A varying time step approach is adopted to optimize the number of times to solve the differential equations. With all the above improvements, the running time of the code is reduced to around 30 hours on a 3 GHz Intel Xenon processor.

4.3 Sensitivity study

Plasma profile uncertainties influence the calculated FIDA signals via three distinct physical mechanisms. One mechanism affects the atomic radiative-collisonal calculations, a second mechanism affects the calculations of the neutral density, and a third modifies the beam-ion distribution function. The signal strength is proportional to both the neutral density and the beam-ion density.

To assess the influence of these uncertainties on the calculated FIDA spectra at various radial locations, a systematic modeling study has been undertaken. We analyzed a typical DIII-D L-mode plasma (122060 at 2.05 s) heated with two 80 keV beams, and modulated power between 2.5 and 5.0 MW. The central plasma density and temperature at the time of interest were $n_e(0) = 4.0 \times 10^{13}\ cm^{-3}$ and $T_e(0) = 3.0$ keV. Individual plasma profiles, such as electron density and temperature, ion temperature and Z_{eff}, were scaled up and down by 20% across the entire plasma column and the calculated spectra were compared with the baseline spectra, where unmodified experimental profiles were used.

Monte Carlo (MC) simulations with 10^7 particles were necessary to obtain satisfactory spectra. Identical random seed was used in all simulations to eliminate the effect of the MC noise. Separate simulations with arbitrary seed numbers had shown that this noise level is about $\pm 2\%$ for a 10^7 particle simulation. The MC statistics are much worse for particles with energies above 70 keV because too few beam ions have such high vertical energy (E_λ). It takes about 30 hours on a 3 GHz Intel Xenon processor to calculate the spectra at 10 radial locations.

Since FIDA signals typically vary over three orders of magnitude in the spectral range of interest, it is necessary to calculate ratios of signals from simulations with modified plasma profiles, to those with the baseline profiles.

We focus now on the modeling results for a vertical channel 4 cm away from the plasma center ($R_0 = 176$ cm) - the effect on channels further away is smaller. It was found that T_e and T_i plasma profile variations affect the atomic radiative-collisonal calculations close to the MC noise level, and thus can be ignored. The influence of the electron and ion temperature variations on the calculated FIDA spectra via the effect on the calculated neutrals is similar; however, the electron density variation has about three times larger influence and can not be ignored (Fig. 4.2). Note that in all these simulations the beam-ion distribution function from the baseline TRANSP model was used.

Higher electron density lowers the injected neutral density by increasing the electron impact ionization of neutrals; higher ion density increases charge exchange with thermal ions. For a given beam-ion distribution function, the smaller neutral density leads to weaker FIDA signals, as seen on Fig. 4.2, where 20% increase in the electron density is responsible for a $\sim 7\%$ reduction of the calculated FIDA signal due to the impact on neutrals alone.

FIDA diagnostics are designed for indirect measurement of the beam-ion distribution function, thus useful FIDA spectra require sensitivity to variations. Energetic ions in DIII-D plasmas slow down on both electrons and thermal ions.

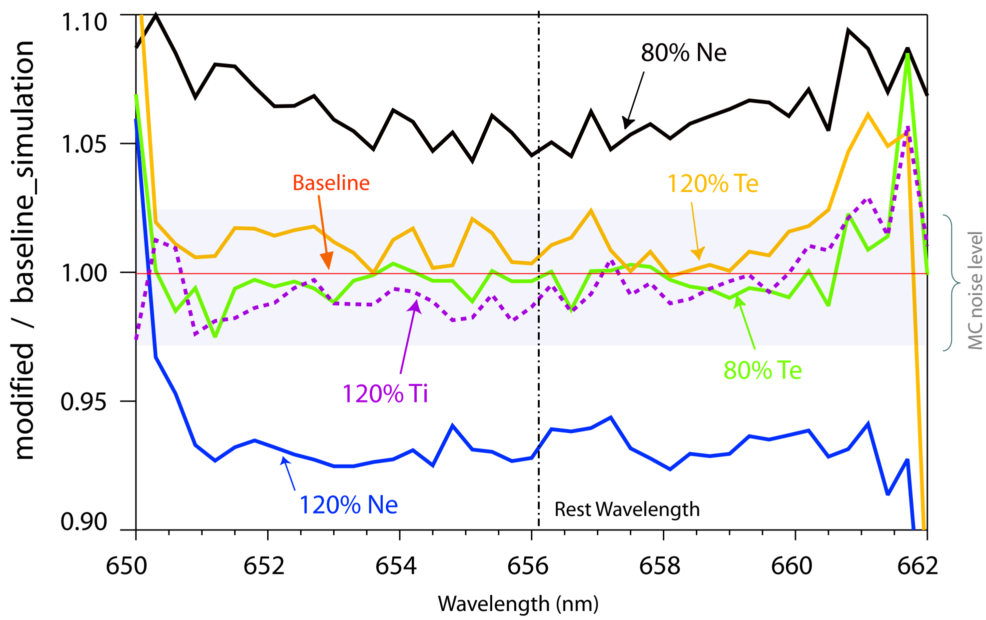

Figure 4.2: Changes in the calculated FIDA signal at $R = 180$ cm caused by changes in neutral density associated with variations in plasma parameters.

The corresponding beam-ion slowing down time on electrons in the absence of MHD activity is:

$$\tau_{sl,e} \sim T_e^{3/2}/n_e \tag{4.1}$$

Lower electron temperature or higher density lead to shorter slowing down times and lower beam-ion densities, i.e. weaker FIDA signals. The opposite is true for higher temperatures and lower densities. These conclusions are corroborated with Fig. 4.3, where modeling results from FIDA simulations with modified beam-ion distribution functions are shown. These functions were obtained from TRANSP simulations where a single plasma profile was uniformly scaled up or down by 20%. To provide sufficiently smooth beam-distribution functions, all TRANSP runs in this study used 100,000 beam-ion particles.

Impurity density variations are also expected to affect the beam-ion distribution function. We studied this effect by scaling Zeff in TRANSP by ±20%. Higher Zeff implies stronger pitch angle scattering of the beam ions into the higher energy range ($>$ 30 keV). The expected increase in the FIDA signal strength for $E >$ 30 keV was indeed observed, and was in the $5 - 10\%$ range.

Figure 4.2 and Figure 4.3 show that the electron density uncertainty has a compounding effect on the calculated FIDA signals: n_e variations alter the spectra due to the change in neutral density and the beam distribution function in the same direction. Another important question is how profile changes in the inner half of the plasma column alter the calculated spectra. In DIII-D , fitting of the measured electron densities with the Thomson scattering diagnostics introduces the largest uncertainties in the plasma center. Modeling results addressing these questions are shown on Fig. 4.4. By lowering ne everywhere by 20%, the FIDA signal at

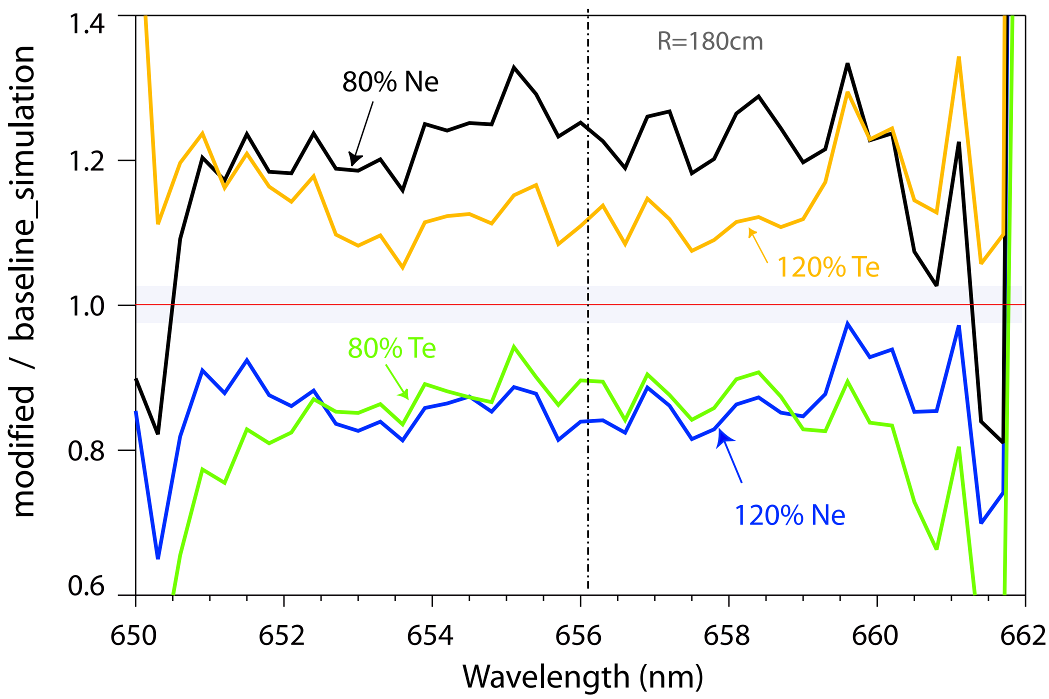

Figure 4.3: FIDA signals are sensitive to modifications of the beam-ion distribution function due to plasma profile uncertainties.

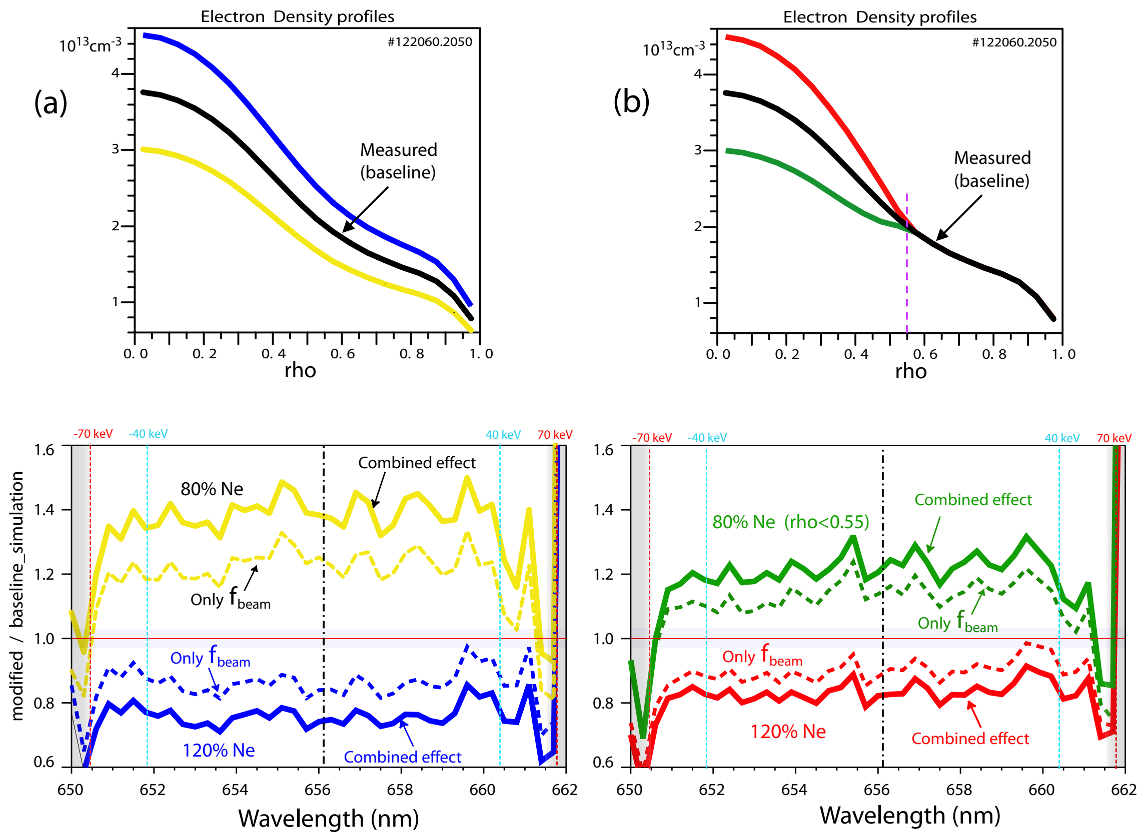

Figure 4.4: FIDA signal sensitivity due to combined effect of n_e on neutrals and f_b: (a) uniformly scaled profile (b) profile scaled in the inner half.

Table 4.1: FIDA signal response to uniformly 20% increase of various parameters

Plasma parameters	atomic rates		Neutrals		Fast ions		Total effects	
	Inner chord	Outer chord	Inner chord	Outer chord	Inner chord	Outer chord	Inner chord	Outer chord
$n_e(+20\%)$	—	—	−7%	+3%	−17%	−14%	−24%	−12%
$T_e(+20\%)$	0%	0%	1%	0%	+11%	+17%	—	—
$T_i(+20\%)$	−2%	−2%	−1%	−3%	—	—	—	—

$R = 180$ cm increases by $\sim 35\%$. n_e lowered by 20%, just in the inner plasma half, increases the signal by $\sim 20\%$. The n_e increase has somewhat smaller effect: $\sim 25\%$ and $\sim 20\%$ signal decrease, respectively. Density variations influence the outer channels less, and the influence for the most peripheral channels ($R \approx 210$ cm) decreases to about half ($< 20\%$) of that for the central channels (not shown).

The sensitivity study results are summarized in Table 4.1. The plasma parameters are uniformly increased by 20% and the resultant changes of the FIDA signals are listed. Since the effect varies across the radial location of the chords, two representative chords are chosen with the inner chord at 180 cm and the outer chord at 212 cm. The effect on other chords can be estimated based on their chord locations. The dashed cells mean that the study has not been done yet. Mostly, it is because the expected effect is trivial or could be inferred. Note that the effect on Zeff is not listed. The resultant spectrum is not uniformly affected, and for some reason, the spectral ratio is very noisy.

Our choice of varying plasma parameters by 20% was motivated by the desire to observe clear trends and produce easily distinguishable results. As expected, the uncertainty in the electron density profile affects the calculated FIDA spectrum the most. In reality, for DIII-D this uncertainty is about 10%, so the ultimate uncertainty for all calculated spectra should be in the $15 - 20\%$ range.

Chapter 5

Measurements in quiet plasmas

The FIDA diagnostic is a new diagnostic technique. Before utilizing this diagnostic to study fast-ion transport by collective instabilities or fast-ion acceleration by ICH, a thorough benchmark is required to validate this novel technique. MHD-quiescent plasmas provide an ideal testbed for this purpose since fast ions decelerate classically and hardly diffuse in such quiet plasmas with dilute fast-ion populations [14]. Meanwhile, measurement in quiet plasmas also helps us understand the FIDA diagnostic in a profound way. The results in this chapter were obtained over two periods. Section 1 presents the proof-of-principal data taken in 2003 by the CER system. The remaining sections show the results with the dedicated FIDA diagnostic and the Reticon system in 2005.

5.1 Proof-of-principal preliminary data

As an initial test of the concept, the spectrometer of the DIII-D charge-exchange recombination spectroscopy (CER) diagnostic [8] was shifted from its usual wavelength to the D_α transition. The first test with a tangential view of the beam, shown in Fig. 2.3(b), highlighted the difficulties. After realizing the importance of exploiting the perpendicular gyromotion to avoid the bright interfering lines, an observation with the fibers at the 15° midplane port was attempted. With this radial view (Fig. 2.3(a)), the injected neutrals are moving away from the detector so their D_α emission is red-shifted. This view is nearly perpendicular to the magnetic field, so the fast-ion gyromotion produces a large Doppler shift in both directions, as in Fig. 2.4. The CER diagnostic cannot span the entire spectral range of interest, so the instrument was tuned to view the uncontaminated blue portion of the spectrum and to just miss the bright central line produced by the edge and halo neutrals.

A typical discharge for the experiments with the radial-view data is shown in Fig. 5.1. Several neutral beams inject into the discharge but only one source injects neutrals in the sightline of the detector. This source steadily injects at the beginning of beam injection from 1.9-2.7 s, is off while other sources inject from 2.7-3.8 s, steadily injects again for the next 0.7 s, and then is modulated by a square wave from 4.5-5.0 s. When the viewed source is off, other sources replace it so, to a first approximation, the fast-ion distribution function is steady throughout the discharge. There are some changes in electron density (and other plasma parameters), however, so the conditions are not perfectly constant. After an initial rise, the neutron rate, which is dominated by reactions between the fast ions and the thermal deuterons for these conditions, is nearly constant, so the changes are modest.

Figure 5.2(a) shows the spectrum at the onset of beam injection. During the first 30 ms of injection a broad feature appears between 652-654 nm in the spectrum (Fig. 5.2(b)). No feature appears below 650 nm, which corresponds to a larger Doppler shift than can be produced by an 81 keV atom. (The neutral beam injection energy is 81 keV.) The feature is fully formed in ~ 40 ms; similarly, the neutron rate completes 75% of its initial rise after 40 ms, then gradually increases for the next 40 ms.

In contrast, the behavior is quite different when the viewed beam comes back on

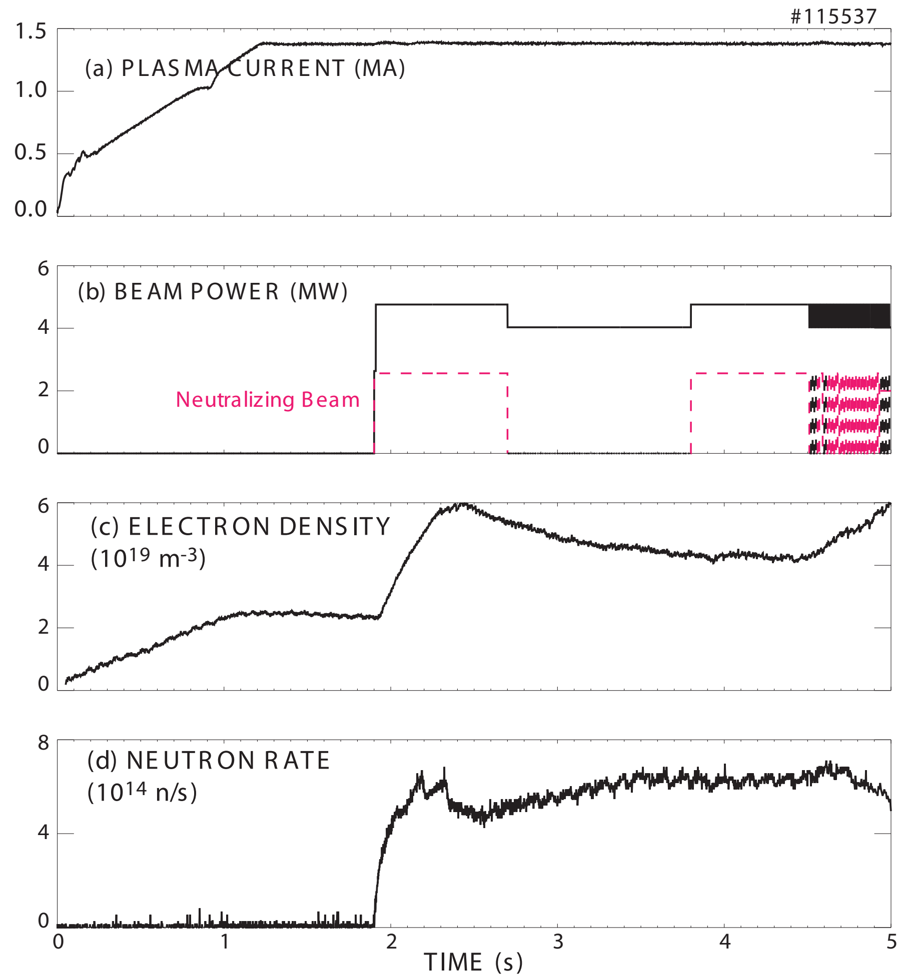

Figure 5.1: Time evolution of (a) plasma current, (b) total beam power (solid line) and power from the source viewed by the detector (dashed line), (c) line-average electron density, and (d) 2.5 MeV neutron rate for the discharge shown in Figs. 5.2 and 5.3. Toroidal field $B_T = 1.7$ T; lower single-null divertor configuration; central electron temperature $T_e \simeq 3$ keV.

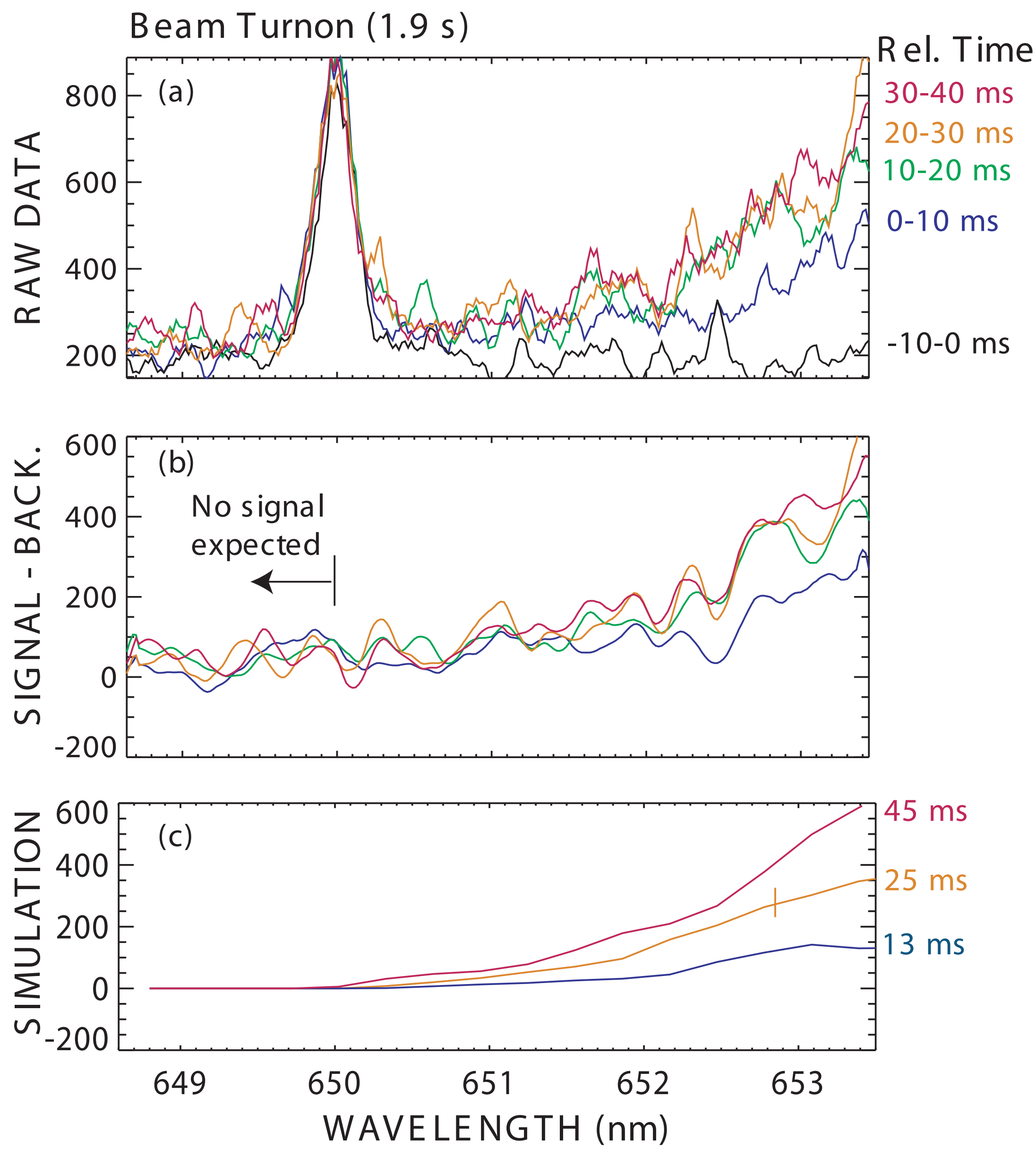

Figure 5.2: (a) Spectra in 10-ms time bins at the onset of beam injection at 1.9 s for the discharge shown in Fig. 5.1. (The peak at 650 nm is an edge impurity line.) (b) Spectra after subtraction of the 0-10 ms time bin. (c) Spectra predicted by the simulation code. A typical relative error associated with Monte Carlo statistics is represented by the vertical line; systematic errors associated with uncertainties in the input data are probably larger.

at 3.8 s (Fig. 5.3). In this case, the fast-ion distribution function is already established because other beam sources have been injecting continuously. The signal immediately jumps up to its asymptotic value, as expected.

The spectra predicted by the simulation code (Fig. 5.2(c)) is similar in shape to the observed spectra (Fig. 5.2(b)). The predicted shape increases rapidly with increasing wavelength because, for these plasma conditions, injected fast ions have large parallel velocities and can only obtain a substantial perpendicular velocity through pitch-angle scattering. The predicted temporal evolution agrees qualitatively with the data but, quantitatively, the simulation predicts a more gradual increase in signal than observed. This discrepancy is probably caused by uncertainties in the experimental inputs to the simulation. The predicted increase in neutron emission (not shown) agrees well with the measured neutron rate.

The latter portion of the discharge, when the viewed beam is modulated, is particularly convenient for background subtraction and for a study of the electron density dependence of the signal. Figure 5.4 compares the spectra for a low-density ($\bar{n}_e = 1.1 \times 10^{19}\,\mathrm{m}^{-3}$) and a high density ($\bar{n}_e = 10.3 \times 10^{19}\,\mathrm{m}^{-3}$) discharge. Three features are evident. The wing of the line produced by halo (thermal) neutrals appears on the right side of the figure (near the unshifted line). The central ion temperature in these discharges is $\lesssim$3 keV, so the expected Doppler broadening of this feature is ~ 0.8 nm, in good agreement with the measurement. The signal between 652-654 nm is associated with gyrating fast ions. The minimum wavelength expected for 81-keV deuterons is ~ 650 nm; in fact, since it is predominately the perpendicular component of the velocity that contributes to the blue shift in this measurement, wavelengths smaller than 651 nm should be rare. The third feature in

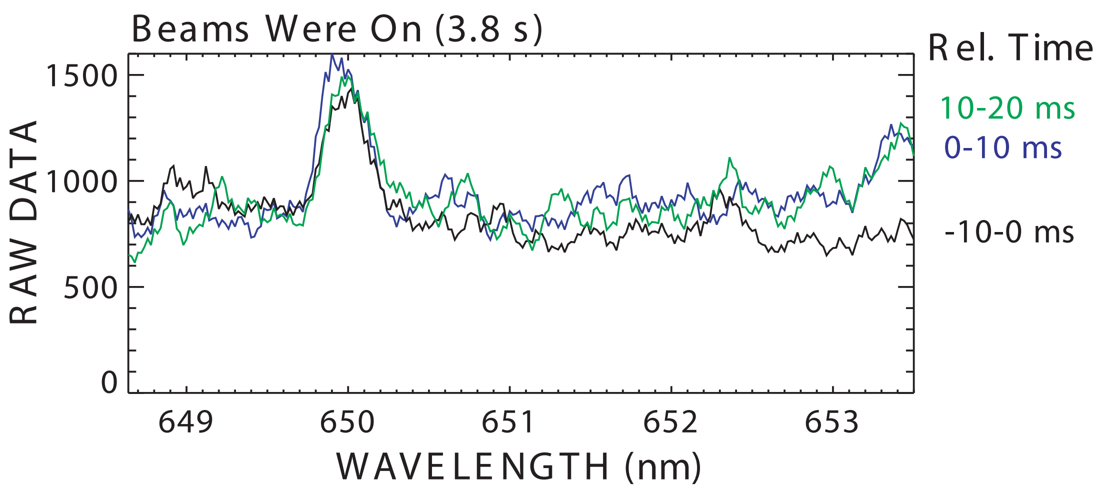

Figure 5.3: Spectra in 10-ms time bins at the resumption of injection by the 30° beam at 3.7 s for the discharge of Fig. 5.1.

the spectra is a broad featureless background associated with visible bremsstrahlung that increases rapidly with increasing electron density.

As in the previous example, the observed fast-ion spectral shape is in good agreement with the shape predicted by the simulation code (Fig. 5.4(a)). The predicted reduction in the fast-ion feature in the high-density discharge is in qualitative agreement with the observation (Fig. 5.4(b)) but the predicted reduction is larger than observed (for reasons discusses below).

To check the identification of these features, Fig. 5.5 shows the density dependence of these three features in a sequence of discharges with the same beam modulation pattern, plasma current, and beam power but with different values of electron density. (Only discharges with $\lesssim$10% density variations during the 500 ms of beam modulation are included.) The feature attributed to fast ions decreases rapidly with increasing density (Fig. 5.5(a)). The feature attributed to halo neutrals decreases less rapidly with increasing density than the fast-ion feature but also decreases (Fig. 5.5(b)). In contrast, the background increases rapidly with density (Fig. 5.5(c)).

Figure 5.5 compares the observations with analytical and empirical estimates of the expected dependencies. Consider first the analytical estimates. The fast-ion feature S_f should scale approximately as the product of the injected-neutral and fast-ion densities, $S_f \propto n_n n_f$. The density of injected neutrals n_n decreases with increasing n_e because the stopping power of the plasma increases with density. A simple analytical estimate based on the mean-free path is $n_n \propto [1 - \exp(-k/n_e)]$, where k is a constant. The density of fast ions n_f depends on their deposition rate and on their slowing down time. Locally, the deposition rate is proportional to the

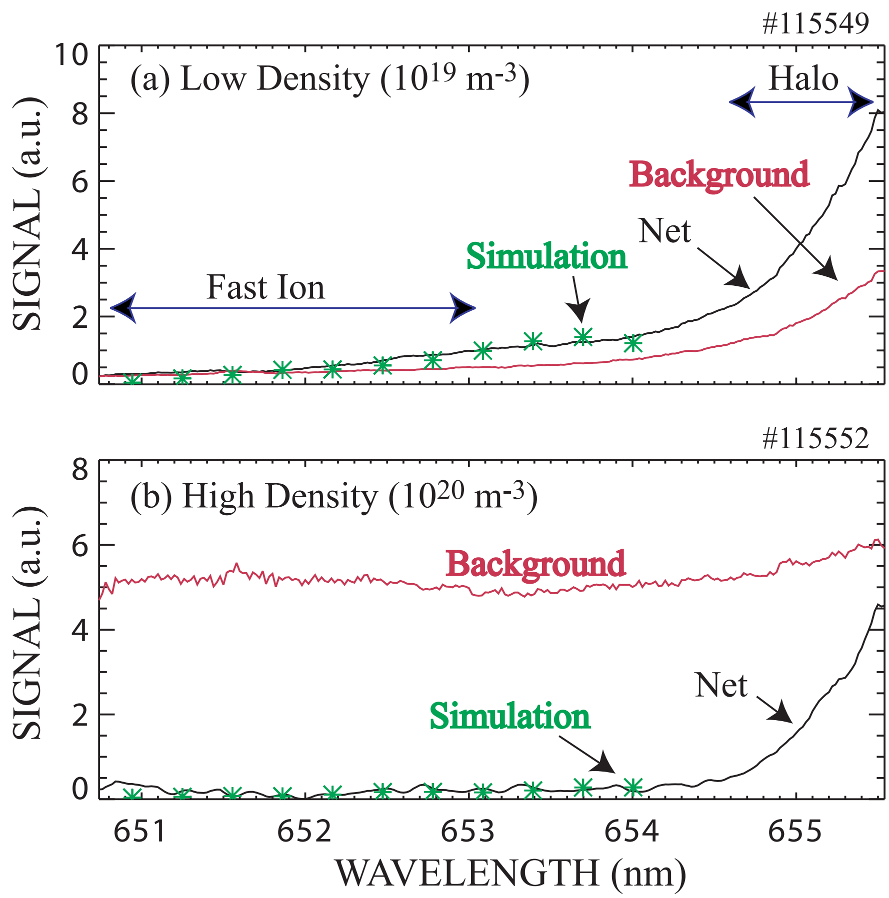

Figure 5.4: Net signal after background subtraction and averaging over the 0.5 s of beam modulation for a (a) $\bar{n}_e = 1.1\times10^{19}\ \mathrm{m}^{-3}$ discharge and a (b) $\bar{n}_e = 10.3\times10^{19}\ \mathrm{m}^{-3}$ discharge similar to the one shown in Fig. 5.1. One of the background slices during a 10-ms beam-off period is also shown. The spectra predicted by the simulation code are indicated by the * symbol; the same normalization is used for both cases. The random uncertainty in the simulation due to Monte Carlo statistics is approximately the size of the symbols. The integration windows for the "fast-ion" and "halo" data shown in Fig. 5.5 are also indicated.

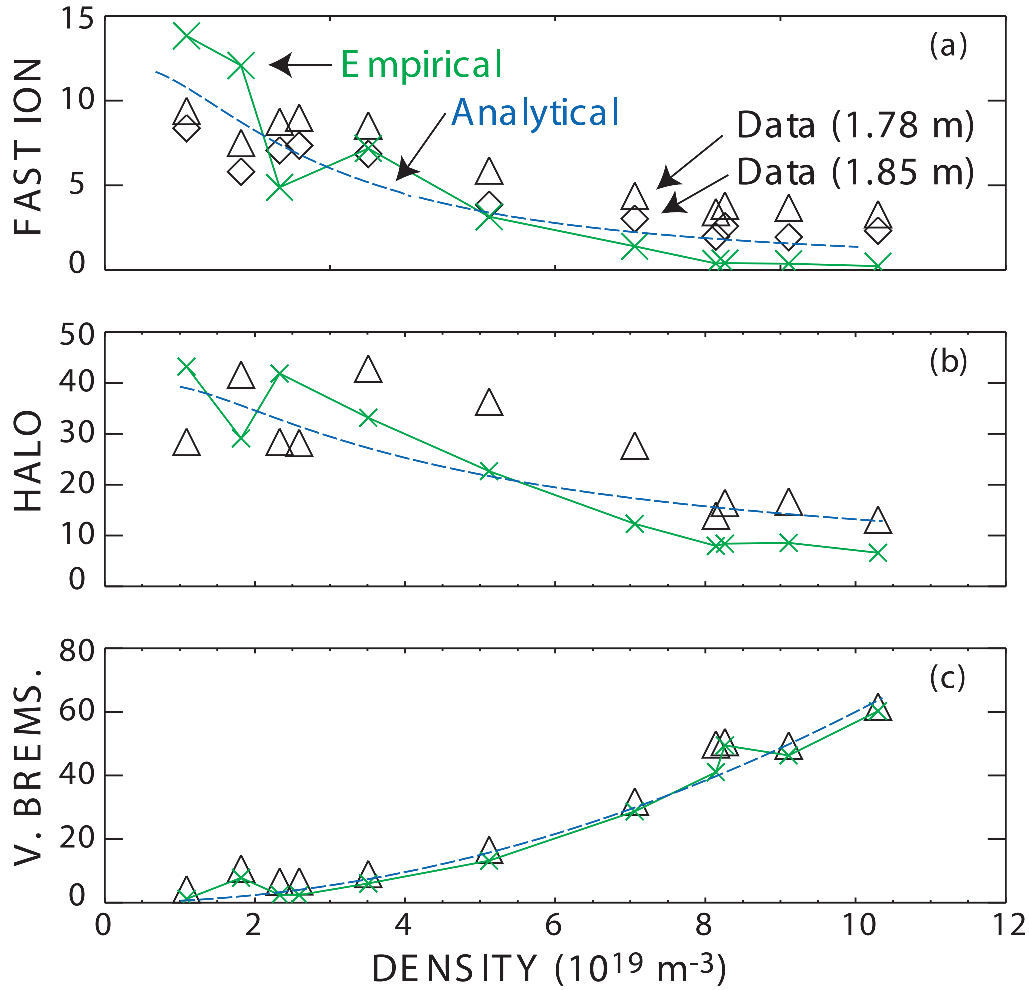

Figure 5.5: Average (a) net signal below 653 nm, (b) net signal above 654.5 nm and (c) background below 653 nm versus $\bar{n}_e$ for a set of eleven discharges with spectra similar to the ones shown in Fig. 5.4. The triangles represent the signals from a fiber that intersects the modulated beam at 1.78 m; the diamonds represent data from 1.85 m. The analytical expressions (dashed lines) and empirical measurements ($\times$) of (a) Eq. 5.1 and $I_{dd}I_{MSE}/\bar{n}_e$, (b) Eq. 5.2 and I_{MSE}, and (c) Eq. 5.3 and I_{VB} are also shown.

product of the local density and the number of injected neutrals that reach that position, $n_e n_n$. The slowing down time is inversely proportional to n_e; also, for the parameters of these discharges, there is an additional modest reduction associated with the dependence of the slowing-down time on the electron temperature, which also generally decreases modestly with increasing density. Thus, the fast-ion density should decrease slightly faster than n_n. Putting these factors together, the expected n_e dependence of the fast-ion feature is roughly

$$S_f \propto n_n n_f \propto [1 - \exp(-k/n_e)]^2. \tag{5.1}$$

The halo feature S_h should be proportional to the number of injected neutrals that ionize near the viewing volume. (There is an additional dependence on the lifetime of the daughter neutrals.) As a rough estimate, we assume that this is proportional to the local neutral density,

$$S_h \propto |\nabla n_n| \propto n_n \propto [1 - \exp(-k/n_e)]. \tag{5.2}$$

For the background, if it is produced by visible bremsstrahlung, it should scale as

$$S_{VB} \propto n_e^2 Z_{eff} \sqrt{T_e} \simeq n_e^2. \tag{5.3}$$

These estimates are compared with the data in Fig. 5.5. The halo and background features agree well with these simple estimates but the fast-ion feature decreases less rapidly than predicted.

Empirical estimates based on independent measurements are also available. For an estimate of the injected neutral density n_n, the intensity of a channel of the Motional Stark Effect (MSE) diagnostic [20] that views the same spatial region is available. For the fast-ion density n_f, when the neutron rate is dominated by beam-plasma reactions, as it is here, the total number of fast ions in the plasma is approximately $N_f \simeq I_{dd}/(n_d\langle\sigma v\rangle)$, where I_{dd} is the d-d neutron rate, n_d is the deuterium density (assumed proportional to n_e), and $\langle\sigma v\rangle$ is the fusion reactivity. Thus, the fast-ion signal should be approximately proportional to $I_{dd}I_{MSE}/n_e$, where I_{MSE} is the MSE amplitude. The halo feature should be proportional to I_{MSE}. An independent diagnostic measures the visible bremsstrahlung emission I_{VB} along a chord that passes through the center of the plasma. These three empirical estimates are also compared with the data in Fig. 5.5. The visible bremsstrahlung measurement is in excellent agreement with the measured background, confirming its identification as bremsstrahlung. The halo feature is in fair agreement with the MSE measurement but, in light of the rather crude model, the agreement is satisfactory. The fast-ion feature does decay with density but the reduction is smaller than expected.

Reexamination of Fig. 5.4 reveals the cause of the discrepancy. The high density data decay less rapidly than expected because the signal is contaminated by the background. In contrast to the low density data (Fig. 5.4(a)), the high density spectrum is essentially flat between 650-654 nm. Evidently, the visible bremsstrahlung is slightly higher when the viewed beam is on than when the distant source is on, so the background subtraction is imperfect, allowing a small fraction of the background to pollute the spectrum. For low densities, the net signal is larger than the background and the pollution is negligible. For high densities, the background is > 10 times larger than the net signal, so small errors are significant. For these discharges and with this instrumentation, a true fast-ion signal is detectable for densities $\lesssim 7 \times 10^{19}\,\mathrm{m}^{-3}$.

To summarize this section, the spectral, temporal, and density dependence of the signals confirms that light from fast ions has been detected in DIII-D .

5.2 Absolute comparison

The simulation output is the number of photons detected by the collection lens, while the measurement is the number of digitizer counts from the CCD camera. To do absolute comparison between the simulation and the measurement, an intensity calibration is performed to convert photons on the collection lens to digitizer counts from the CCD camera for each channel.

Figure 5.6 shows the comparison for a quiet, low beam power (2.4 MW), moderately low density (1.8×10^{13} cm^{-3}), L-mode plasma. The fast-ion distribution from [12] is input to the FIDA simulation code. The central range of the spectrum ($E < 20$ keV) is not simulated for two reasons. First, the measured spectrum over that range is contaminated by halo emissions, edge neutral emissions and beam neutral emissions. Second, it is very inefficient to launch low energy fast ions in the simulation code. They have large populations compared to high energy fast ions. Moreover, they move slowly, which means more time steps for them when solving the collisional-radiative equations.

For the channel with a major radius of 180 cm, the simulated spectrum is scaled by 0.75 to get the agreement, and for the channel at 195 cm, there is no scaling, which is believed to be fortuitous. Comparisons for other shots also reveal that the

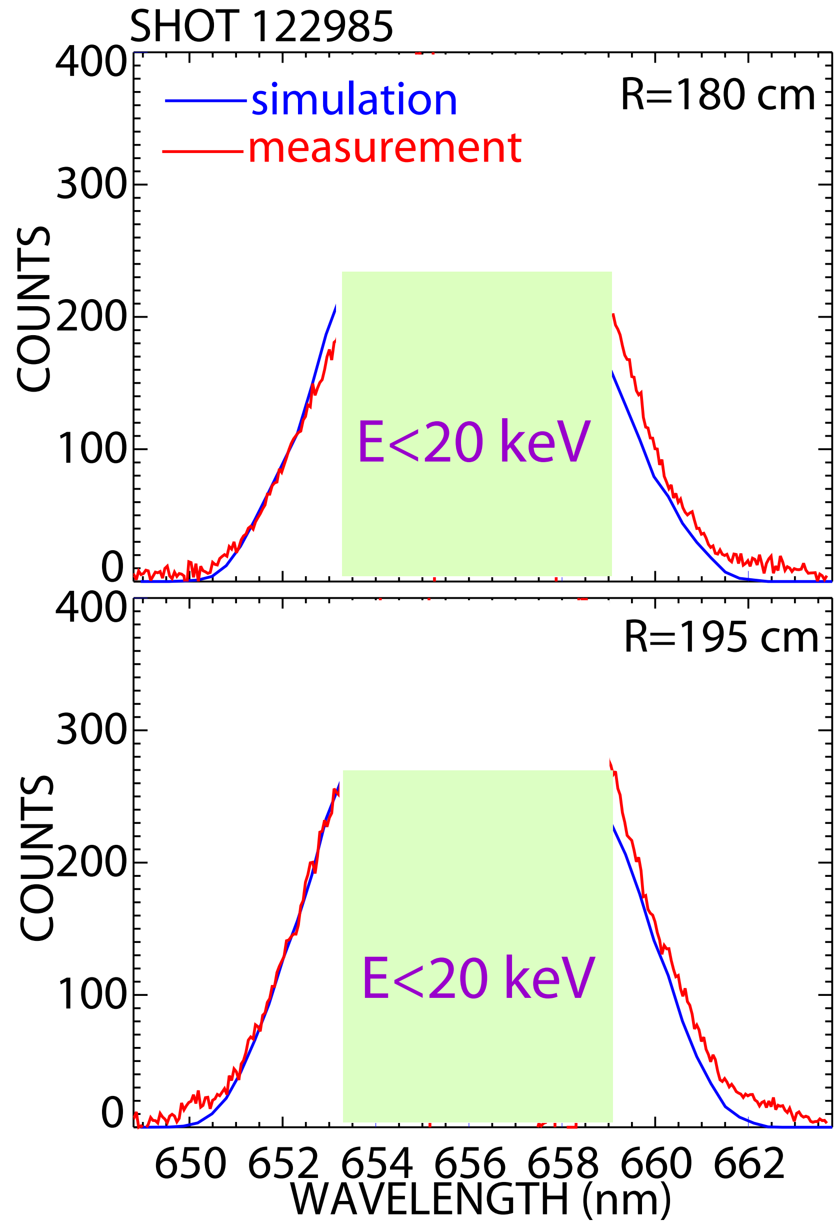

Figure 5.6: Comparison of the measured spectra and simulated spectra. There are no detectable instabilities at the time (1380 ms) of comparison (P_B = 2.4 MW, $B_T = 2.0$ T, $I_P = 1.0$ MA, and single-null configuration). Error bars associated with random errors are less than the size of symbols (not shown).

magnitudes are generally within $20 - 30\%$, which is reasonable provided uncertainties in background subtraction, intensity calibration, and uncertainties in the simulated spectra associated with uncertainties in the plasma parameters and the calculated distribution function. The results of an extensive study of sensitivity of the FIDA simulation code (including TRANSP) on various plasma profiles are presented in §4.3. Among the plasma parameters, electron density has the greatest effect on the FIDA spectrum. Estimates based on this study suggest that the uncertainty in the simulated intensity in Fig. 5.6 is $\sim 20\%$.

For both chords, the spectral shape is in excellent agreement with theory. The simulated spectral shape depends on the fast-ion velocity distribution model and atomic rates. The shape agreements confirm that TRANSP models the fast-ion velocity distribution correctly and validate the atomic cross sections in the simulation code. Some minor discrepancies are readily explained. On the two ends, the small bumps are from imperfect removal of impurity lines. In the left range of the red side, there are huge carbon lines and they usually are removed by beam-on and off background subtraction. When the carbon emission changes slightly between beam-on and beam-off, the background subtraction results in an error. As shown in §4.3, although simulated spectral magnitude is very sensitive on plasma profile uncertainties, the simulated spectral shape is less affected by plasma profile uncertainties. This is one of the reasons that there is better agreement on spectral shape than spectral magnitude.

The spectral shape is determined by the fast-ion velocity distribution. One interesting question is: Does the fast-ion velocity distribution ever change? In other words, does the spectral shape ever change? Figure 5.7 shows the spectral shape of a vertical chord at 195 cm for different plasmas. For this study, the cleanest portion of the spectrum with minimum contamination by impurity lines is chosen. The dashed blue line is the typical shape, which is the average of eight spectra with left beams in quiet plasmas. The green line is also from a quiet discharge, however the electron temperature is only 1.1 keV, which is very low for DIII-D discharges. In this case, the low energy signal agrees with the typical shape and the high energy signal is weaker. This is because there is less pitch angle scattering due to low electron temperature and therefore less fast ions with high vertical energies. The red line is a case with ICH for conditions similar to those documented in Ref.[22]. In this case with 4^{th} harmonic heating, the high energy signal is elevated compared to the typical shape, and the higher the energy, the larger the discrepancy [27]. This is because the fast ions are accelerated by a finite Larmor radius effect and the higher the energy, the stronger the acceleration. The line in violet is a case with Alfvén activities. This case shows the strongest distortion of the spectral shape. The low energy signal decreases and the high energy signal increases compared to the typical shape. This is because fast ions are expelled from the core region and those fast ions have higher vertical energy since the electron temperature is higher in the core region. Normally fast-ion transport due to Alfvén activities can be observed by fast-ion spatial profile change [28]. The shape study implies another way to see evidence of fast-ion redistribution through spectral shape change.

To study parametric dependences and correlations of the FIDA signal, a database with around 700 entries of plasmas with steady conditions for over 200 ms is built from the 2005 campaign. Each entry corresponds to a discharge and an averaging time window which is typically 200 ms. For each entry, there is a substantial amount

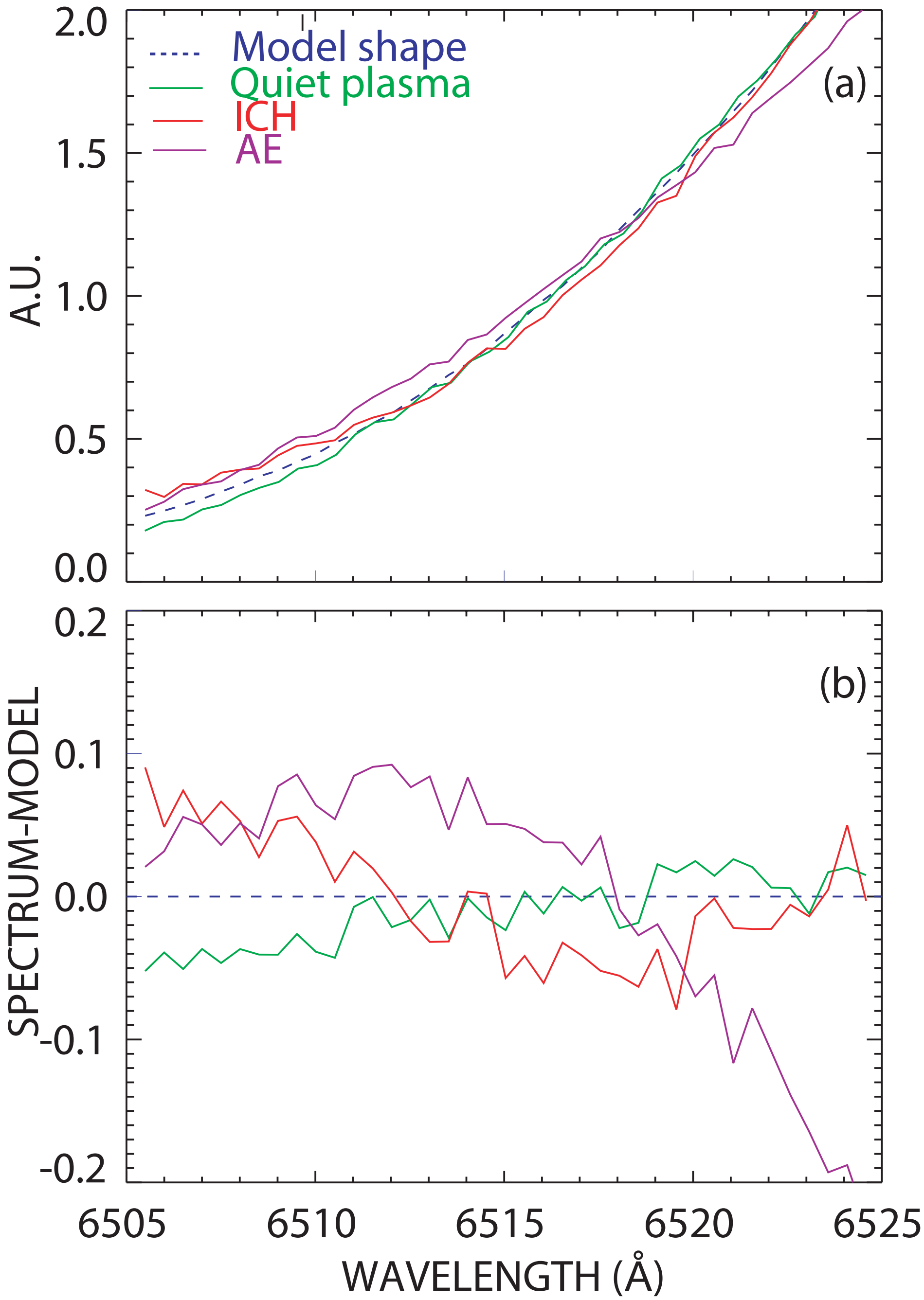

Figure 5.7: (a) Comparison of spectral shape in different plasma conditions. The quiet plasma case is from discharge 122073 at 2000 ms, the ICH case is from discharge 123117 at 2450 ms, and the AE case is from discharge 122527 at 2405 ms. The typical ("model") shape is the average of eight spectra with left beams in quiet plasmas. (b) the differences between the spectral shape of the three individual cases and the model shape.

of information saved. A partial list relevant to this thesis includes the following: plasma parameters (electron density, electron temperature), beam parameters (total power, left beam fraction, beam modulation pattern), ion cyclotron heating (ICH) power, instability flag (MHD, TAE), neutron rate, NPA signal, and FIDA signal.

Spectral shape variation is also studied via the database. For each entry in the database, the spectral shape is compared to the model shape and the reduced chi square is archived. The average of the reduced chi squares for quiet discharges is 0.33. Apparently we overestimated the experimental error associated with photon statistics and readout noise [25], resulting in reduced chi squares much less than 1. Nonetheless, this comparison does show that the average reduced chi squares for discharges with ICH or strong AE activity is considerably larger: 0.44 and 0.50, respectively. Thus, it is evident that ICH and AE activity can alter the spectral shape.

The energy resolution of the FIDA diagnostic is primarily determined by line broadening associated with the motional Stark effect and the slit width of the spectrometer. The Zeeman effect is one order of magnitude smaller than the motional Stark effect for fast ions and can be neglected. The motional Stark effect is proportional to $\mathbf{v} \times \mathbf{B}$, where $\mathbf{v}$ is the velocity of reneutrals and $\mathbf{B}$ is the magnetic field. In DIII-D , the degradation in energy resolution caused by the motional Stark effect is about 6 keV. The entrance slit of the spectrometer is opened up to 500 μm to get more signal, which translates into a spectral resolution of ~ 0.7 nm and an energy resolution of ~ 8 keV. The overall energy resolution is estimated to be ~ 10 keV. This estimation is confirmed by the experimental data. As shown in Fig. 2.6, fast ions are born with full (80 keV), half (40 keV), and third energy

(27 keV) components. Through Coulomb collisions with ions and electrons, fast ions experience slowing down and pitch angle scattering and form a fast-ion distribution. In Fig. 5.8, “steps” in the fast-ion distribution function from half and third energy components are clearly resolved, which demonstrates that the energy resolution of this diagnostic is indeed ~ 10 keV.

5.3 Parametric dependencies and corroborations

In DIII-D , fast ions are born with an injection energy and pitch that is determined by the neutral beam injectors. In quiet plasmas, they slow down through coulomb collisions with thermal electrons and thermal ions. At the same time, they also experience pitch angle scattering through coulomb collisions with thermal ions. The fast-ion density is proportional to the fast-ion birth density and the slowing down time. The fast-ion birth density depends on the deposition profile (which depends in a complex manner on the density profile) and the number of injected beam ions (which is proportional to the beam power P_{inj}). The slowing down time on electrons is proportional to $T_e^{3/2}/n_e$, but collisions with thermal ions are also important, so the expected dependence is $f(T_e)/n_e$, where $f(T_e)$ is an increasing function of electron temperature. The fast-ion density approximately scales as

$$n_f \propto D(n_e) P_{inj} f(T_e)/n_e, \tag{5.4}$$

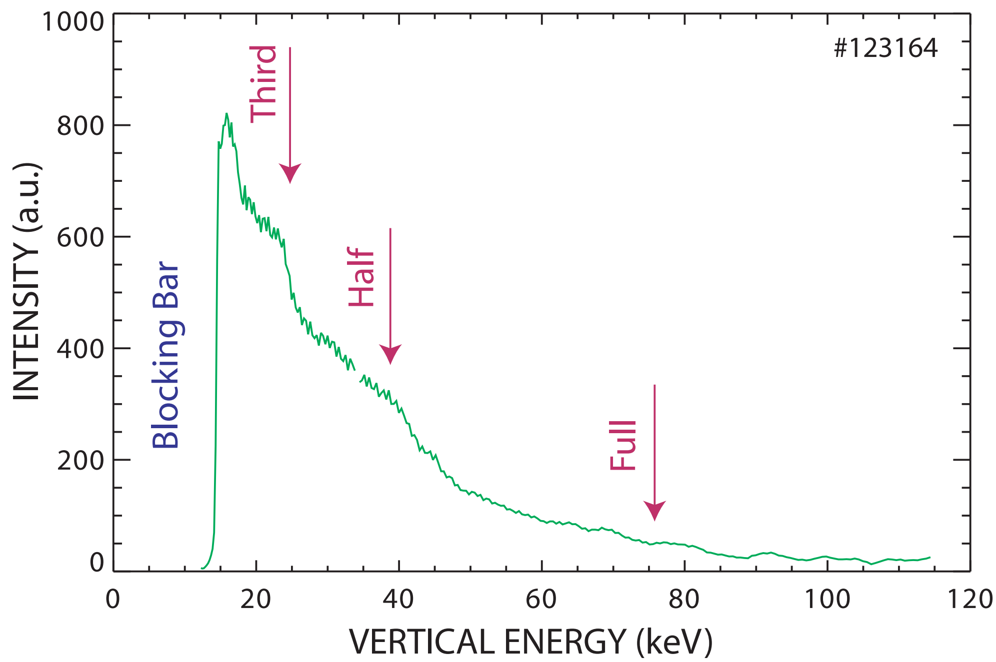

Figure 5.8: “Steps” in the FIDA spectrum. The first one is caused by fast ions from the third energy beam component (27 keV). The second one is caused by fast ions from the half energy beam component (40 keV). In the abscissa, wavelength is converted to the equivalent vertical energy that produces the observed Doppler shift.

where $D(n_e)$ is the beam deposition rate. In this section, we investigate the dependence of the FIDA signal on each of these parameters.

5.3.1 Injection energy

In a neutral-beam heated plasma without RF heating, the highest energy a fast ion can have is approximately the injection energy. Therefore, in the wavelength range above the injection energy, there should be little signal. This makes a very good first test of the FIDA diagnostic. In Fig. 5.9, the line in red is the FIDA spectrum for a discharge with an injection energy of 79 keV. On the two wings beyond the injection energy, the FIDA signal is virtually zero as expected. Starting from the injection energy, the FIDA signal builds up gradually. This is because the FIDA vertical chord measures the vertical energy and the neutral beam injection angle includes a toroidal component. By the time fast ions are scattered to have a large pitch angle, most of them have slowed down considerably. To further check the injection energy dependence, a discharge with a different injection energy is compared. The line in blue is a discharge with an injection energy of 65 keV. It resembles the red line, except that the transition point moves from 79 keV to 65 keV as expected.

5.3.2 Injection angle

In DIII-D , neutral beams can be injected at two different angles. Right beams are more perpendicular and therefore, they introduce fast ions with higher perpendicular energy. Since the FIDA vertical channels measure the vertical energy, over the high energy range, the FIDA signal should be stronger because there is less pitch angle scattering required. In Fig.5.10, the discharge has left beams only in the

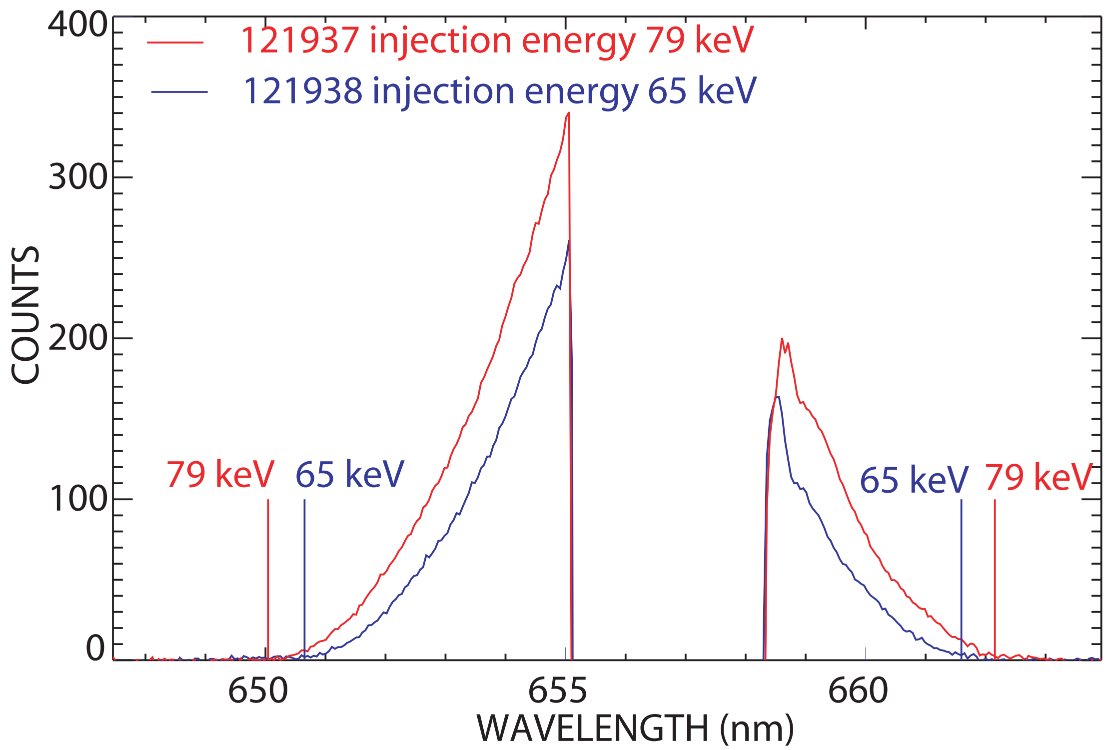

Figure 5.9: Spectra with different injection energies. The middle portion of the spectrum is blocked to avoid saturation due to bright interferences. The wavelengths corresponding to injection energies are labeled on both sides.

early time and later it switches to right beams. Over the two phases, all the fast-ion relevant parameters are kept similar. In the high energy range, the FIDA signal is substantially elevated during right beam injection, as expected.

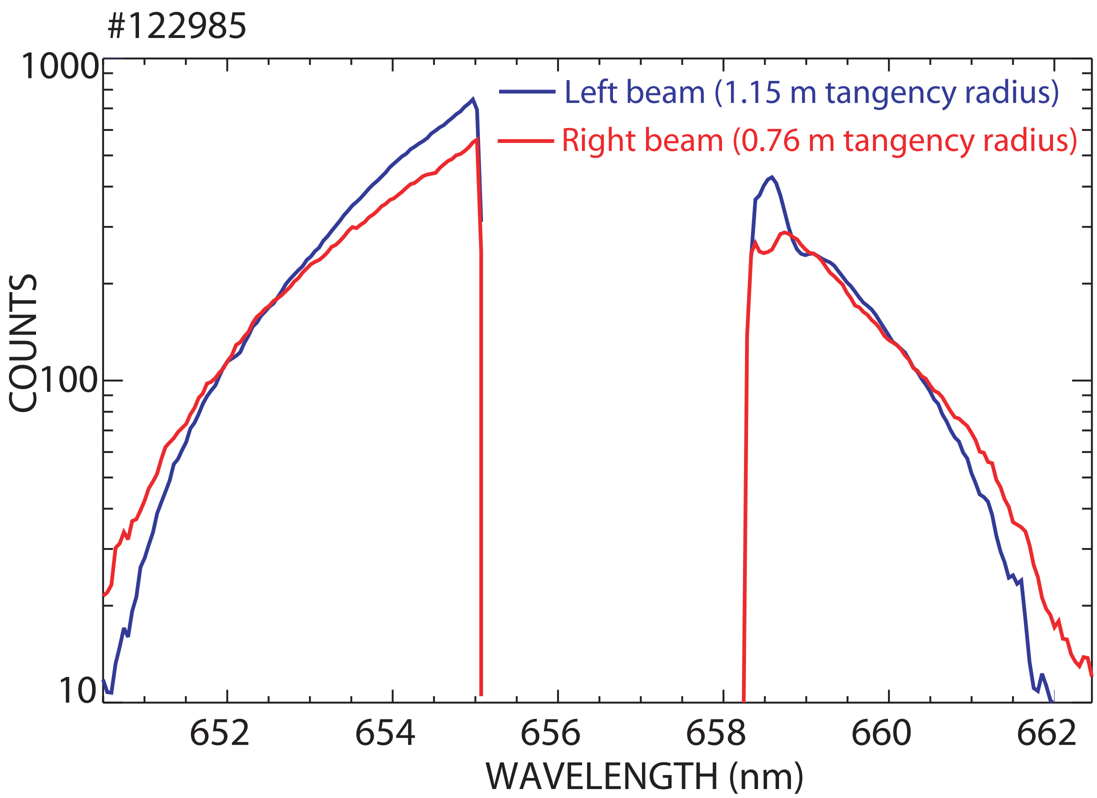

Figure 5.10: Spectra with different injection angles. For the more perpendicular right beam cases, the 330 left beam is modulated in order to take the FIDA measurements with a left beam fraction of 0.2.

5.3.3 Viewing angle

In order to measure the full FIDA spectrum, a perpendicular view is required to minimize the Doppler shift of neutral beam emission. For a non-perpendicular view, one half of the FIDA spectrum is clean with the other half contaminated by beam emission. It is interesting to compare which view has the stronger signal. In the current FIDA system, there is a radial chord viewing at the same major radius as one of the vertical views. Since the red shift side of the radial view spectrum is contaminated, only the blue shift side is compared (Fig.5.11). The spectral shape comparison shows that the radial view detects relatively stronger signal over the high energy range. To explain the difference, a set of angles relevant to the views and fast ions are calculated. The initial fast-ion pitch angle at the chord location is 50.4°, the pitch angle of the radial view is 82.4°, and the pitch angle of the vertical view is 91.1°. For a fast ion to contribute to the high energy range in the spectrum, it needs to be scattered to be around the pitch angle of the viewing chord and at the same time, slowing down should be minimized. Therefore, when the pitch angle of the view is closer to the initial fast-ion pitch angle, fast ions are more likely to be scattered without being significantly slowed down. In the above comparison, the radial view is closer to the initial fast-ion pitch angle resulting in stronger signal over the high energy range. The numbers of the angles show that the present views are far from optimized. To maximize the signal in future implementations, views should be chosen to be as close to the initial fast-ion pitch angle as possible. This usually results in beam emission contamination on the blue side, which is more favorable for the FIDA diagnostic. However, when there are both co and counter neutral beams, views on the counter neutral beam can be optimized to measure circulating fast ions produced by co beam injection.

5.3.4 Injection power

Equation 5.4 shows that, provided that the electron density and electron temperature are fixed, the fast-ion density is proportional to beam power. On the other hand, provided that the neutral density at the chord location is fixed and there is minimal velocity distribution change, the fast-ion density is also proportional to the FIDA signal. Therefore, a linear relationship between the FIDA signal and the beam power is expected when the relevant parameters are similar. This correlation is studied in the database (§5.2) (Fig. 5.12). In this study, electron density is held to be between $4.1 \times 10^{13}\ cm^{-3}$ and $5.0 \times 10^{13}\ cm^{-3}$. The density profiles are very similar, and therefore, the deposition profiles should have minimal differences. Electron temperature on the magnetic axis is held to be between 2.9 keV and 3.5 keV. The relative broad ranges are necessary to get more data points from the database. The correlation coefficient is 0.89. The scatter is likely caused by the finite ranges in electron temperatures and electron density and uncertainties in the beam neutral calculation.

5.3.5 Electron temperature and corroborations

As shown in Eq. 5.4, the fast-ion slowing down time is an increasing function of electron temperature. As a result, the fast-ion density is an increasing function of electron temperature. Moreover, the relative importance of pitch angle scattering increases with electron temperature and consequently the number of fast ions with higher perpendicular energy increases. To study the FIDA electron temperature

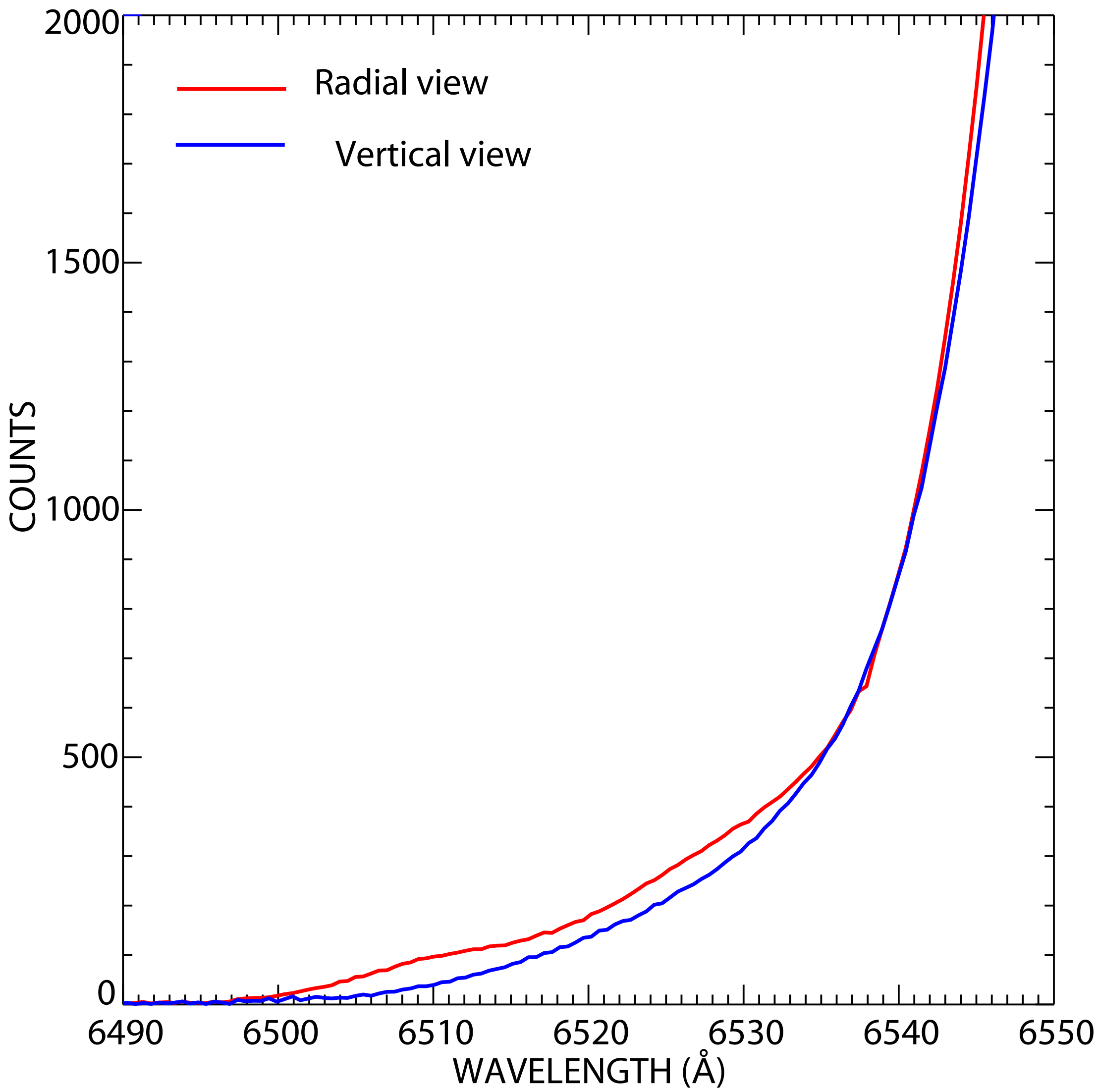

Figure 5.11: View comparison. The radial view is from discharge 122062 at 1670 ms and the vertical view is from discharge 122050 at 1670 ms. Both views are looking at 179 cm major radius. The two discharges have very similar plasma parameters.

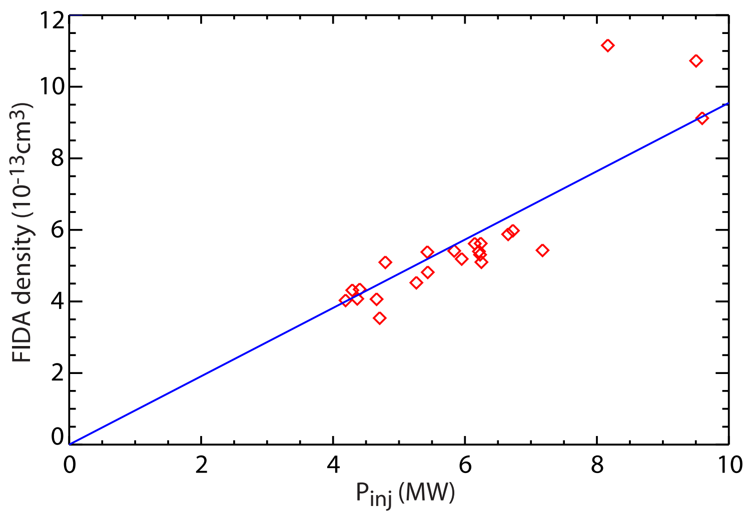

Figure 5.12: Beam power dependence of the FIDA signal. The FIDA signal is averaged over E_λ between 50 keV and 60 keV.

dependence, electron cyclotron heating is modulated to vary the electron temperature. Figure 5.13 confirms that the FIDA signal goes up and down with electron temperature. However, it is not as sensitive as the NPA. The fundamental reason is that the NPA only measures a point in velocity space, while FIDA measures a collection of fast ions in velocity space (§2.2), so pitch angle scattering has a much bigger effect on the NPA. The neutron diagnostic is also a velocity space integrated diagnostic, and not surprisingly, like FIDA, it changes with electron temperature in a more gradual way.

The electron temperature dependence is also studied in the database. To single out the electron temperature effect, all the other relevant parameters are kept similar including electron density, beam power, and left beam fraction. The vertical axis is chosen to be FIDA density to get rid of the neutral density factor on FIDA. Figure 5.14 shows that the FIDA signal increases with electron temperature in the database. The scattered points are caused by loose constraints on the other parameters due to limited database entries.

5.3.6 Electron density dependence

Electron density affects the FIDA signal in three ways: first, fast-ion density is proportional to the fast-ion birth density, which decreases with electron density; second, fast-ion density is proportional to the slowing down time, which is inversely proportional to electron density; third, the injected neutral density decreases with electron density because of the increased stopping power. Figure 5.15 shows the electron density dependence in a particular discharge. This discharge has different densities at the two times with all the other relevant parameters similar. For both

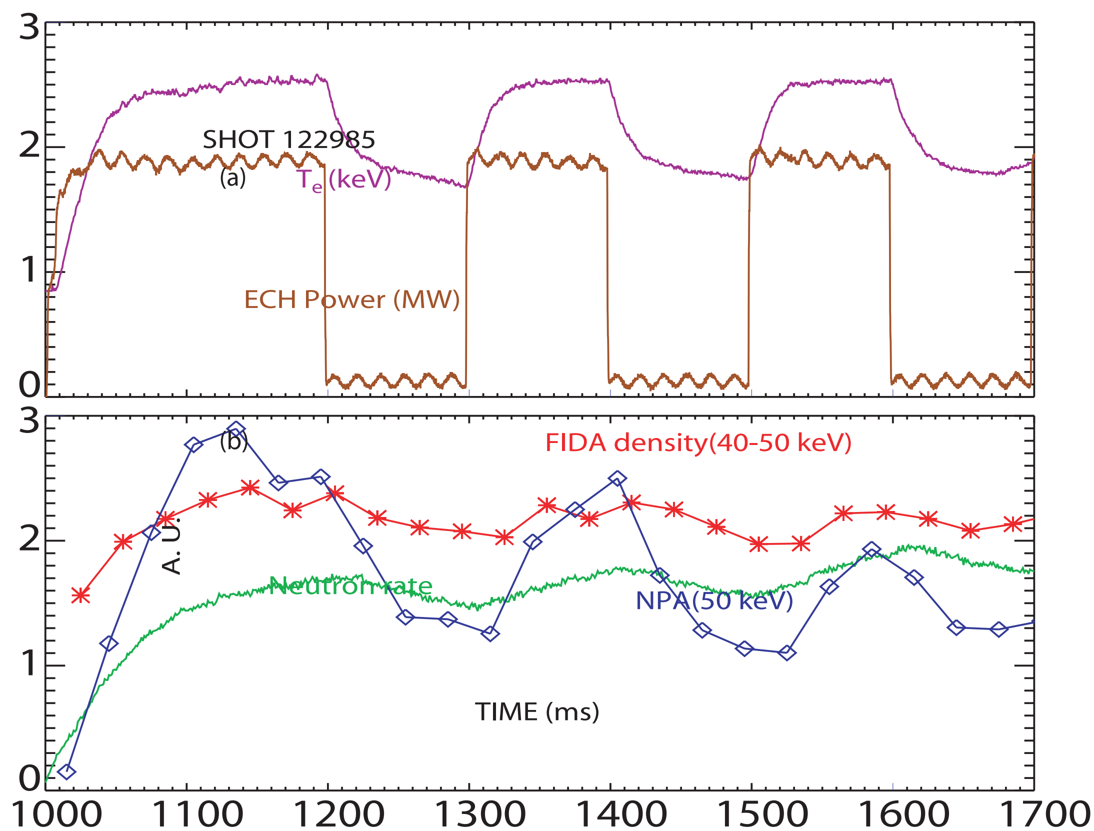

Figure 5.13: (a) Time evolution of ECH power and electron temperature. (b) Time evolution of FIDA density, NPA signal, and neutron rate.

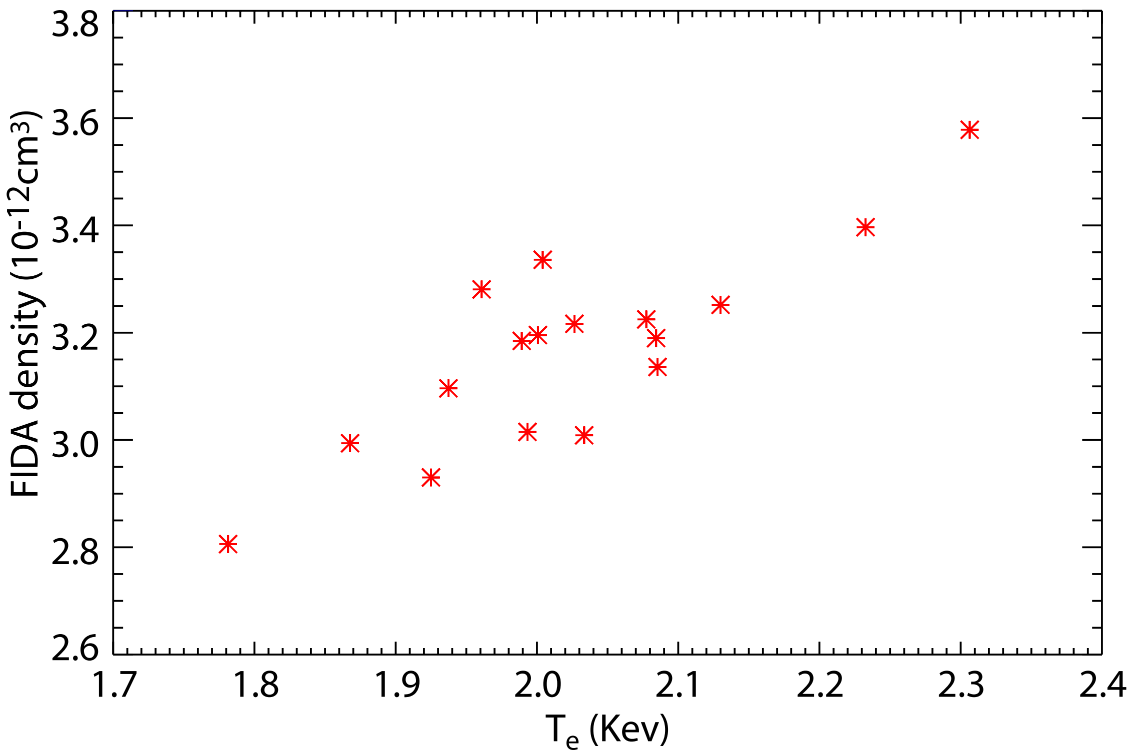

Figure 5.14: Electron temperature dependence of the FIDA density in the database. The FIDA signal is averaged over E_λ between 40 keV and 60 keV. Electron is held to be between $2.5 - 3.5 \times 10^{13}\ cm^{-3}$.

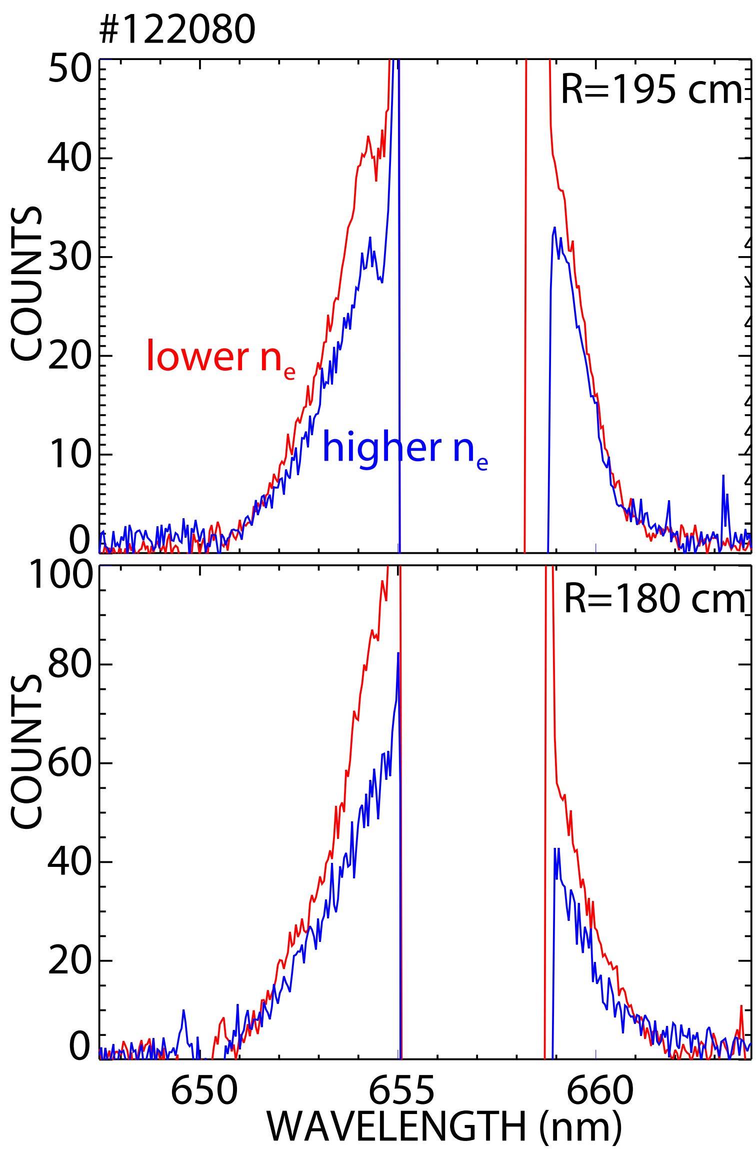

Figure 5.15: Electron density dependence of the FIDA signal. The spectra in red is at 1930 ms with an electron density of $3.8 \times 10^{13}\ cm^{-3}$. The spectra in blue is at 2750 ms with an electron density of $5.0 \times 10^{13}\ cm^{-3}$.

chords, the FIDA signal drops considerably during the high density phase. The chord at 195 cm shows less drop because the electron temperature is 15% higher at the later time, which offsets some of the dip.

To study the electron density dependence quantitatively, a discharge with a period during which the electron density steadily ramps up is selected. The points in red in Fig. 5.16 are the FIDA measurements and, as expected, they decrease with electron density. To calculate the expected dependence, a simple model is built for the FIDA signal. The model is the product of total neutral density, the deposition rate of the full energy component, and the slowing down time. Note that the product of the last two terms is proportional to fast-ion density. Only the deposition rate of the full energy component is adopted because the FIDA measurements are the high energy signal, which exceeds the half and third energy components. All atomic physics is neglected in this model, which is legitimate when the velocity distribution doesn not change and only the signal level is concerned. With one free parameter (constant scaling), the model shows very good agreement with the measurements on both chords.

5.3.7 Neutron corroboration

The neutron diagnostic is another fast-ion diagnostic and the correlation between FIDA and the neutron diagnostic is investigated in the database. As usual, the vertical axis is FIDA density, which is proportional to fast-ion density. In most discharges in this study, beam-thermal reactions dominate the neutron production and therefore, the neutron rate over electron density is proportional to the fast-ion density. As shown in Fig. 5.17, a strong correlation is observed between FIDA and

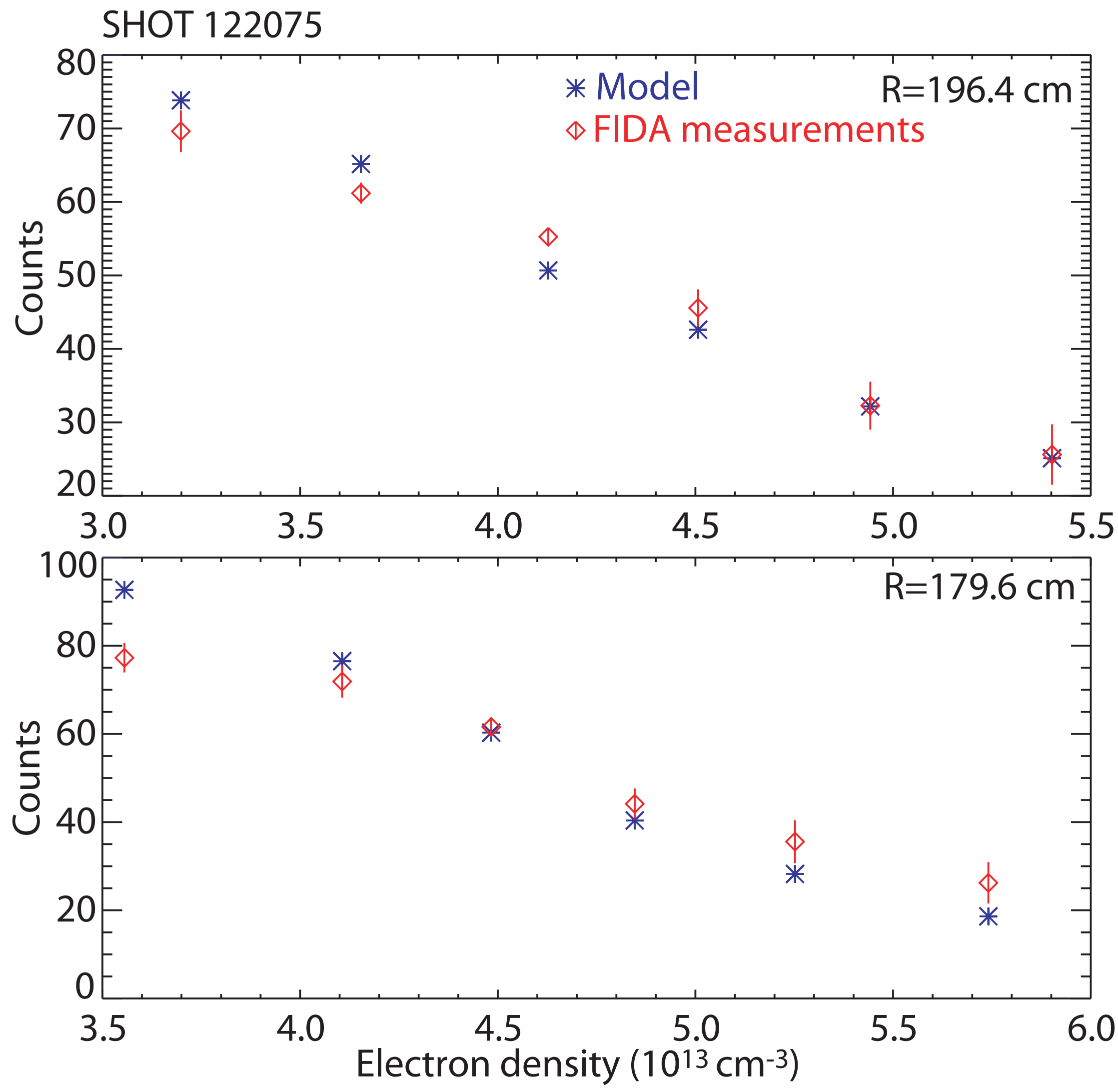

Figure 5.16: Electron density dependence of the FIDA signal and comparison with the simple model described in the text. Each FIDA data point is averaged over E_λ between 25 keV and 60 keV and a 200 ms time window.

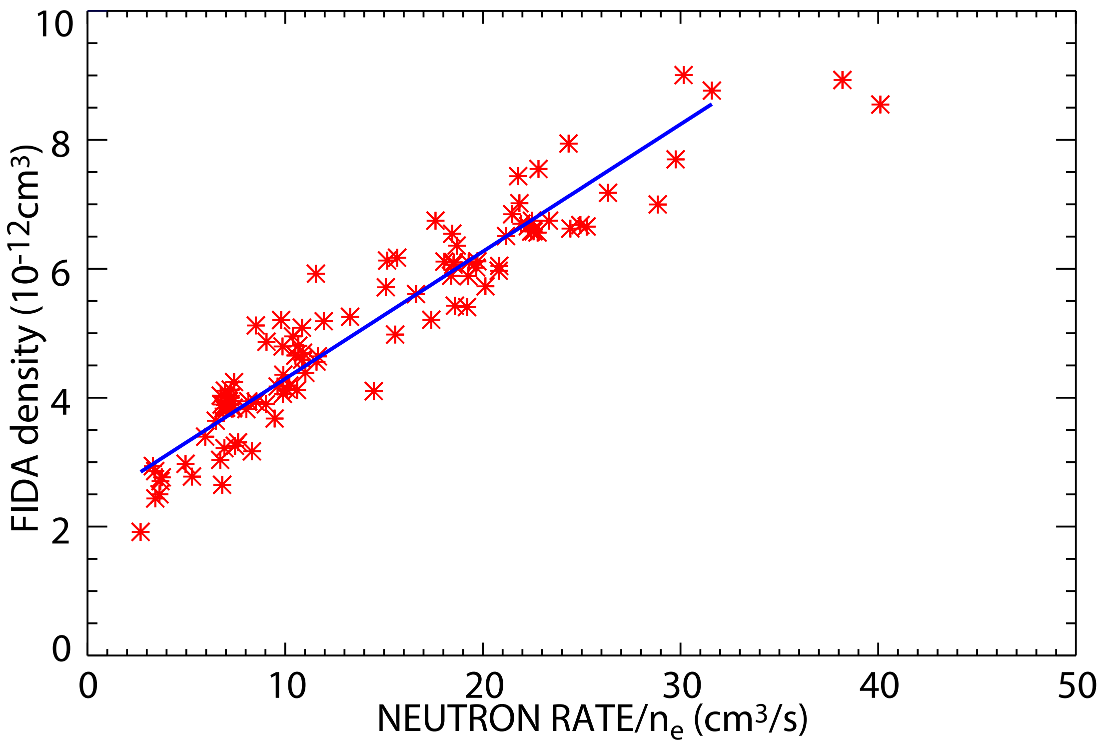

Figure 5.17: Correlation between the FIDA diagnostic and the neutron diagnostic. The FIDA signal is averaged over E_λ between 30 keV and 80 keV from a chord viewing 195 cm major radius.

the neutron diagnostic. The fitted line does not go through the origin because for low values of n_e, beam-beam reactions constitute $\sim 25\%$ of the total neutron rate, so neutron rate/n_e overestimates the fast-ion density.

5.4 Spatial profiles

As shown in Fig. 2.10, there are 9 vertical chords available for the FIDA measurements, which allow us to obtain the fast-ion spatial profiles. However, the chords are different in many aspects. There are two systems, the dedicated system and the Reticon system, which have different components and detectors. Even within a system, the spot sizes, the solid angles subtended by the collection lens and the light paths differ substantially. There are two ways to overcome the chord difference. One is to use the relative FIDA profile, and the other is to take the absolute FIDA profile with all the chord specifics removed.

To generate a FIDA profile, an energy window is chosen first. Then for each chord, the signal is averaged over the selected energy window. A relative FIDA spatial profile is a profile obtained by dividing one raw profile by another raw profile for different plasma parameters. Since the relative profile only provides relative information, it is independent of chord specifics and requires no special processing for individual chords. Figure 5.18 shows a typical relative profile in a quiet plasma. Two time slices are chosen with a substantial density change (Fig. 5.18(a)). In quiet plasmas, the fast-ion density is inversely proportional to the electron density. Therefore, the fast-ion density at the later time is expected to be higher. This is confirmed by the beam pressure profile calculated by TRANSP (Fig. 5.18(b)); the shapes of the predicted beam-ion density profiles are similar. An independent

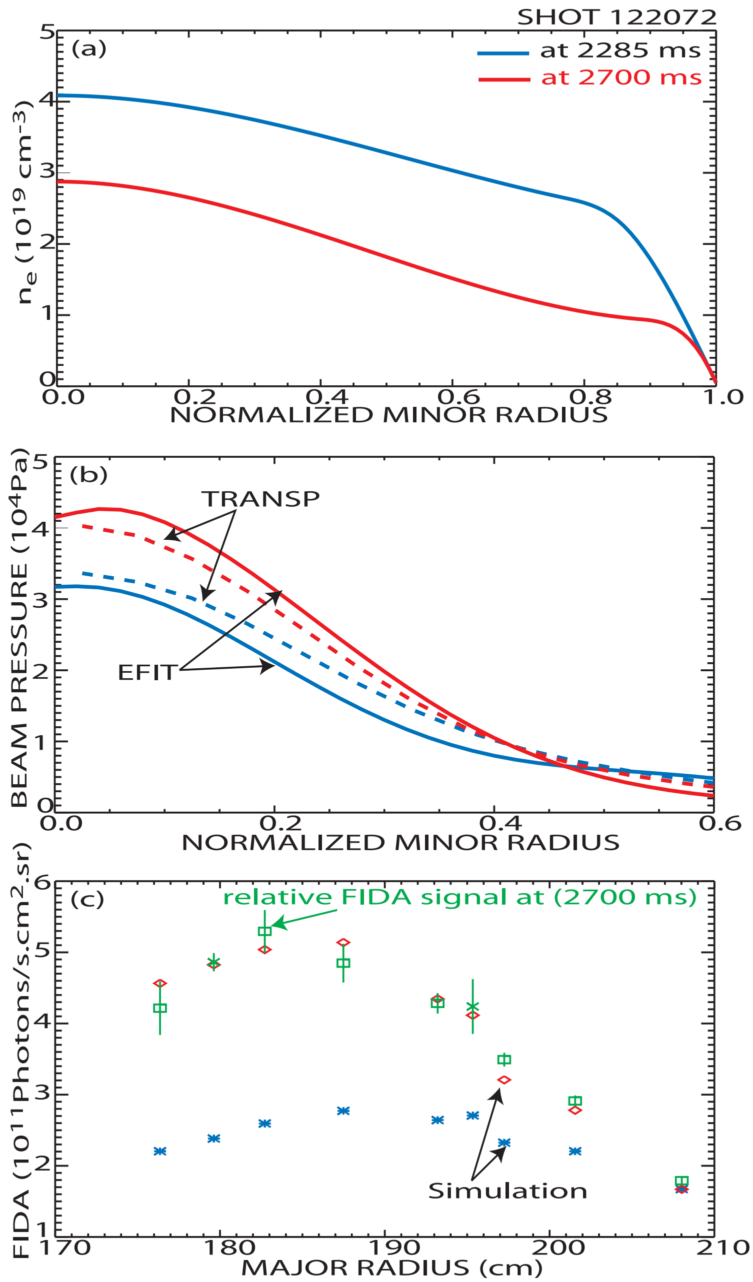

Figure 5.18: (a)Electron density profiles versus normalized minor radius at 2285 ms and 2700 ms. (b) Beam pressure profiles from TRANSP (dashed) and EFIT (solid) versus normalized minor radius at the two times. (c) Simulated profiles and relative FIDA profile. The FIDA signal is averaged over E_λ between 20 keV and 40 keV.

measurement of the beam pressure profile is available from EFIT [13] equilibrium reconstructions that rely on motional Stark effect (MSE) polarimetry,[11] magnetics, and T_e isotherm measurements (§2.2). The thermal pressure profile from kinetic measurements is subtracted from the EFIT pressure profile to obtain the beam-ion pressure. [21] For the conditions of Fig. 5.18, the absolute uncertainty in the fast-ion profiles are $\sim 20\%$ and the relative uncertainties are about $\sim 10\%$. The profiles obtained in this fashion are consistent with the TRANSP predictions within these uncertainties and confirm that the fast-ion behavior is close to classical in this discharge. TRANSP runs with various spatially uniform *ad hoc* beam-ion diffusion coefficients are compared with the EFIT beam pressure profile. Error bars imply that diffusion coefficient must be within 0.1 m^2/s. The FIDA profile is compared with the prediction of the simulation code in Fig. 5.18(c). The FIDA signal is proportional to both the fast-ion density and the neutral density. Since the fast-ion density peaks on axis, but the neutral density is largest at the edge, the simulated profiles peak between the magnetic axis and the edge. At the later time with lower electron density, the simulated FIDA profile is significantly elevated. The jump is more pronounced than that for beam pressure. This is due to the increased neutral density resulting from the lower electron density. To obtain the relative FIDA profile, the FIDA measurements at the earlier time are scaled to match the simulated profile at the earlier time and at the later time, the FIDA measurements are scaled by the same factor. Excellent agreement is reached between the measured FIDA relative profile and the simulated profile. The error bars in the figure only address the random errors. In this quiet discharge, the systematic errors should be small. The agreement shows that FIDA relative profiles can provide precise information on how fast-ion profiles evolve.

Figure 5.19 shows the first attempt we made to compare the FIDA relative spatial profile with the simulation. In this discharge, electron density increases significantly from 1.395 s to 1.5 s. As a result, the simulated profile is lowered as expected. However, the measured relative spatial profile does not agree with the simulation in the outer region even after taking into account the error bars. This discrepancy had troubled us for a long time until one day we found that there is a strong Alfvén instability right around 1.5 s, which easily explained the discrepancy. Some fast ions are expelled to the outer region by the Alfvén instability resulting in increased FIDA signals for the outer chords.

The absolute FIDA profile is very challenging. To produce an absolute FIDA profile from the measurements, intensity calibration data for each chord are utilized to convert the number of digitizer counts into numbers of photons. The chord specifics such as solid angles and spot sizes are normalized out. Figure 5.20 shows the comparison between the measured absolute FIDA profile and the simulated absolute FIDA profile in a quiet plasma. The magnitudes are within 30% for all the chords, which is very reasonable provided the uncertainties in data processing, plasma profiles input to the simulation code and intensity calibrations. The simulated profile shape is as expected, peaking at a point somewhere between the magnetic axis and the edge. However, the measured profile shape does not agree with the simulation. The difference between the CCD channels and the Reticon channels suggests that the intensity calibration is problematic. The errors are estimated based on the FIDA data only, without taking into account the uncertainties in intensity calibration. The modest error bars show that future

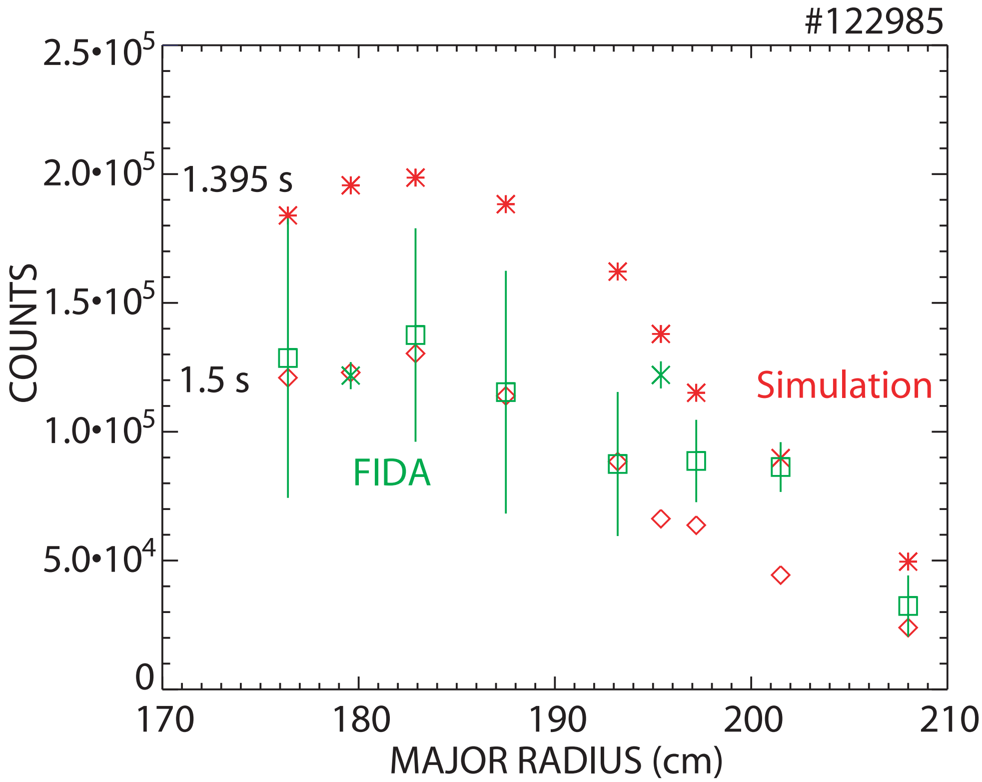

Figure 5.19: Simulated profiles and measured relative profile. The FIDA signals are averaged over E_λ between 30 keV and 60 keV.

prospect for absolute profiles is good with careful intensity calibration.

5.5 Conclusion

The proof-of-principal FIDA data taken by the CER system in 2003 show that D_α light from a fast-ion population produced by deuterium neutral beam injection has been detected in the DIII-D tokamak. The signals have the expected spectral, temporal and density dependences. Visible bremsstrahlung obscures the fast-ion signal for densities $\lesssim 7 \times 10^{19}\ m^{-3}$. It is unlikely that this constitues the ultimate density limit for this diagnostic. In the TFTR α CER spectroscopy experiments, high-throughput optics and background corrections enabled successful measurements of fast-ion signals with signal-to-background ratios of $< 1\%$ [43]; in JET, helium signals that were a few percent of the bremsstrahlung level were extracted from the data [49]. Nevertheless, it is clear that this diagnostic concept favors low density: for fast ions produced by neutral-beam injection, the signal-to-background ratio scales roughly as n_e^{-3}.

FIDA measurements in quiet plasmas are compared with simulations that use the fast-ion distribution from TRANSP. The spectral shape is in excellent agreement, indicating that the Coulomb collision model in TRANSP is valid and the atomic cross sections in the FIDA simulation code are accurate. The absolute signal magnitude is within 30%, resulting from a variety of uncertainty sources. The sensitivity study (§4.3) suggests that the uncertainty of electron density profile is the most influential one and could account for a large portion of the discrepancy.

The parametric dependencies of the FIDA diagnostic in quiet plasmas are studied extensively both in individual discharges and in a large database. All of the

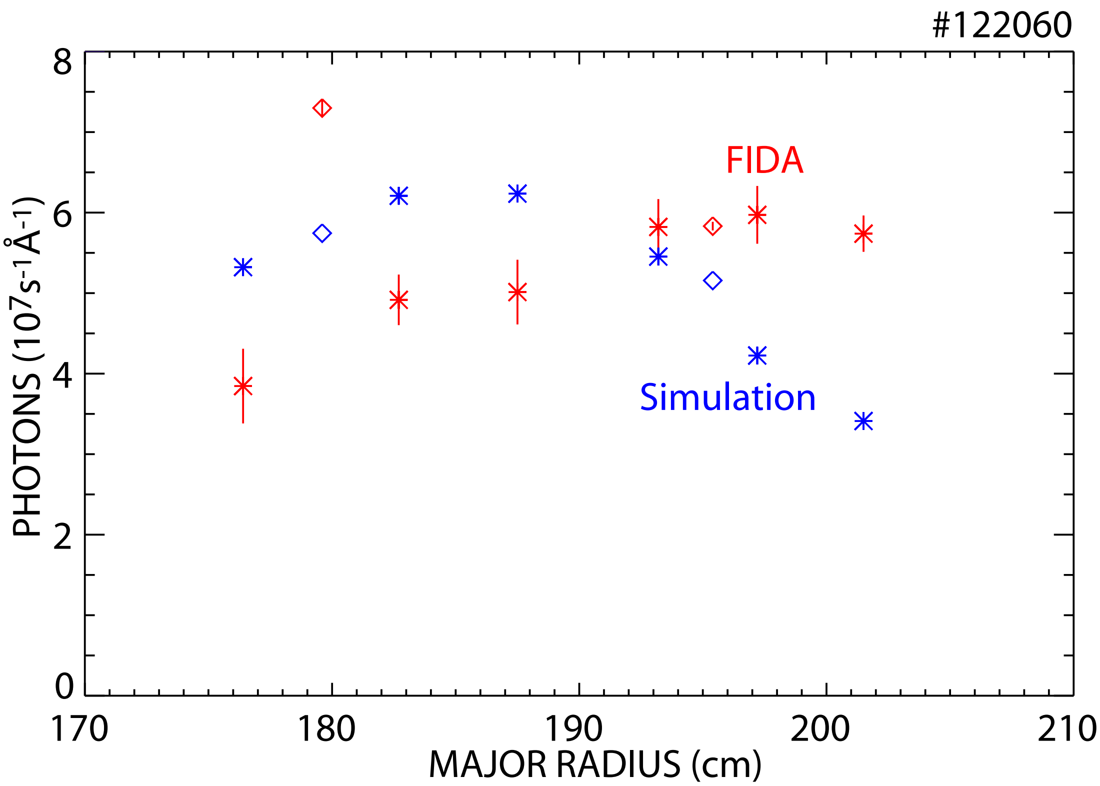

Figure 5.20: Absolute comparison of the measured FIDA profile and the simulated profile. The time of the comparison is at 2100 ms. The FIDA signal is averaged over E_λ between 30 keV to 60 keV. The CCD channels are shown in diamonds.

dependencies are as classically expected, suggesting that the FIDA diagnostic is well understood. The NPA and neutron diagnostics corroborate the FIDA diagnostic.

A set of vertial chords allows us to obtain the FIDA spatial profile. The relative profile is compared with the simulated profile and shows excellent agreement. Error bars imply that fast-ion diffusion coefficient must be within 0.1 m^2/s. However, obtaining the absolute profile is problematic currently, but may be resolved in the future with a careful intensity calibration.

The successful benchmarking of FIDA measurements in these quiet plasma establishes the reliability of this diagnostic technique, allowing its confident application in more complicated situations.

Chapter 6

Measurements of fast-ion acceleration at cyclotron harmonics

6.1 Introduction

Cyclotron damping of fast waves in the ion cyclotron range of frequencies is a standard heating scheme in magnetic fusion devices. Injected beam ions have been accelerated by ion cyclotron heating (ICH) at cyclotron harmonics in many tokamaks [69]-[82]. Most measurements of acceleration by ICH have employed neutral particle analysis [83, 14], although fusion reaction measurements of neutrons and charged fusion products are also common [14, 84]. Differences between the perpendicular and equilibrium stored energy are used to measure the anisotropic fast-ion energy [85]. Measurements of fast ions that escape on loss orbits can also diagnose ion acceleration [86]. In recent years, gamma- ray tomography has emerged as a powerful technique [87, 88]. Collective Thomson scattering has also detected ions accelerated by ion cyclotron heating [89].

Deuterium beam-ion acceleration at the 4th-8th harmonics was previously studied on the DIII-D tokamak using established techniques [21, 76, 22, 79, 90, 91]. Since the vertical chords of the FIDA diagnostics measure the vertical component of the fast-ion velocity, which is one component of the perpendicular velocity, the FIDA diagnostics are well suited to detect fast-ion acceleration by ICH that accelerates fast ions in the perpendicular direction.

6.2 Data

6.2.1 Plasma conditions

The experiments were performed in the DIII-D tokamak (§1.3) (graphite walls, deuterium plasmas) at the end of the 2005 campaign. The conditions are nearly identical to the ones reported in Ref. [22]. Typically, one transmitter couples 0.7-1.0 MW at 60 MHz into L-mode plasmas. Counter-current drive phasing (90° toroidal phasing between straps) is employed, with the peak in the vacuum spectrum at $n_\parallel \simeq 5$. In some discharges, other transmitters couple up to 2 MW of power at 113-117 MHz but these waves have little effect on the fast ions [92] and are not discussed here. At the usual toroidal field of 1.9 T, the 60 MHz waves resonate with the deuterium cyclotron harmonic at several radial locations, with the central resonance corresponding to the fourth harmonic (Fig. 6.1). The beams inject 75-81 keV deuterium beam ions in the direction of the plasma current at tangency radii of 0.76 m (right sources) and 1.15 m (left sources). Most plasmas are upper single null divertor discharges with an elongation of $\kappa = 1.7$. The ∇B drift is usually downward to avoid H-mode transitions. Spectroscopic measurements of the cold H-alpha and D-alpha lines imply that the hydrogen concentration is usually below 1%. The dominant impurity is carbon and charge-exchange recombination [8] measurements indicate typical central ion temperatures of $T_i = 5$ keV, toroidal rotation velocities of 2×10^7 cm/s, and impurity concentrations of $Z_{eff} = 1.5$.

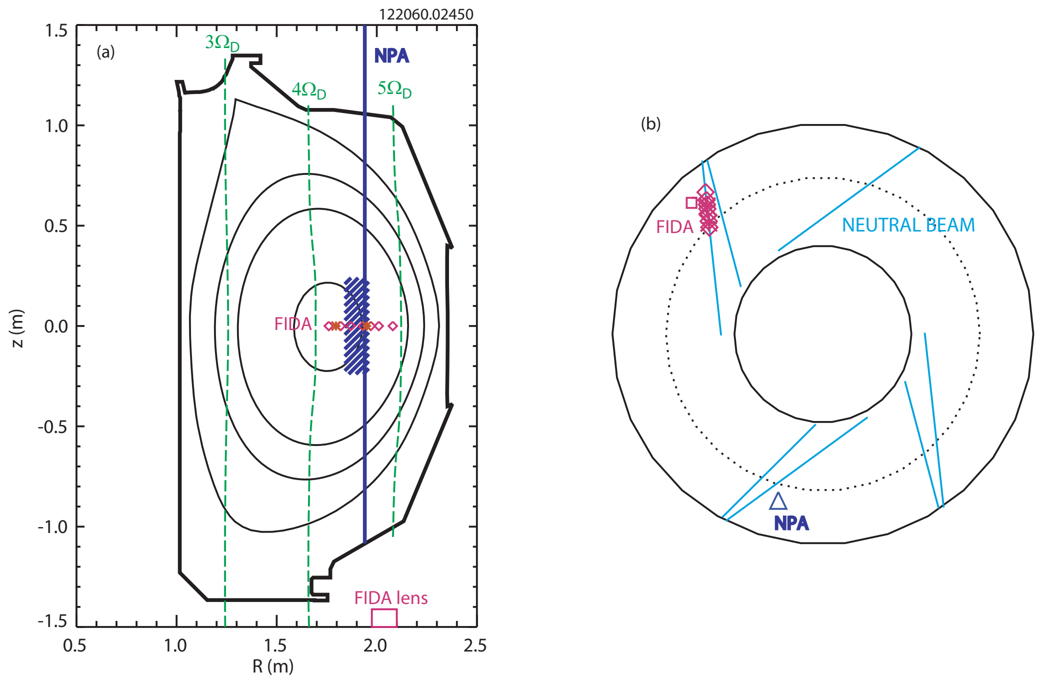

Figure 6.1: (a) Elevation of the DIII-D vacuum vessel, showing the separatrix and the $q = 1, 2$, and 3 surfaces (solid black curves), the locations where ω_{RF} equals the third, fourth, and fifth deuterium cyclotron harmonic (dashed green curves), the neutral-particle analyzer sightline (thick blue line), and the midplane locations of the FIDA Reticon (diamond) and CCD (solid triangle) chords. The hashed region represents the approximate vertical extent of the heating beam that produces the FIDA and NPA signals. The square indicates the approximate location of the FIDA collection optics. (b) Plan view of the vessel, showing the toroidal location of the FIDA and NPA diagnostics and the centerlines of the various Left and Right beams. The dotted line represents the magnetic axis.

6.2.2 FIDA measurements

The temporal evolution of a discharge with central fourth harmonic heating is shown in Fig. 6.2. Neutral-beam injection commences 0.6 s after the current reaches its flat top value of 1.0 MA. To accommodate the diagnostics, five modulated sources inject into the plasma but the average total power is 3.6 MW. The total power only varies for 10 ms, which is much less than the beam ion slowing down time of $\tau_s \simeq 100$ms. The 60 MHz system couples ~ 1 MW of power between 2.2 and 3.7 s. At 3.3 s, the neutral beam injection switches from the more tangential Left sources to the more perpendicular Right sources. With the application of RF power, the neutron rate increases on a τ_s timescale. The central electron temperature increases and the sawtooth period increases during ICH but transient periods of sawtooth stabilization ("monster" sawteeth [93]) are not observed. Analysis of magnetics and far-infrared scattering [94] signals shows that Alfvén modes are weak or absent in this discharge.

During the ICH, the neutron rate increases more than classically predicted (Fig. 6.2(c)), indicating acceleration of energetic ions by the 60 MHz waves. The central FIDA data (Fig. 6.2(d)) show that the acceleration is greatest for energies near or above the injection energy. Evidently, the slope of the energy distribution is distorted by the harmonic heating.

Comparison of the FIDA spectra before and during ICH (Fig. 6.3) clearly shows that fast ions are accelerated above the injection energy. Prior to ICH, the spectra are in good agreement in magnitude and shape with the spectra predicted by a FIDA simulation code (Chapter 4) that uses the distribution function from collisional processes (as predicted by TRANSP) and includes all relevant atomic physics effects. In the absence of RF acceleration, the predicted spectra are only

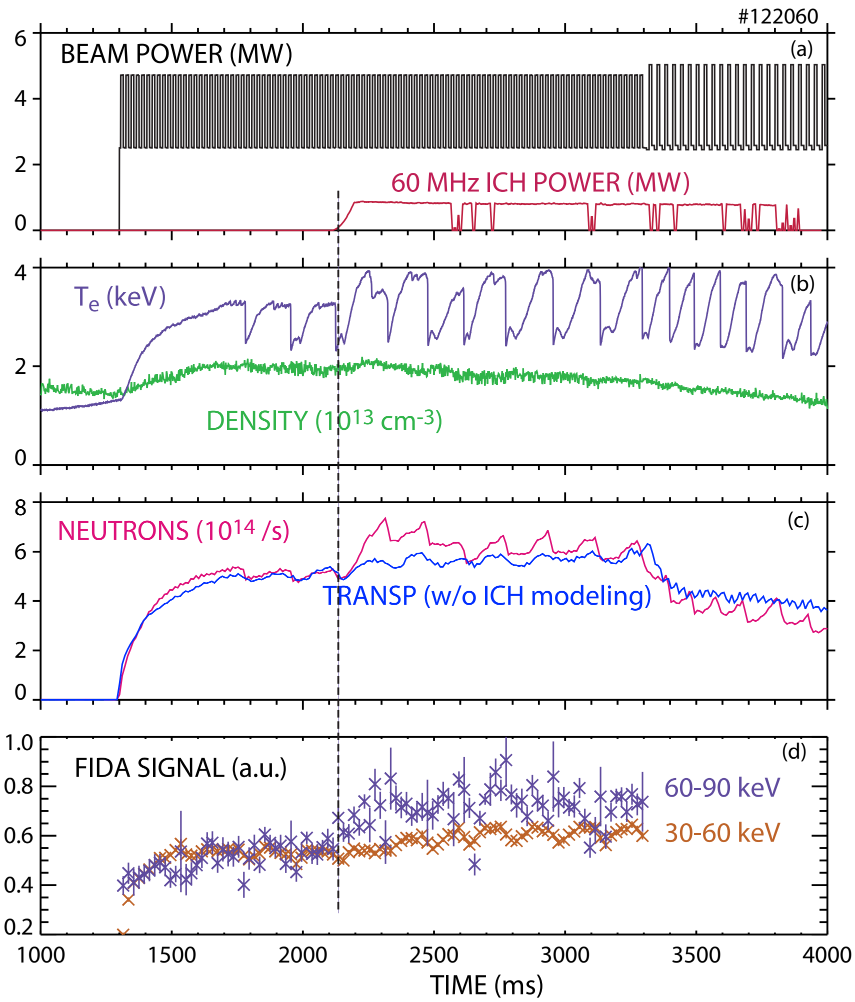

Figure 6.2: Time evolution of (a) the injected neutral beam and coupled ICH power, (b) the central electron temperature and the line-average electron density, (c) the measured neutron rate and the classically expected rate in the absence of ion cyclotron acceleration, and (d) the FIDA signal in two spectral bands. The more tangential Left beams are injected from 1300-3300 ms, while more perpendicular Right beams are injected after 3300 ms. For the FIDA data, the “30-60 keV” signal represents E_λ between 30-60 keV (wavelengths between 650.8-652.4 and 659.8-661.3 nm) and the “60-90 keV” signal integrates wavelengths between 649.6-650.8 and 661.3-662.6 nm. The radial position of the FIDA channel is centered at $R = 195.4$ cm. $B_T = 1.92$ T; $I_p = 1.0$ MA.

expected to change slightly in the latter phase of the discharge but the observed increase is much larger, owing to the ion cyclotron acceleration. The distortion in the measured slope begins at a wavelength that corresponds to $E_\lambda \simeq 50$ keV. Because 4th harmonic heating is a finite Larmor radius effect that depends upon the value of $k_\perp \rho_f$, this is consistent with the theoretical expectation that higher energy ions should be most strongly affected. (Here $k_\perp$ is the perpendicular wavenumber and ρ_f is the fast-ion gyroradius.) As expected, the acceleration is larger near the resonance layer (Fig. 6.3(a)) than farther away (Fig. 6.3(b)).

Strong acceleration is also sometimes observed at lower toroidal field when the 5th harmonic layer is near the magnetic axis. Figure 6.4 shows the time evolution of a low-power discharge with particularly large acceleration. The average beam power is only 1.2 MW and the coupled ICH power is 0.8 MW in this case (Fig. 6.4(a)). The electron density and temperature are both relatively low (Fig. 6.4(b)). With the onset of ICH, the neutron rate nearly doubles (Fig. 6.4(c)), presumably because the power per particle is large. Because the number of fast ions is relatively low, the NPA and FIDA signals have rather poor statistics (Fig. 6.4(d) and (e)) but a significant increase is observed by both diagnostics during ICH. The angle of beam injection switches from exclusively Left to primarily Right sources midway through the ICH pulse (at 2.75 s). This causes a large jump in NPA signal that is classically expected and that persists after the RF. The vertically-viewing NPA only detects perpendicular ions, so ions injected by the Right source need only pitch-angle scatter $\sim 23°$ to be detected, while ions from the Left source must scatter $\sim 36°$. In contrast, because they arise from effective averages over pitch angle in velocity space, the FIDA and neutron signals hardly change when the injection angle

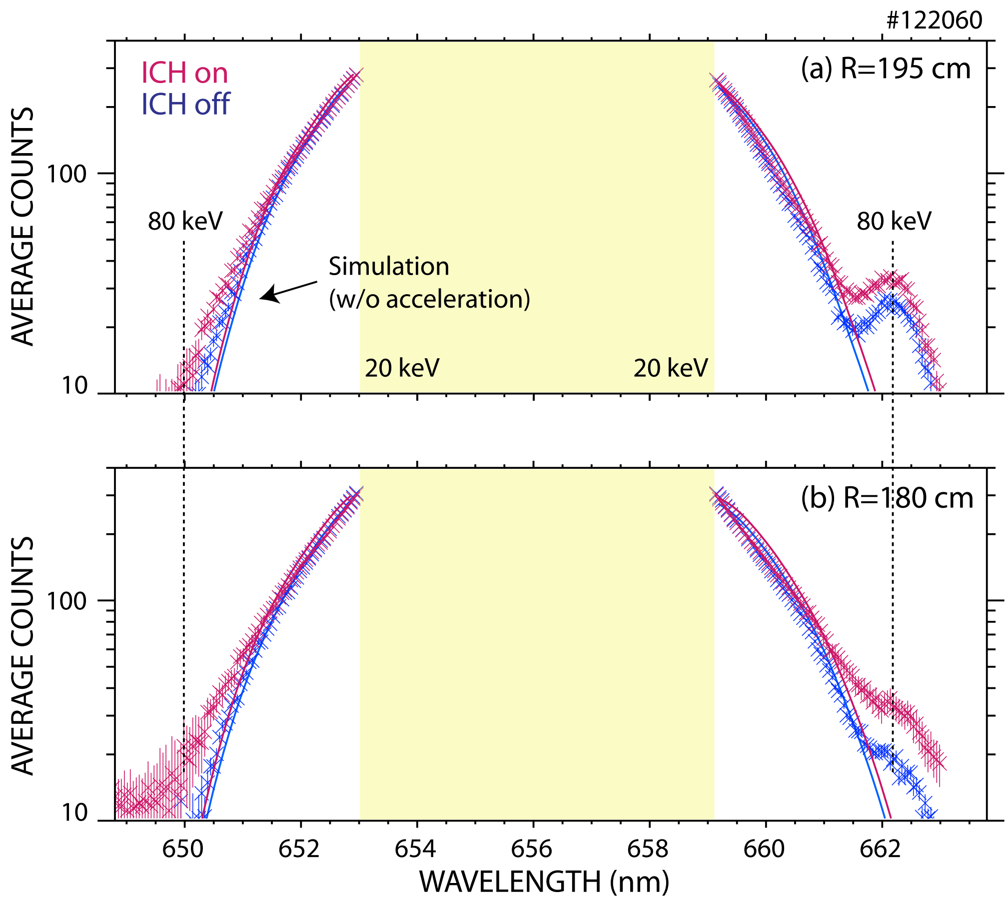

Figure 6.3: Average FIDA spectra (symbols) with and without ICH for the channels at (a) $R = 195$ cm and (b) 180 cm in the discharge shown in Fig. 6.2 between 2250-2500 ms and 1700-2000 ms, respectively. The solid lines show the spectra predicted by the FIDA simulation code for the TRANSP fast-ion distribution function calculated in the absence of ICH acceleration. The dotted vertical lines indicate the wavelengths that correspond to $E_\lambda = 80$ keV. The FIDA simulation only treated the portion of the fast-ion distribution function with energies above 20 keV. Although the most prominent impurity lines have already been fitted and removed from the spectra [25], an impurity line at 662.15 nm still appears.

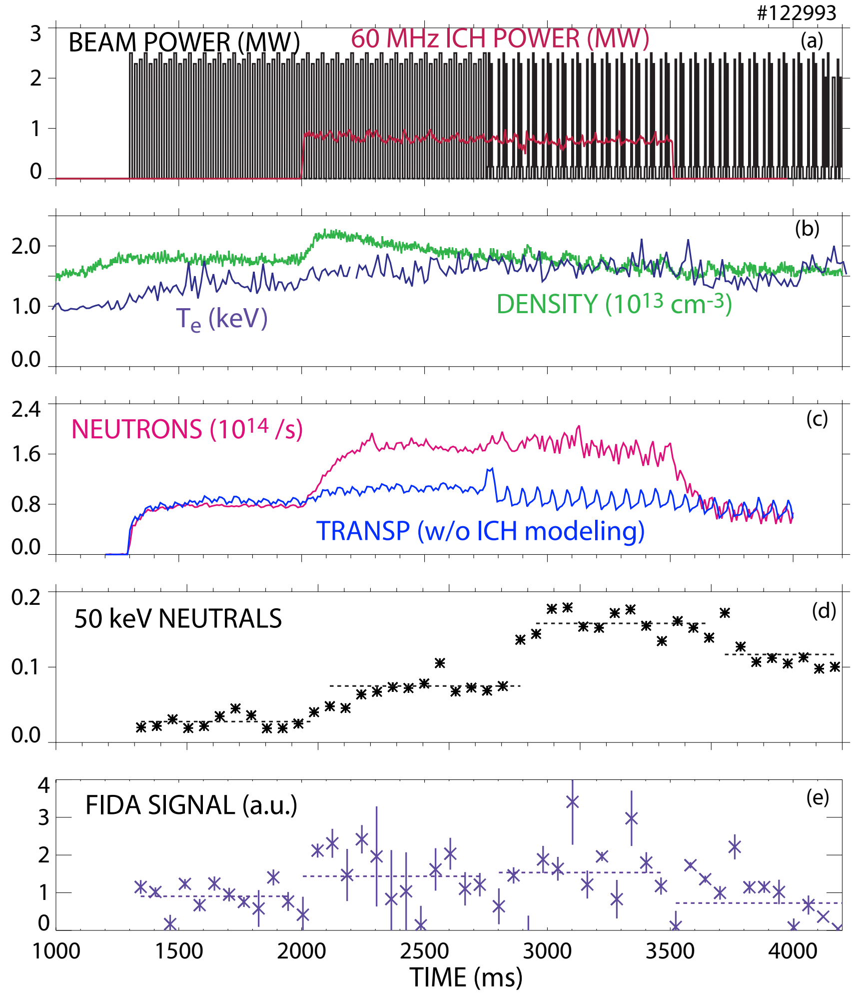

Figure 6.4: Time evolution of (a) the injected neutral beam and coupled ICH power, (b) the central electron temperature and the line-average electron density, (c) the measured neutron rate and the classically expected rate in the absence of ion cyclotron acceleration, (d) the active charge-exchange signal from the vertical NPA (with neutral density and neutral attenuation corrections) and (e) the FIDA density. The more tangential Left beams are injected from 1300-2750 ms, while an equal mixture of Left and Right beams are injected from 2750-4150 ms. The FIDA data are integrated over wavelengths between 649.6-650.8 and 661.3-662.6 nm for the channel that is centered at $R = 179.6$ cm. The dotted lines show the average values of the (d) NPA and (e) FIDA data over the four time periods: Left beams and no ICH, Left beams with ICH, mixed beams with ICH, mixed beams no ICH. $B_T = 1.53$ T; $I_p = 1.0$ MA.

changes.

Measurements of the spatial profile are shown in Fig. 6.5. Consider first the fourth-harmonic discharge shown in Fig. 6.2. In the absence of RF acceleration, very little change in fast-ion pressure is expected during ICH (Fig. 6.5(a)). (The increase in T_e is modest so the slowing-down time barely increases.) Before RF, the measured p_f profile agrees with the TRANSP prediction within estimated experimental error. With ICH, the pressure profile increases significantly in the center of the discharge. For comparison, the relative change in the FIDA density profile is plotted on the same graph using the before-ICH profile as normalization. It should be noted that, because of different weighting in velocity space (Fig. 2.7), the p_f and the FIDA profiles need not be identical, although the difference in relative shape is expected to be small in these conditions. In light of the differences between the quantities, the agreement is excellent.

Figure 6.5 (b) shows spatial profiles in a high density, fourth-harmonic discharge that had very little enhancement in the neutron rate [92]. As before, in the absence of RF acceleration, no significant difference in p_f is expected in the ICH and no-ICH phases but, in this case, the fast-ion pressure profile inferred from the equilibrium hardly changes as well. The FIDA profile (not shown) also hardly changes but has large error bars because of the high density.

The spatial profiles for the fifth-harmonic discharge shown in Fig. 6.4 appear in Fig. 6.5(c). Here, as in the other cases, little change in pressure profile is expected between the ICH and no-ICH phases in the absence of RF acceleration. However, in this case, the measured pressure profile prior to the RF is broader than predicted classically. A likely cause of this broadening is the larger sawteeth in this lower

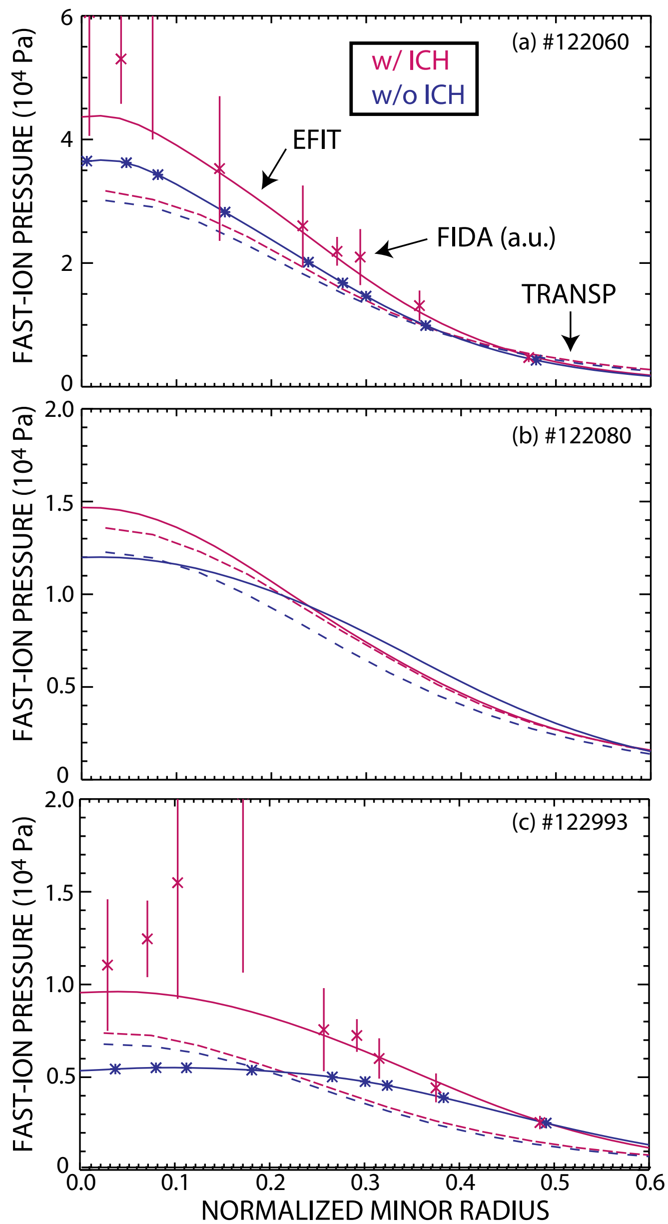

Figure 6.5: Fast-ion pressure inferred from equilibrium analysis (solid line) with and without ICH vs. normalized minor radius ρ. (a) The 4th harmonic discharge shown in Fig. 6.2 at 2285 and 2065 ms. (b) A high-density 4th harmonic discharge at 4450 and 2670 ms. (c) The 5th harmonic discharge shown in Fig. 6.4 at 2445 and 1965 ms. The dashed lines are the fast-ion pressure predicted by TRANSP for classical behavior with ICH acceleration ignored. The symbols represent FIDA density data that are averaged over ~ 200 ms and $E_\lambda = 45$-75 keV; the data are normalized to agree with the pressure profile without ICH.

toroidal field, lower q discharge. (The $q = 1$ surface is at $\rho \simeq 0.28$ prior to the sawtooth crash.) Despite this discrepancy, the enhancement in fast- ion pressure and density associated with RF acceleration is clearly seen by both diagnostics.

Balmer-alpha light can be emitted by hydrogen atoms as well as deuterium atoms. For central fourth-harmonic heating on the deuterium beam ions, parasitic absorption by hydrogen at the second harmonic also occurs. Although the residual hydrogen density in these experiments is quite low (edge spectroscopy indicates that the hydrogen to deuterium concentration is $< 1\%$), a dilute population of hydrogen fast ions probably exists that contributes to the FIDA signal. Empirically, there is no evidence of contamination of the spectrum by hydrogen. Estimates based on calculations of the parasitic hydrogen absorption [22] indicate that hydrogen fast ions may contribute $\lesssim 5\%$ of the signal at $E_\lambda > 50$ keV during fourth harmonic heating. During fifth harmonic heating, any contribution is negligible.

6.2.3 Database corroboration

The discharges from the database (§3.3) with both ICH power and FIDA data are used to investigate systematic trends. In this study, discharges with large tearing modes or appreciable Alfvénic activity are excluded.

When the 60-MHz ICH power exceeds 0.75 MW, the neutron rate usually exceeds the classical prediction (Fig. 6.6). Previous studies showed that a simple zero-dimensional model agrees well with the measured rate in quiet plasmas [18] but not in plasmas with strong Alfvénic activity [95], so this model is used here. For the present database, the neutron rate in discharges with ICH power > 0.75 MW have a fit coefficient that is 50% larger than the discharges with < 0.75 MW of ICH power, confirming that fast-ion acceleration is generally observed.

Figure 6.7 compares the neutron rate with the FIDA density for plasmas with various levels of 60-MHz ICH power. As expected in light of their similar sensitivity in velocity space (Fig. 2.7), the neutron rate correlates well with the FIDA density for values of E_λ that correspond with the bulk of the distribution function (Fig. 6.7(a)). Note that, although a "tail" above the injection energy is clearly evident in the velocity spectra (e.g., Fig. 6.3), the total number of particles above the injection energy is relatively small, so the bulk FIDA density ($E_\lambda > 35$ keV) still correlates well with the neutron rate even when the velocity distribution is distorted. This is not true above the injection energy, however. For large values of E_λ, discharges with over 1.0 MW of ICH power invariably have larger high-energy signals than predicted by the usual (no-ICH) scaling, while discharges with 0.7-1.0 MW occasionally contain a tail (Fig. 6.7(b)).

In a previous study [22], the enhancement of the neutron rate over the classically expected level showed good agreement with a simple model of the 4th harmonic acceleration that depends on the parameter $k_\perp \rho_f$. Here ρ_f is the fast-ion gyroradius at the injection energy and angle and $k_\perp$ is estimated from the Alfvén speed v_A and the wave frequency ω_{RF}, $k_\perp = \omega_{RF}/v_A$. As shown in Fig. 6.8, the neutron data from the 2005 discharges also agree well with this simple model. Note that the neutron rate performs an effective average over the fast-ion distribution function in both velocity and configuration space. The FIDA diagnostic also averages over much of velocity space (Fig. 2.7) but is localized in configuration space. For the database, the FIDA density correlates nearly as well with $k_\perp \rho_f$ as the neutron enhancement (correlation coefficients of $r = 0.82$ and $r = 0.95$, respectively) (Fig. 6.8). In

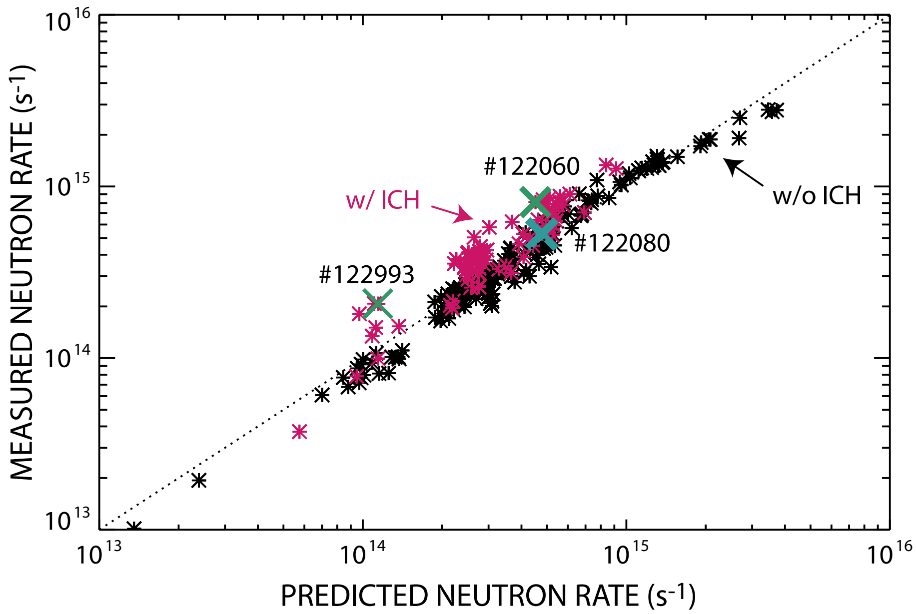

Figure 6.6: Measured neutron rate versus the prediction of a zero-dimensional model [18] for quiet plasmas with over 0.75 MW of ICH power (red) and with less than 0.5 MW of ICH (black). The three discharges selected for detailed analysis are indicated. None of the discharges have tearing or Alfven modes.

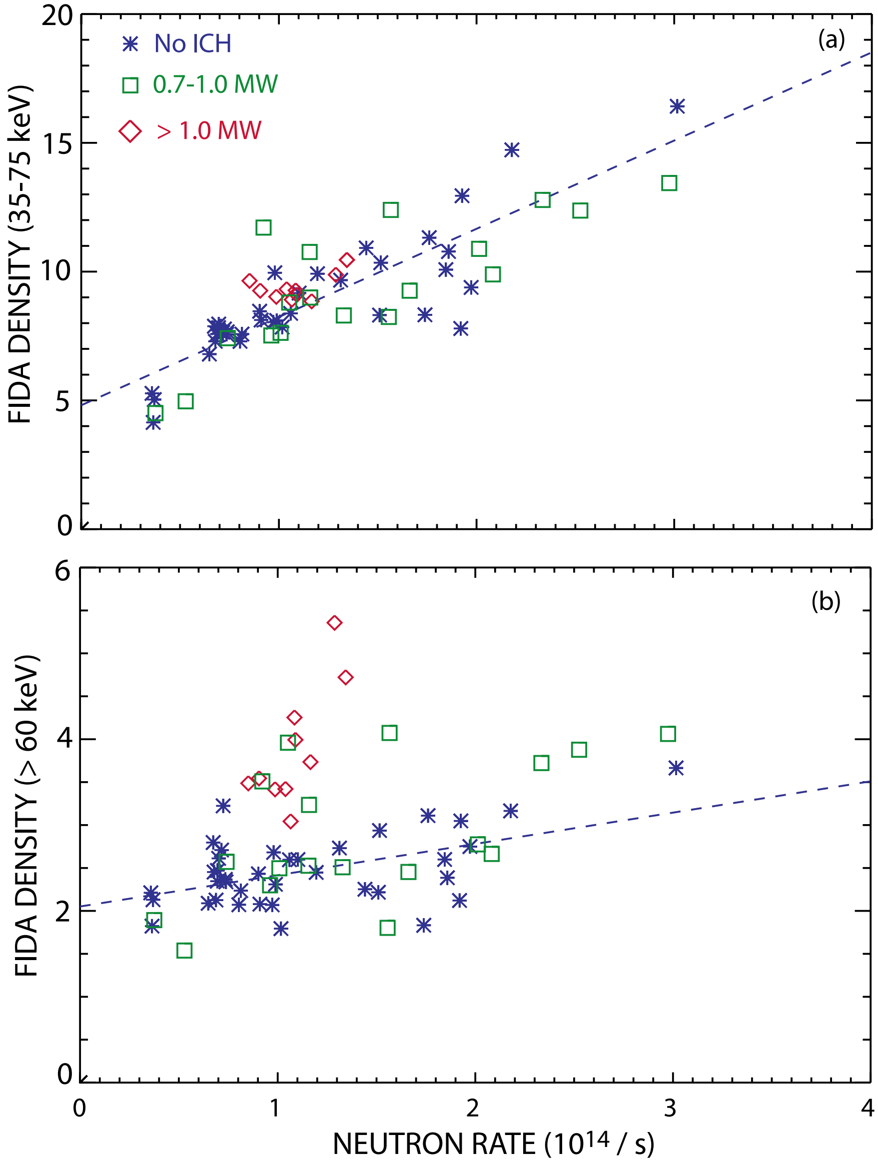

Figure 6.7: FIDA density at R=180 cm averaged over E_λ of (a) 35-75 keV and (b) 60-90 keV versus the neutron rate for 60 MHz ICH power above 1.0 MW (diamond), between 0.7-1.0 MW (square) and without ICH (*). The dashed lines are linear fits to the data in the absence of ICH. $B_t > 1.9$ T; only Left beams.

contrast, the NPA diagnostic is highly localized in both velocity and configuration space and shows virtually no correlation with $k_\perp \rho_f$ ($r = 0.02$ for the six measurements represented by the symbols in Fig. 6.8).

6.3 Comparison with theory

The CQL3D code [96] solves the Fokker-Planck equation for the fast-ion distribution function. In the version of the code employed here, the wave fields in the quasilinear RF operator Q are found using ray tracing (for the antenna parameters in Ref. [22]). The code treats the fast-ion orbits in a zero banana-width approximation and is run for several slowing-down times to obtain a steady-state distribution function with and without RF. The calculated distribution function prior to ICH resembles the TRANSP prediction but is smoother (due to the absence of Monte Carlo noise) and is slightly narrower in pitch (due to the neglect of finite-orbit and charge-exchange effects). To compare with the FIDA data, the distribution functions are mapped into the coordinates used in the FIDA simulation code [23, 26], namely $F(E, p, x, y, z)$, where (x, y, z) are Cartesian coordinates along the neutral beam that produces the FIDA signal. The FIDA simulation code uses F and the computed injected and halo neutral densities in a weighted Monte Carlo scheme to predict the spectral intensity for the nine FIDA channels. For the classical distribution function calculated by TRANSP, this procedure gives good agreement with the measured intensity and spectral shape in quiet plasmas (§5.4).

The analyzed case is the fifth-harmonic acceleration discharge of Fig. 6.4 (#122993). One check of the CQL3D simulation is to compare the enhancement in the neutron rate during ICH with the measured value. The predicted enhancement

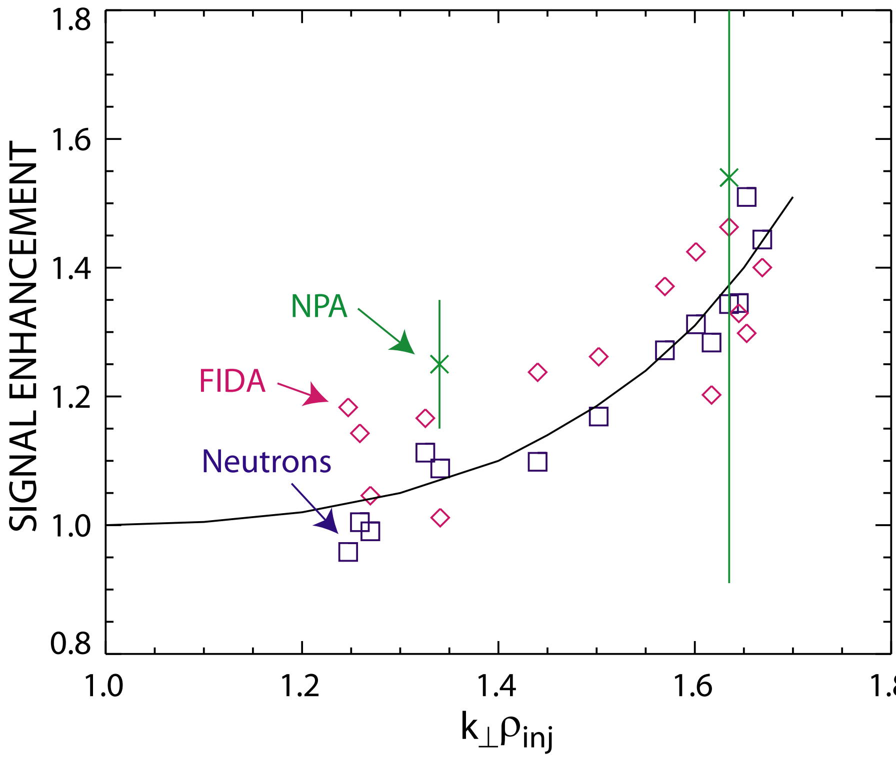

Figure 6.8: Signal enhancement during ICH for the neutron (square), FIDA (diamond), and NPA (x) diagnostics versus the normalized gyroradius of the injected beam ions for all of the 4th harmonic discharges with quiet MHD and > 0.5 MW of 60 MHz ICH in the database. The abscissa employs the approximation $k_\perp \simeq \omega_{RF}/v_A$, with the Alfvén speed evaluated using the line averaged electron density and nominal toroidal field. The solid curve is taken from Ref. [22]. The FIDA data are from the $R = 180$ cm channel and are averaged over $E_\lambda =$ 55-80 keV. The NPA points are the mean and standard deviation of several discharges with the analyzer set to measure neutrals of 50 keV.

is 1.8, while the measured value is 2.2.

The simulated FIDA spectra are similar to the measurements (Fig. 6.9) both before ICH and during ICH. Near the injection energy ($E_\lambda \simeq 50$ keV), both the data and the simulation increase by $\sim 50\%$ during ICH. (Recall from Fig. 2.7 that the signal at $E_\lambda \simeq 50$ keV originates primarily from ions with $E \simeq 80$ keV.) The measured spectral shape during ICH is in reasonable quantitative agreement with the CQL3D prediction: the reduced chi-squared over the energy range $E_\lambda = 40$-70 keV is $\tilde{\chi}^2 = 1.7$. (This calculation neglects the uncertainties in the theoretical prediction associated with uncertainties in plasma parameters, so a value of 1.7 is acceptable agreement.) The agreement is even better if the simulated spectra from a channel 4-cm closer to the resonance layer is selected. As discussed below, because it uses a zero-banana width model, CQL3D predicts that the maximum acceleration occurs closer to the resonance layer than observed experimentally.

In order to determine the radial position of the fast-ion acceleration, Fig. 6.10 shows the enhancement of the FIDA density as a function of major radius. For the fifth-harmonic discharge, the profile peaks about 10 cm farther out in radius than the nominal fifth-harmonic resonance layer. The shift is similar for central fourth-harmonic heating: an average outshift of 8 cm is observed (Fig. 6.10(b)). In earlier work [76], the enhancement in the neutron rate was maximized when the magnetic axis was ~ 5 cm outside of the nominal resonance layer; this shift is consistent with the expected $k_\phi v_\phi$ fast-wave Doppler shift, where k_ϕ is the vacuum toroidal wavenumber and v_ϕ is the toroidal velocity of the injected beam ions. Empirically, the peak in the FIDA spectrum is a few centimeters farther out than

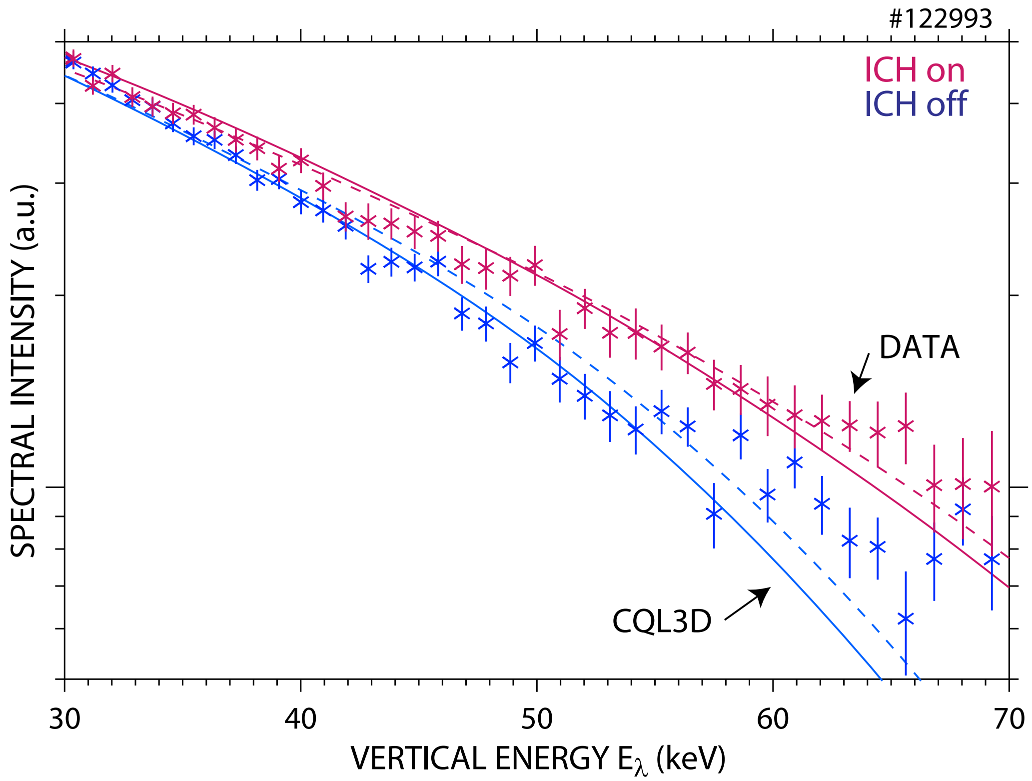

Figure 6.9: Measured (symbols) and calculated (curves) FIDA spectra with (2200-2700 ms) and without (1500-2000 ms) ICH in the fifth-harmonic discharge shown in Fig. 6.4. The CQL3D predictions are for the 180 cm channel (solid) and for the 176 cm channel (dashed); the data are from the 180 cm channel.

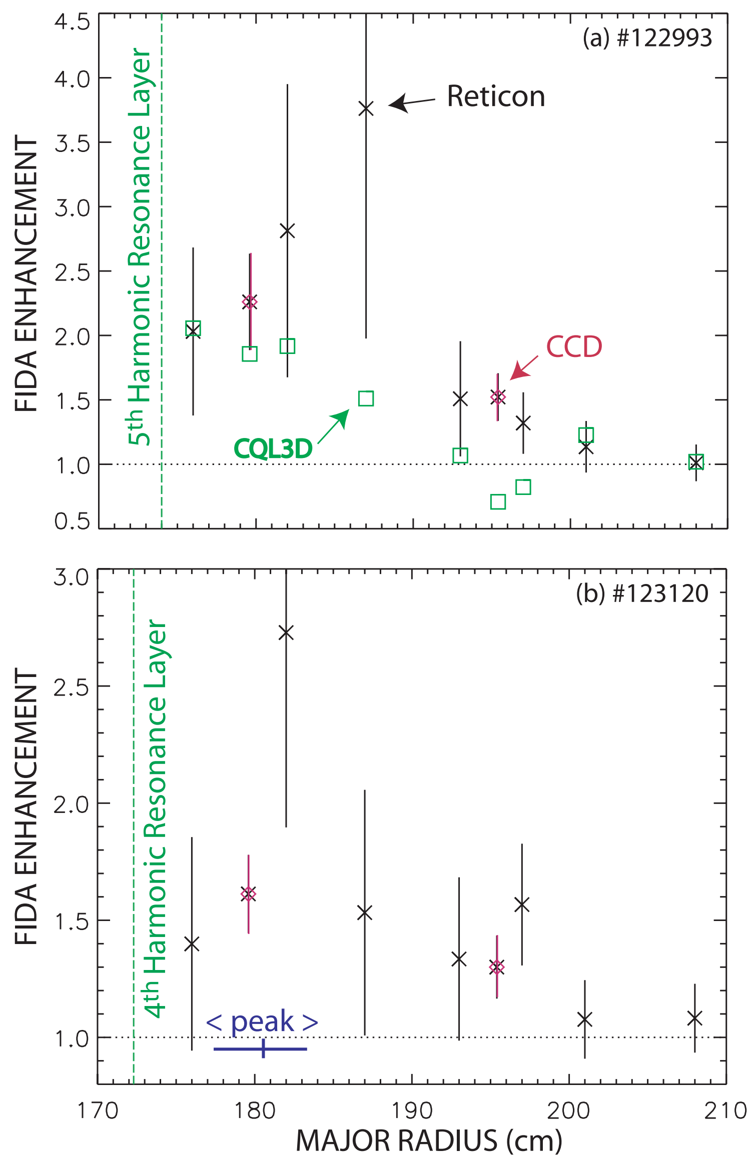

Figure 6.10: Relative change in FIDA density during ICH versus major radius for central (a) fifth harmonic heating and (b) fourth harmonic heating. The data from the dedicated diagnostic (*) are integrated over E_λ = 48-77 keV and the data from the diagnostic that uses Reticon detectors (x) are integrated over wavelengths that correspond to E_λ = 45-65 keV. The solid curves are Gaussian fits to the data. The square symbols are the theoretical predictions of the CQL3D code. The dashed lines represent the nominal resonance layer without fast-wave Doppler shift corrections. In the lower figure, the average and standard deviation of the peak location for five discharges similar to #123120 are indicated by the symbol near 180 cm.

this.

CQL3D predicts a slightly smaller outshift than observed experimentally (Fig. 2.2(a)). The likely explanation for this discrepancy is the zero-banana width approximation in CQL3D. Figure 6.11 shows a collection of particle orbits that have the correct value of vertical velocity to contribute to the observed spectral enhancement at the major radius of maximum FIDA enhancement. These orbits have turning points that are in good agreement with the expected resonance layer (including $k_\phi v_\phi$ fast-wave Doppler shift). In general, because of the nature of banana orbits, accelerated fast ions with turning points at the resonance layer must have an average major radius $< R >$ that exceeds the resonance layer. This simple orbital effect appears to account for the outward shift of the FIDA spatial profile.

6.4 Conclusion

Balmer-alpha spectroscopy is a powerful technique for the diagnosis of ion cyclotron acceleration of hydrogenic fast ions. The spectrum is sensitive to the distortion of the velocity distribution. The spatial profile depends on the wave absorption by the fast ions. The FIDA data are consistent with independent neutron and fast-ion pressure profile measurements.

The various fast-ion diagnostics are complementary. General trends, such as the dependence of fast-ion acceleration on $k_\perp \rho_f$, are most apparent in a diagnostic (like the neutron rate) that effectively integrates over all of phase space. For spatial density profiles, effective integration over velocity space (as in the FIDA and p_f techniques) is helpful. On the other hand, for detailed information about which portion of velocity space interacts with the waves, local measurements in velocity

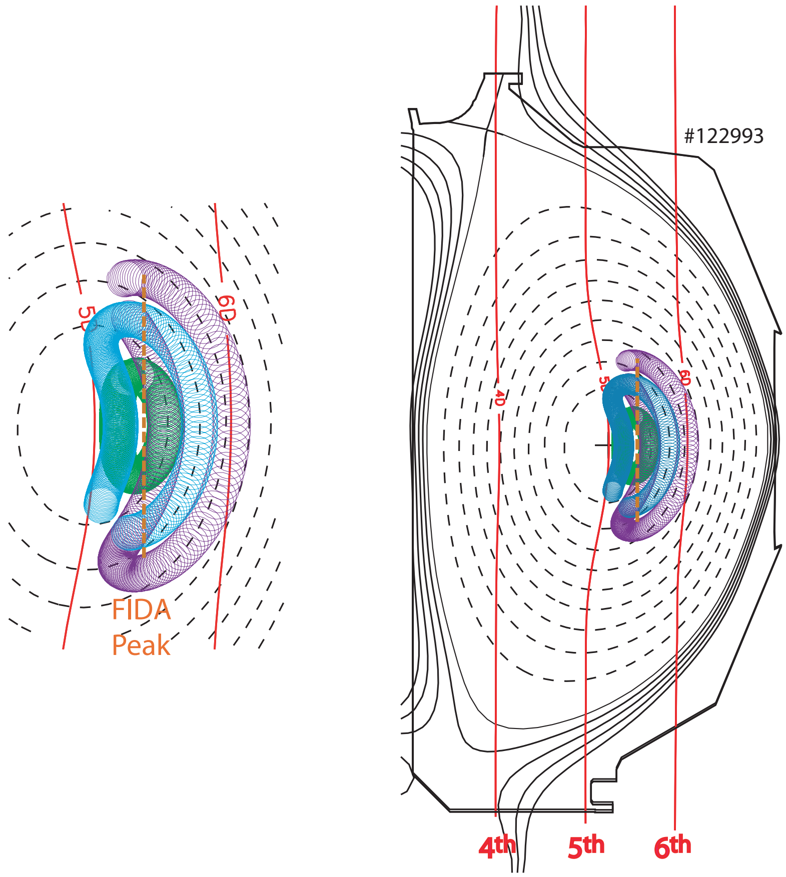

Figure 6.11: Elevation of DIII-D for the discharge shown in Fig. 6.4, showing the projection of representative orbits that have values of v_z that contribute strongly to the observed enhancement of the FIDA signal and are launched from the radial location of the peak of the FIDA enhancement. The dashed lines represent flux surfaces and the solid lines represent the nominal resonance layers (neglecting Doppler shifts).

space by a NPA or similar diagnostic are best.

In light of its zero-banana width model, the CQL3D simulation is in reasonable agreement with the FIDA data. Comparison with the finite banana-width treatment implemented in ORBIT-RF [97] is in progress. In future work, the combination of temporal, spectral, and spatial resolution should allow for stringent tests of theoretical models of wave absorption. A planned experiment will investigate the role of the accelerated fast-ion population in the stabilization and destabilization of "monster" sawteeth.

Chapter 7

Measurements of fast-ion transport by Alfvén eigenmodes

7.1 Introduction

Alpha particles produced in deuterium-tritium fusion reactions may drive Alfvén eigenmodes [98, 99] unstable in ITER and other burning plasma experiments. If they do, the most important practical issue is the resultant fast-ion transport. Will benign local flattening of the alpha pressure profile occur? Or will the alphas escape from the plasma and damage the first wall? The expulsion of fast ions by toroidicity-induced Alfvén eigenmodes (TAE) has damaged internal vessel components in two tokamaks [100, 101]. The damage was explained qualitatively in terms of wave-particle resonances and orbital effects but no quantitative comparisons between the measured fluctuation levels and the expected transport were given in these publications. In the only quantitative studies of this important issue [102, 103], wave amplitudes an order of magnitude larger than the measured values were needed to predict the large losses observed experimentally.

The fast-ion and instability diagnostics were coarse in these early studies, suggesting that misinterpretation of the available signals might account for the discrepancy. In the work reported here, however, both the instabilities and the fast-ion response are very well characterized. Nevertheless, the calculated fast-ion transport is still much smaller than the observed value.

The DIII-D tokamak has an extensive suite of fluctuation diagnostics (Fig. 7.1) with the bandwidth and sensitivity needed to detect Alfvén instabilities [104]. A 40-channel electron cyclotron emission (ECE) diagnostic [5] measures electron temperature (T_e) fluctuations, density (n_e) fluctuations are measured by reflectometry [10], beam-emission spectroscopy (BES) [9], and CO_2 interferometry [105] and magnetic fluctuations are measured by Mirnov coils. A detailed comparison of these measurements with the mode structures predicted by linear ideal MHD theory was recently reported [106, 107]. Both the electron temperature and the electron density eigenfunctions are in excellent agreement with the NOVA code [108] for the $n = 3$ TAE and the reversed-shear Alfvén eigenmode (RSAE). (n is the toroidal mode number.) This chapter documents the fast-ion response to these well-characterized wave fields.

7.2 Data

In the baseline discharge (#122117) (Fig. 7.2), 4.6 MW of 80-keV deuterium neutral beams are injected in the direction of the plasma current into a low-density (2×10^{13} cm^{-3}), diverted, deuterium plasma with T_e = 1-2 keV. The beams are injected early in the current ramp to produce a reversed-shear plasma with an off-axis minimum in the safety factor q at ρ_{qmin}. (The normalized minor radius coordinate is proportional to the square root of the toroidal flux ρ.) The beam pressure is large ($\sim$ 50% of the total) and the ratio of the injected beam speed to the Alfvén speed is ~ 0.45. At the magnetic axis, the peak of the fast-ion distribution function occurs at a pitch of $v_\parallel/v = 0.6$.

The fast-ion response to the instabilities is determined by four independent

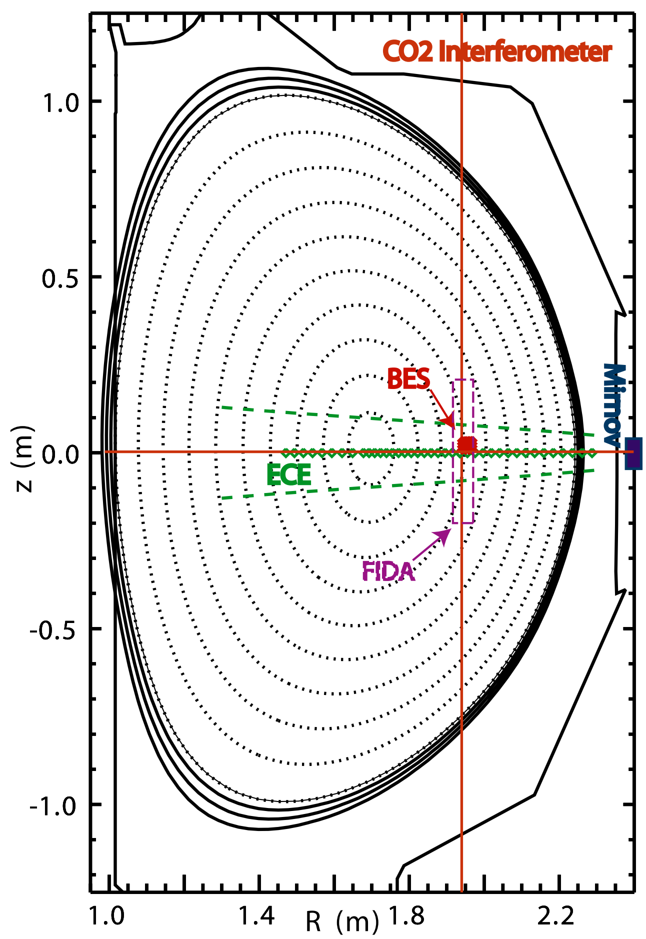

Figure 7.1: Fluctuation diagnostics and a FIDA channel shown in the vertical cross section of DIII-D .

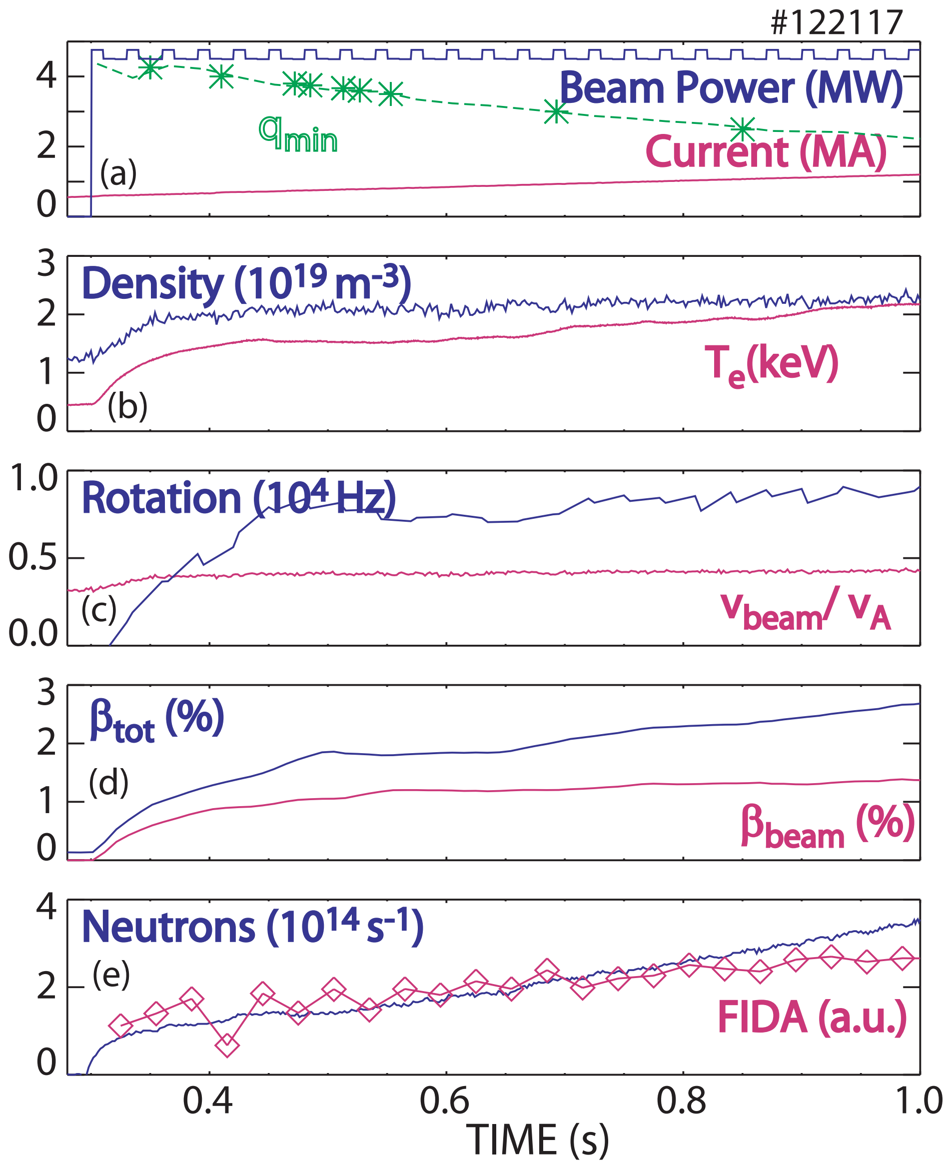

Figure 7.2: Time evolution of (a) beam power, current, and q_{min}, (b) electron density and temperature, (c) rotation and V_{beam}/V_A, (d) β_{tot} and β_{beam}, (e) neutron rate and FIDA signal. The FIDA signal is averaged over E_λ between 30 keV and 60 keV.

techniques. The primary diagnostic is the FIDA diagnostic (Fig. 7.1). Uncertainties in background subtraction are the dominant source of error and are represented by error bars in the figures. In this chapter, the spectra from this FIDA diagnostic are averaged over wavelengths that correspond to energies along the vertical line of sight of $E_\lambda = 30$-60 keV. The wavelength-integrated signals are divided by the injected neutral density (as calculated by a pencil-beam code) to yield fast-ion density measurements in most of the high-energy portion of velocity space [27] with a spatial resolution of a few centimeters. The second diagnostic is the volume-averaged deuterium-deuterium neutron rate S_n. Under these conditions, S_n is dominated by beam-plasma reactions between the fast and thermal populations, so the signal is proportional to the number of high-energy fast ions in the plasma. To detect effects caused by the instabilities, the signal is normalized to the classically expected rate due to collisional processes (as calculated by TRANSP [12]). The third diagnostic is the fast-ion pressure p_f inferred from the equilibrium reconstruction. The absolute uncertainty in the inferred fast-ion pressure at $\rho = 0.25$ is $\sim 16\%$ and the relative uncertainty is $\sim 8\%$. In the fourth technique, the evolution of the q profile provides information on the neutral-beam current drive (NBCD) profile, which is sensitive to the spatial profile of circulating fast ions. In addition to the evolution of q_{min} inferred from the equilibrium reconstructions, rational values of q_{min} are also inferred from the temporal pattern of frequency-sweeping RSAEs with different toroidal mode numbers [99].

Strong Alfvén activity occurs early in the discharge (Fig. 7.3(a)). RSAEs that are localized near ρ_{qmin} and more global TAEs are both observed [106]. When the frequency of a RSAE sweeps across a TAE frequency, the eigenfunctions mix [107].

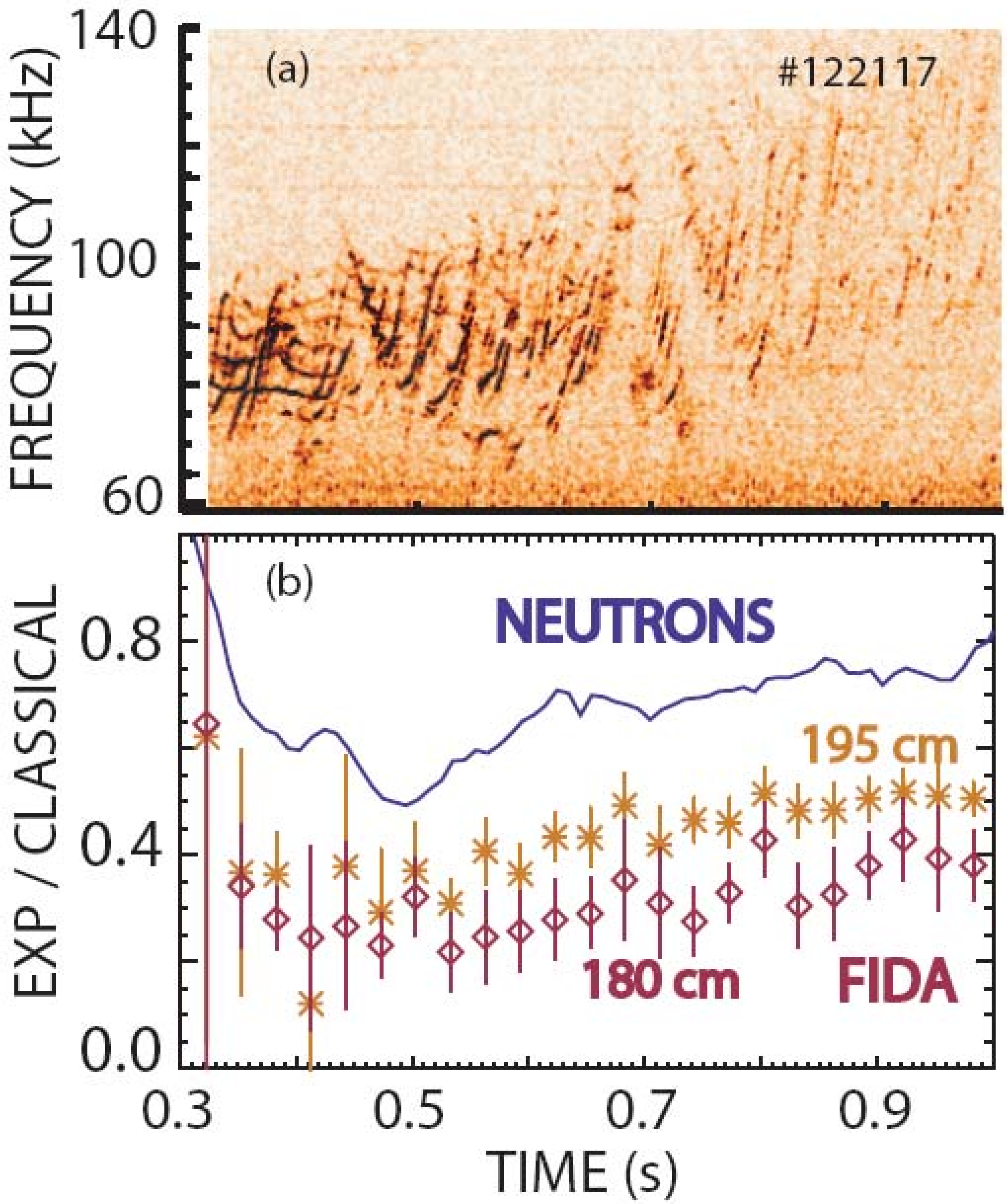

Figure 7.3: (a) Cross-power of radial and vertical CO_2 interferometer channels showing the many RSAEs (upward-sweeping lines) and TAEs ($\sim$ horizontal lines) in the plasma. (b) Neutron rate and FIDA densities at R = 180 and 195 cm vs. time. The signals are normalized by the classical TRANSP neutron and beam-ion density predictions, respectively. The absolute calibrations of the neutron and FIDA data are adjusted so that the ratio is unity in the preceding 2.3 MW discharge at 2.0 s (when the Alfvén activity is undetectable).

Throughout the period of strong activity, both the neutron rate and the FIDA density are suppressed relative to their classically expected values (Fig. 7.3(b)). The magnitude of this suppression correlates with the amplitude of the mode activity. Figure 7.4 shows data from five similar discharges with different values of beam power. Because of the complexity of the Alfvén activity, it is difficult to quantify the composite amplitude. Figure 7.4 uses the amplitude of the ten strongest modes as measured by ECE; the correlation is similar using a bandpass-filtered Mirnov signal. These results strongly suggest that the observed reductions in fast-ion signal are caused by the Alfvén activity.

The Alfvén activity flattens the fast-ion spatial profile. Both the FIDA density profile and the fast-ion pressure profile from MSE are much flatter during the strongest activity than they are later in the discharge (Fig. 7.5). Although the pressure profile peaks as the activity weakens, it is still less peaked than classically expected at 1.2 s. This is in contrast to the profiles observed in MHD-quiescent plasmas, which are in excellent agreement with the TRANSP predictions (§5.4).

The FIDA spectrum is sensitive to the perpendicular energy distribution; distorted spectra are sometimes observed during Alfvén activity and are common during ion cyclotron heating (Fig. 6.3). In discharge #122117, however, the spectra agree (within the uncertainties) with the spectral shape normally observed in quiet plasmas. This suggests that the transport process changes the average perpendicular energy of the fast ions no more than ~ 5 keV.

In the presence of this fast-ion transport, the plasma current diffuses more gradually than classically predicted (Fig. 7.6(a)). Two independent measurements of the evolution of q_{min} are in excellent agreement. They differ markedly from the

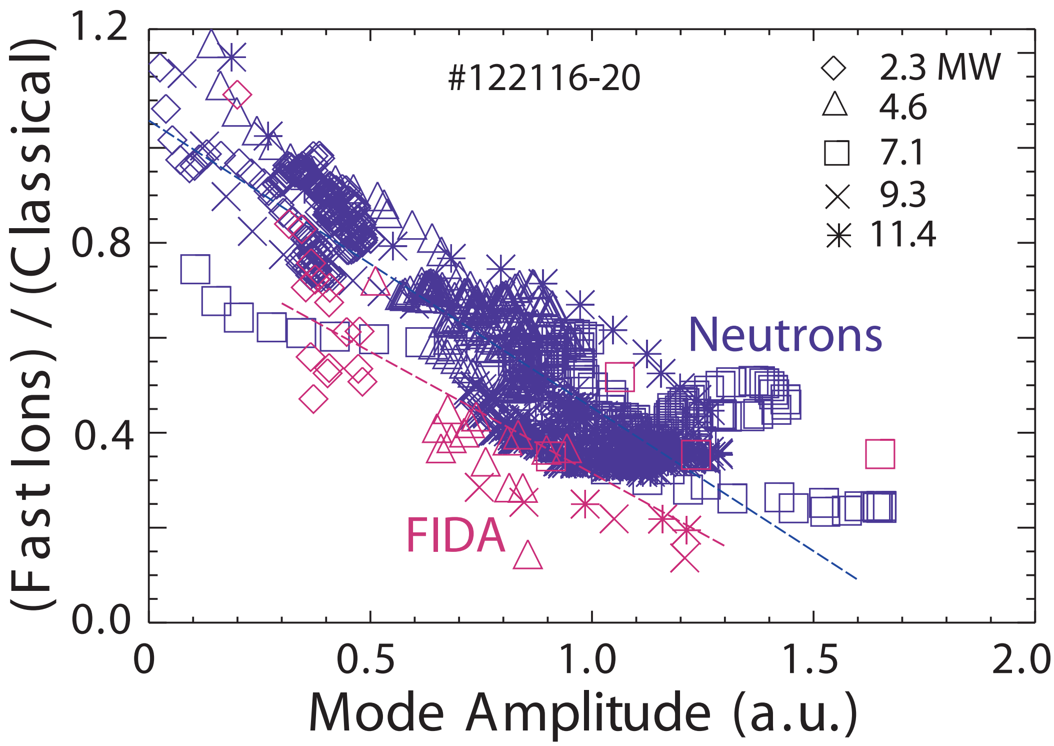

Figure 7.4: Normalized neutron rate and R=180 cm FIDA density versus approximate mode amplitude at various times in five successive discharges with increasing amounts of beam power. The mode amplitude is obtained by summing the amplitudes of the ten largest modes measured by the ECE diagnostic in the frequency band above 50 kHz. The dashed lines are linear fits to the data.

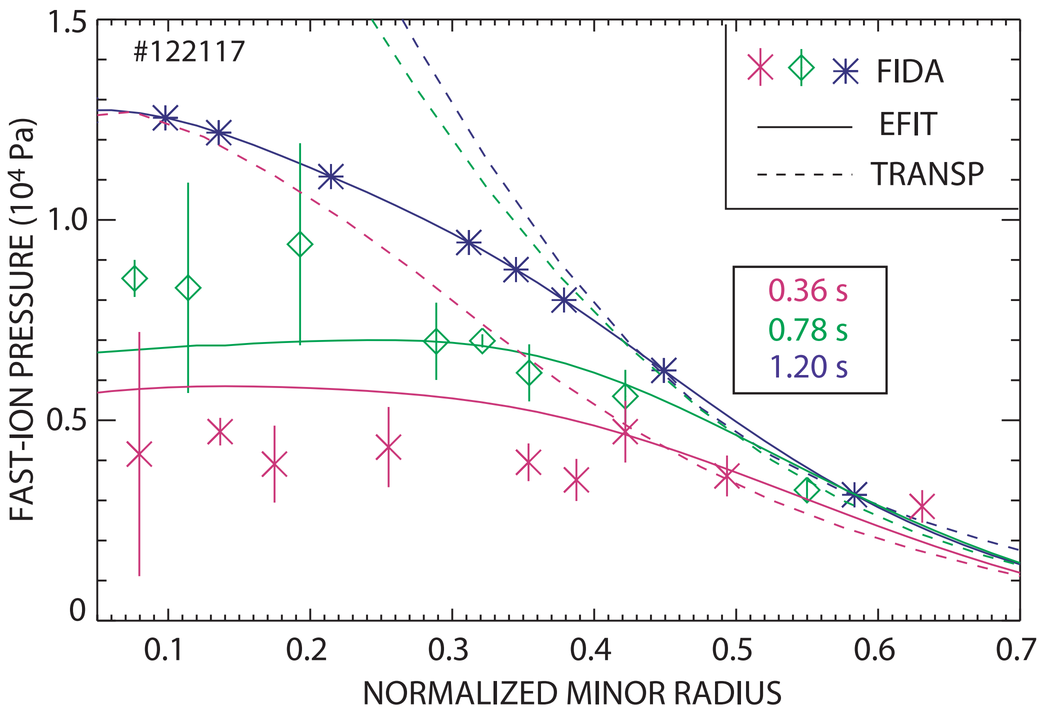

Figure 7.5: Fast-ion pressure profiles and FIDA density profiles versus ρ at three different times that correspond to normalized neutron rates of 0.66, 0.72, and 0.94. The dashed lines are the classical pressure profile predicted by TRANSP. The FIDA density profile is normalized to the MSE-EFIT p_f profile at 1.2 s.

classical predictions calculated by special TRANSP simulations that begin with the measured equilibrium, then evolve the current profile assuming neoclassical flux diffusion. These simulations adjust the boundary value of the parallel electric field to match the measured plasma current. For either of two extreme assumptions–either classical NBCD or no NBCD whatsoever–the predicted diffusion is far more rapid than experimentally observed because both the classical NBCD profile and the neoclassical conductivity profile are more peaked than the actual current profile. It is likely that redistribution of circulating fast ions toward the half radius broadens the NBCD profile and slows the current diffusion; however, modeling with flattened fast-ion density profiles (like those in Fig. 7.5) suggests that an additional source of off-axis current is also required. Gradual evolution of q_{min} was previously reported [109] in more poorly diagnosed discharges. In contrast, in the discharge with lower beam power and much weaker Alfvén activity, the current evolution is close to the classical expectation (Fig. 7.6(b)).

7.3 Comparison with theory

The strongest modes in the spectrum (Fig. 7.3(a)) have peak magnetic perturbations of $\delta B/B \sim 7 \times 10^{-4}$. Published theoretical simulations of fast-ion transport generally require larger amplitudes than this to obtain significant transport; see, e.g., Refs. [102, 103, 110]. To determine if the measured Alfvén activity can explain the observed fast-ion transport, the eleven strongest toroidal modes are matched to NOVA linear eigenfunctions and the amplitudes are scaled to agree with the ECE measurements. Reliable mode identification is possible for the largest 7-8 modes but is problematic for the weakest ones or for modes with similar frequencies. For each

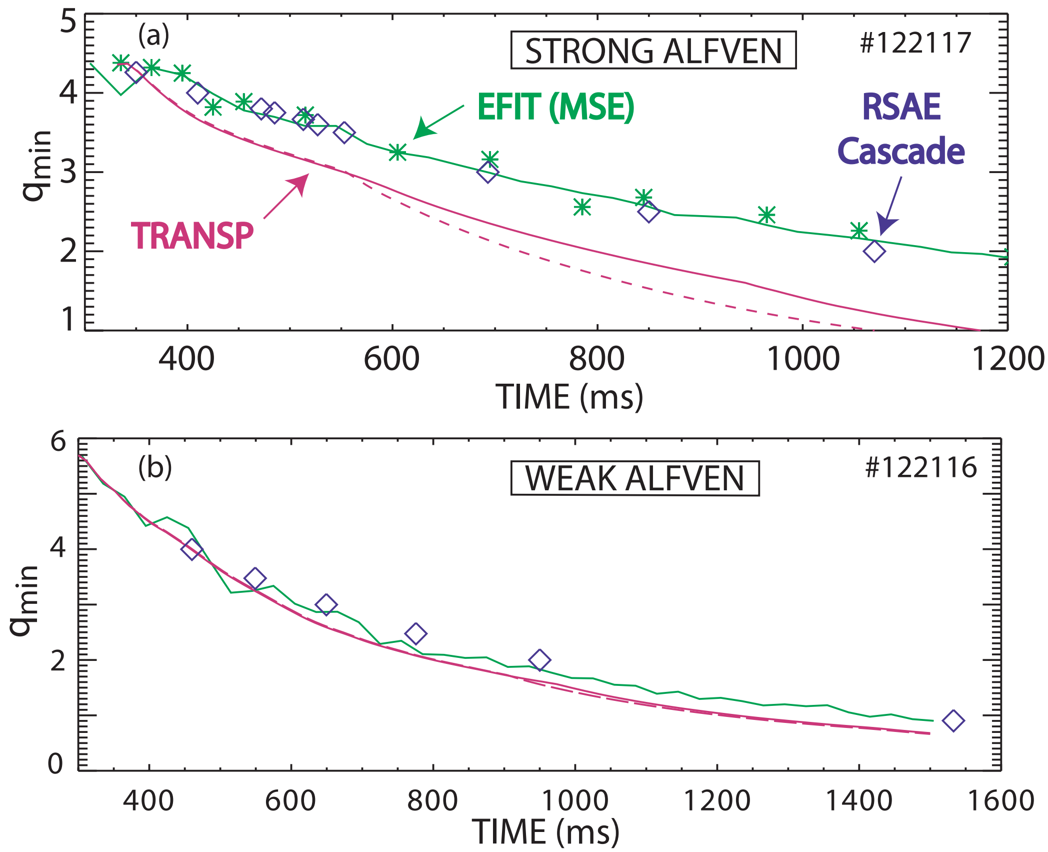

Figure 7.6: Measured evolution of q_{min} from MSE-based equilibrium reconstructions (line) and RSAE rational integer crossings (diamond) in (a) a discharge with strong Alfvén activity (4.6 MW) and (b) weak Alfvén activity (2.3 MW). The TRANSP simulations assume either classical NBCD (solid) or no NBCD (dashed).

toroidal mode, the strongest poloidal harmonics m are selected and a total of 151 (n, m) helical perturbations with their experimental amplitudes and frequencies are entered into the Hamiltonian guiding center code ORBIT [111]. The initial fast-ion birth distribution function F_0 is taken from TRANSP. The particle orbits are computed in the presence of pitch-angle scattering and the perturbed fields, then the distribution function F is sampled for comparison with F_0.

This procedure cannot account for the observed fast-ion transport. Figure 7.7 shows the change in the distribution function in the region of velocity space that makes the dominant contribution to the measured fast-ion signals for ORBIT runs where the mode amplitudes are artificially enhanced by a factor of five. Even with this enormous enhancement, which is much larger than the experimental uncertainty of $\lesssim$10%, the transport is smaller than observed. To estimate the experimental transport, an *ad hoc* diffusion coefficient D_B is employed in a sequence of special TRANSP runs that hold all other plasma parameters fixed. Spatially variable diffusion that is very large ($\gtrsim$5 m^2/s) inside $\rho \simeq 0.55$ and tiny outside is needed for consistency with the measured FIDA and p_f profiles. The ORBIT simulations predict transport in the correct locations but, even with five times the measured amplitude, the change in the distribution function is far too small. The predicted transport is comparable to neoclassical diffusion.

The ORBIT simulation uses the strongest modes observed experimentally. However, many weaker intermittent modes appear at lower frequencies; perhaps these play an important role in the observed transport.

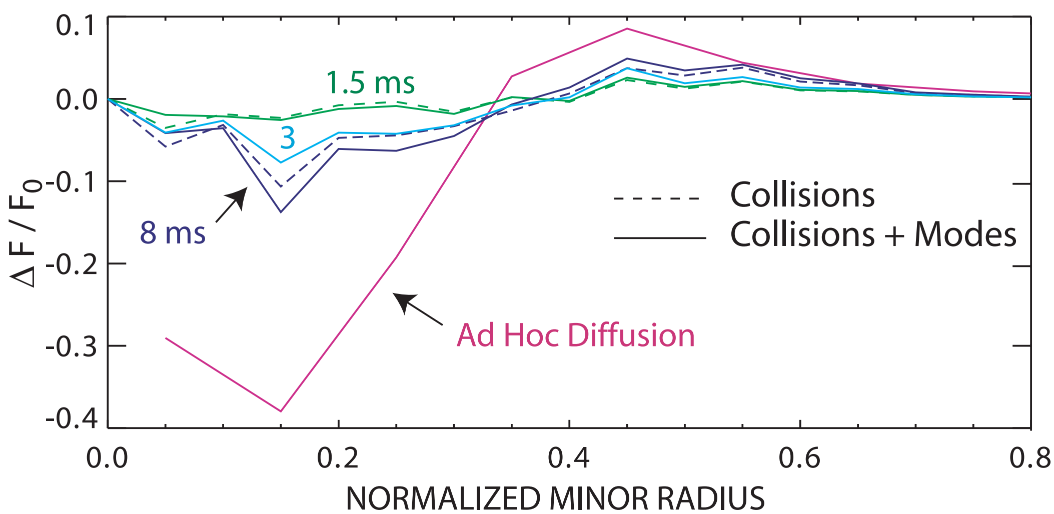

Figure 7.7: Change in the distribution function of fast ions with $E \geq 60$ keV and $v_{\parallel}/v = 0.4$-0.7 vs. ρ; ΔF is normalized to the maximum value of the intial distribution function, which occurs at $\rho = 0.15$. The dashed lines are with collisions alone; the solid lines include collisions and 151 helical modes at five times the experimental amplitudes for the TAEs and RSAEs that are observed at 0.41 s.. The distribution function is sampled after 0.95-1.9 ms (green), 1.9-3.8 ms (turquoise), and 5.5-11 ms (purple). The red curve compares a TRANSP simulation with $D_B = 5$ m^2/s inside $\rho = 0.55$ and zero outside with a standard ($D_B = 0$) simulation. To approximate the conditions of the 8-ms ORBIT simulation, F is evaluated for $E > 66\ keV$, since an 80-keV deuteron slows down to 66 keV in 8 ms under these conditions.

7.4 Conclusion

In summary, four independent diagnostics all indicate strong transport of fast ions in reversed-shear discharges with multiple TAE and RSAE modes that have $\delta B/B = O(10^{-4})$. In quiet plasmas, these same diagnostics agree with classical (§5.4) and ion cyclotron (Chapter 6) theory. Moreover, similar profiles are measured with different techniques during Alfvén activity on JT-60U [112]. The mode amplitudes are also measured by four independent diagnostics [106]. The hypothesis that diagnostic inadequacies account for the discrepancy between theory and experiment is therefore excluded. Fast-ion transport is remarkably effective in plasmas with Alfvén activity. Identification of the mechanism responsible for this transport is an urgent task in burning plasma physics.

Chapter 8

Conclusions

8.1 Summary

The FIDA diagnostic measures the D_α spectrum produced by reneutrals born in charge exchange events with injected neutrals and halo neutrals. In real space, it is a localized measurement with the observational volume defined primarily by the intersection of the viewing line with the neutral beam. In velocity space, it is a one-dimensional measurement. A collection of fast ions in pitch and energy space can contribute to each specific wavelength. The dedicated diagnostic consists of a collection lens, optical fibers, a spectrometer, a blocking bar, two camera lenses, and a CCD camera. The main challenges of this diagnostic is to avoid the bright D_α interferences from other neutral sources and remove the contaminants in the spectrum. In the current system, vertical views are used to minimize the impact of the emission from injected neutrals on the spectrum. A bar at the exit focal plane of the spectrometer blocks the bright interferences in the middle of the spectrum. Background subtraction through beam modulation eliminates visible bremsstrahlung, scattered light, and non charge exchange impurity lines. The impurity lines excited by charge exchange and halo emissions are fit and removed. The current system has an energy resolution of ~ 10 keV, a spatial resolution of ~ 4 cm, and a time resolution of ~ 1 ms. The energy resolution of the FIDA diagnostic is primarily determined by line broadening associated with the motional

Stark effect and the slit width of the spectrometer. The spatial resolution is determined by the distance between the chords. The spatial resolution can be improved to ~ 1 cm, which is the intrinsic spatial resolution, if more chords are installed. The time resolution is the integration of the camera. The various fast-ion diagnostics are complementary and FIDA is a great addition to the existing diagnostics.

It is theoretically impossible to convert the FIDA spectrum to a fast-ion distribution function. Nevertheless, for a specific fast-ion distribution function, the FIDA spectrum can be predicted. This is achieved through the FIDA simulation code, which allows us to compare the FIDA measurements with various fast ions models in different plasma conditions, for instance, TRANSP in quiet plasmas and CQL3D for fast-ion acceleration by ICH. The magnitude of the simulated FIDA signal is very sensitive to uncertainties in electron density profile and electron temperature profile. A $\sim 10\%$ uncertainty in electron density can lead to a $15\% - 20\%$ uncertainty in the simulated signal magnitude. The uncertainties in plasma parameters are probably the primary cause of the discrepancies between simulation and measurements. The shape of the simulated spectrum is relatively insensitive to plasma parameters, which explains the excellent shape agreement between the simulation and the measurement in §5.2.

The FIDA diagnostic is extensively benchmarked in quiet plasmas, where the behaviour of fast ions is well understood. Absolute comparison between the simulation and measurements has excellent shape agreement and reasonable magnitude agreement confirming the validity of the Coulomb collision model in TRANSP in quiet plasmas and the FIDA simulation code. The parametric dependencies of the FIDA signals are as classically expected. The neutron diagnostic and NPA corroborate the FIDA measurements.

The FIDA spectral shape depends on the fast-ion velocity distribution. For vertical views, the spectral shape is very sensitive to the perpendicular energy of fast ions. Therefore, the FIDA diagnostic is a powerful technique for the diagnosis of ion cyclotron acceleration of fast ions. The spectral shape distortion induced by fast-ion acceleration agrees well with the simulated spectrum based on the fast-ion distribution from CQL3D. In discharges with Alfvén activities, the FIDA spectral shape can be distorted as a result of transport when the fast-ion velocity distribution varies substantially at different locations.

The FIDA spatial profiles are measured in various plasma conditions. The absolute profile is currently problematic, probably due to coarse and inconsistent intensity calibration data for the dedicated diagnostic and the Reticon system. The FIDA relative spatial profile, which measures the relative change at different times, agrees very well with the simulated relative profile in quiet plasmas. During ICH, the relative FIDA profile is in reasonable agreement with both the fast-ion pressure profile and the simulated FIDA profile based on the fast-ion distribution from CQL3D. In discharges with Alfvén activities, flattening of the FIDA spatial profile is observed, which is consistent with the fast-ion pressure profile.

8.2 Lessons learned and future work

For the dedicated diagnostic, the signal level is adequate. The systematic errors usually dominate the random errors. Consequently, stronger signal will not improve the SNR much. However, in the high energy range (around the injection energy and above), the random errors can match or even dominate the systematic errors. The high energy range becomes important while studying cyclotron acceleration of fast ions. In this case, more signal will improve the SNR and be beneficial. The Reticon system has a narrow slit width and low quantum efficiency detector. The signal level is low and should be improved. Besides using a CCD camera and broader slit width, the most effective way to increase the signal level is to equip the system with a low f/number collection lens. For example, a f/1.8 collection lens would increase the signal by a factor of 6 compared to a f/4.4 collection lens.

The spectral resolution of the FIDA diagnostic is primarily determined by line broadening associated with the motional Stark effect and the slit width of the spectrometer. Because of the limitation from the motional Stark effect, the slit should be opened to a point where the spectral resolution induced by the motional Stark effect is comparable to that caused by the finite slit width. This would enable more light to be collected while there is little degradation of the spectral resolution.

The current system shows that with vertical views, the blue shift side and the red shift side are very similar and the blue shift side has less contaminations by impurity lines. In future designs, the blue shift side can be measured alone. As a result, a rich set of views becomes usable as long as the emission from the neutral beam has no Doppler shift or is red shifted. In the views comparison study, we have shown that views should be chosen to be as close to the initial fast-ion pitch angle as possible.

The biggest challenge of the FIDA diagnostic is that the background changes in transient plasmas, resulting in a systematic error in the background subtraction. The background consists of visible bremsstrahlung and scattered light that is mainly from edge cold D_α . On the one hand, the scattering should be minimized in future designs. A spectrometer with less scattering is preferred and the blocking bar should be covered with more absorbent material. On the other hand, visible bremsstrahlung and scattered light should be monitored independently along the same sightline. Vissible bremsstrahlung can be measured at somewhere above the injection energy where there is no fast-ion signal. The edge D_α from the same sight line can be measured after it is attenuated by a filter. With the backgrounds from the exact same sight line monitored, we can do dynamic background subtraction that can dramatically improve the capability of the FIDA diagnostic.

The absolute spatial profile is currently problematic. A single system with careful intensity calibration would enable us to measure the absolute spatial profile, which would allow us to make more comprehensive comparisons.

CQL3D assumes zero banana-width, which might cause the discrepancy of the comparison. In the future, ORBIT-RF with the finite banana-width will be used. The combination of temporal, spectral, and spatial resolution should allow for stringent tests of theoretical models of wave absorption.

The mechanism responsible for fast-ion transport induced by Alfvén activities is unclear now. Nevertheless, the FIDA diagnostic and its companion simulation code can provide an excellent test for theoretical models in the future.

Bibliography

[1] http://fusioned.gat.com/images/pdf/what_is_fusion.pdf .

[2] http://en.wikipedia.org/wiki/Tokamak .

[3] LUXON, J. E. A., in Plasma physics and Controlled Nuclear Fusion Research 1986 (Proc. 11th Int. Conf. Kyoto, 1986), Vol.1, IAEA, Vienna (1986) P159. .

[4] BOIVIN, R. L., LUXON, J. L., AUSTIN, M. E., et al., **48** (2005) 834.

[5] AUSTIN, M. E. and LOHR, J., Rev. Sci. Instrum. **74** (2003) 1457.

[6] CARLSTROM, T. N., CAMPBELL, G. L., DEBOO, J. C., et al., Rev. Sci. Instrum. **63** (1992) 4901.

[7] CARLSTROM, T. N., AHLGREN, D. R., and CROSBIE, J., Rev. Sci. Instrum. **59** (1998) 1063.

[8] GOHIL, P., BURRELL, K. H., GROEBNER, R. J., and SERAYDARIAN, R. P., Rev. Sci. Instrum. **61** (1990) 2949.

[9] GUPTA, D. K., FONCK, R. J., MCKEE, G. R., SCHLOSSBERG, D. J., and SHAFER, M. W., Rev. Sci. Instrum. **75** (2004) 3493.

[10] WANG, G., PEEBLES, W. A., RHODES, T. L., et al., Nucl. Fusion **46** (2006) S708.

[11] RICE, B. W., NILSON, D. G., and WROBLEWSKI, D., Rev. Sci. Instrum. **66** (1995) 373.

[12] BUDNY, R. V., Nucl. Fusion **34** (1994) 1247.

[13] LAO, L. L., ST. JOHN, H., STAMBAUGH, R. D., KELLMAN, A. G., and PFEIFFER, W., Nucl. Fusion **25** (1985) 1611.

[14] HEIDBRINK, W. W. and SADLER, G. J., Nucl. Fusion **34** (1994) 535.

[15] GOLDSTON, R. J. and RUTHERFORD, P. H., Introduction to Plasma Physics, Institution of Physics Publishing, London (2000).

[16] HEIDBRINK, W. W., GORELENKOV, N. N., and MURAKAMI, M., Nucl. Fusion **42** (2002) 972.

[17] BINDSLEV, H., HOEKZEMA, J. A., EGEDAL, J., et al., Phys. Rev. Lett. **83** (1999) 3206.

[18] HEIDBRINK, W. W., TAYLOR, P. L., and PHILLIPS, J. A., Rev. Sci. Instrum. **68** (1997) 536.

[19] CAROLIPIO, E. M. and HEIDBRINK, W. W., Rev. Sci. Instrum. **68** (1997) 304.

[20] RICE, B. W., NILSON, D. G., BURRELL, K. H., and LAO, L. L., Rev. Sci. Instrum. **70** (1999) 815.

[21] PETTY, C. C., FOREST, C. B., PINSKER, R. I., et al., Fast wave current drive in neutral beam heated plasmas on diii-d, in *Radio Frequency Power in Plasmas (Proc. 12th International Conference (Savannah, 1997)*, p. 225, New York, 1997, AIP.

[22] HEIDBRINK, W. W., FREDRICKSON, E., MAU, T. K., et al., Nucl. Fusion **39** (1999) 1369.

[23] HEIDBRINK, W. W., BURRELL, K. H., LUO, Y., PABLANT, N. A., and RUSKOV, E., Plasma Phys. Controlled Fusion **46** (2004) 1855.

[24] LUO, Y., HEIDBRINK, W. W., and BURRELL, K. H., Rev. Sci. Instrum. **75** (2004) 3468.

[25] LUO, Y., HEIDBRINK, W. W., BURRELL, K. H., KAPLAN, D. H., and GOHIL, P., Rev. Sci. Instrum. **78** (2007) 033505.

[26] LUO, Y., HEIDBRINK, W. W., RUSKOV, E., BURRELL, K. H., and SOLOMON, W. M., Phys. Plasmas (2007) submitted.

[27] HEIDBRINK, W. W., LUO, Y., BURRELL, K. H., et al., Plasma Phys. Controlled Fusion **49** (2007) 1457.

[28] HEIDBRINK, W. W., GORELENKOV, N. N., LUO, Y., et al., Phys. Rev. Lett. **73** (2007) submitted.

[29] SKINNER, C. H., STOTLER, D. P., ADLER, H., and RAMSEY, A. T., Rev. Sci. Instrum. **66** (1995) 646.

[30] SERAYDARIAN, R. P., BURRELL, K. H., and GROEBNER, R. J., Rev. Sci. Instrum. **59** (1988) 1530.

[31] MANDL, W., WOLF, R. C., VON HELLERMANN, M. G., and SUMMERS, H. P., Plasma Phys. Controlled Fusion **35** (1993) 1373.

[32] LEVINTON, F. M. et al., Phys. Rev. Lett. **63** (1989) 2060.

[33] RICE, B. W., BURRELL, K. H., LAO, L. L., and LIN-LIU, Y. R., Phys. Rev. Lett. **79** (1997) 2694.

[34] ZARNSTORFF, M. C., LEVINTON, F. M., BATHA, S. H., et al., **4** (1997) 1097.

[35] FONCK, R. J., DUPERREX, P. A., and PAUL, S. F., Rev. Sci. Instrum. **61** (1990) 3487.

[36] COTTRELL, G. A., Nucl. Fusion **23** (1983) 1689.

[37] BEREZOVSKIJ, E. L., BEREZOVSKAYA, M. M., IZVOZCHIKOV, A. B., KRUPIN, V. A., and RANTSEV-KARTINOV, V. A., Nucl. Fusion **25** (1985) 1495.

[38] SVENSSON, J., VON HELLERMANN, M., and KÖNIG, R. W. T., Plasma Phys. Controlled Fusion **43** (2002) 389.

[39] POST, D. E., MIKKELSEN, D. R., HULSE, R. A., STEWARD, L. D., and WEISHEIT, J. C., J. Fusion Energy **1** (1981) 129.

[40] VON HELLERMANN. M. G., CORE, W. G. F., FRIELING, J., et al., Plasma Phys. Controlled Fusion **35** (1993) 799.

[41] GERSTEL, U., HORTON, L., SUMMERS, H. P., VON HELLERMANN, M., and WOLLE, B., Plasma Phys. Controlled Fusion **39** (1997) 737.

[42] MCKEE, G., FONCK, R., STRATTON, B., et al., Phys. Rev. Lett. **75** (1995) 649.

[43] MCKEE, G. R., FONCK, R. J., STRATTON, B. C., et al., Nucl. Fusion **37** (1997) 501.

[44] FONCK, R. J., DARROW, D. S., and JAEHNIG, K. P., Phys. Rev. A **29** (1984) 3288.

[45] HUTCHINSON, I. H., Plasma Phys. Controlled Fusion **44** (2002) 71.

[46] MCKEE, G. R., FONCK, R. J., FENZI, C., and LESLIE, B. P., Rev. Sci. Instrum. **72** (2001) 992.

[47] VON HELLERMANN, M. et al., Rev. Sci. Instrum. **61** (1990) 3479.

[48] HOWELL, R. B., FONCK, R. J., KNIZE, R. J., and JAEHNIG, K. P., Rev. Sci. Instrum. **59** (1988) 1521.

[49] VON HELLERMANN, M., MANDL, W., SUMMERS, H. P., et al., Plasma Phys. Controlled Fusion **33** (1991) 1805.

[50] HEIDBRINK, W. W., Nucl. Fusion **24** (1984) 636, Figure 1a shows 3He anisotropy.

[51] THOMAS, D. M., BURRELL, K. H., GROEBNER, R. J., et al., Rev. Sci. Instrum. **68** (1997) 1233.

[52] http://cow.physics.wisc.edu/ craigm/idl/fitting.html .

[53] LEVENBERG, K., Q. Appl. Math. **2** (1944) 164.

[54] MARQUARDT, D. W., J. Soc. Ind. Appl. Math. **11** (1963) 431.

[55] MARCUS, F. B., ADAMS, J. M., CHEETHAM, A. D., et al., Plasma Phys. Controlled Fusion **33** (1991) 277, Figure 3 and 8. Best evidence for beam-ion redistribution at ST. Beam-beam dominates on axis but only constitutes 1/3 overall with b-t the other 2/3.

[56] MANDL, W., Ph.D. thesis, JET (1992).

[57] EGEDAL, J. and BINDSLEV, H., Phys. Plamsas **11** (2004) 2191.

[58] GIANAKON, T. A., FONCK, R. J., CALLEN, J. D., DURST, R. D., and KIM, J. S., Rev. Sci. Instrum. **63** (1992) 4931.

[59] HTTP://ADAS.PHYS.STRATH.AC.UK/, ADAS.

[60] ANDERSON, H., VON HELLERMANN, M., HOEKSTRA, R., et al., Plasma Phys. Controlled Fusion **42** (2000) 781.

[61] JANEV, R. K., LANGER, W. D., POST JR., D. E., and EVANS JR., K., *Elementary processes in hydrogen-helium plasmas*, Springer-Verlag, Berlin, 1987.

[62] VRIENS, L. and SMEETS, A. H. M., Phys. Rev. A **22** (1980) 940.

[63] JANEV, R. K., BOLEY, C. D., and POST, D. E., Nucl. Fusion **29** (1989) 2125.

[64] LODGE, J. G., PERCIVAL, I. C., and RICHARDS, D., J. Phys. B **9** (1976) 239.

[65] SERIES, G. W., *The spectrum of atomic hydrogen*, Oxford University Press, New York, 1987.

[66] GOLDSTON, R. J., Nucl. Fusion **15** (1975) 651.

[67] MANDL, W., Development of active balmer-alpha spectroscopy at JET, Technical Report JET-IR(92)05, JET, 1992.

[68] FINKENTHAL, D. F., *The measurement of absolute helium ion density profiles on the DIII-D tokamak using charge exchange recombination spectroscopy*, PhD thesis, Univ. of California at Berkeley, 1994.

[69] BIDDLE, A. P. and SPROTT, J. C., Plasma Phys. **23** (1981) 679.

[70] SEKI, T., KUMAZAWA, R., TAKASE, Y., et al., Nucl. Fusion **31** (1991) 1369.

[71] SADLER, G., BARABASCHI, P., BERTOLINI, E., et al., Plasma Phys. Controlled Fusion **34** (1992) 1971.

[72] KIMURA, H., FUJII, T., SAIGUSA, M., et al., Plasma Phys. Controlled Fusion **35** (1993) 845.

[73] KOCH, R., VAN WASSENHOVE, G., VAN EESTER, D., et al., Plasma Phys. Controlled Fusion **37** (1995) A291.

[74] NEMOTO, M., KUSAMA, Y., AFANASSIEV, V. I., et al., Plasma Phys. Controlled Fusion **39** (1997) 1599.

[75] ERIKSSON, L.-G., MANTSINEN, M. J., RIMINI, F. G., et al., Nucl. Fusion **38** (1998) 265.

[76] PINSKER, R. I., BAITY, F. W., BERNABEI, S. N., et al., Experiments on ion cyclotron damping at the deuterium fourth harmonic in diii-d, in *Radio Frequency Power in Plasmas (Proc. 13th International Conference (Annapolis, 1999)*, p. 144, New York, 1999, AIP.

[77] KUSAMA, Y., KIMURA, H., NEMOTO, M., et al., Plasma Phys. Controlled Fusion **41** (1999) 625.

[78] MANTSINEN, M. J., ERIKSSON, L., BHATNAGAR, V. P., et al., Plasma Phys. Controlled Fusion **41** (1999) 843.

[79] PETTY, C. C., BAITY, F. W., DEGRASSIE, J. S., et al., Plasma Phys. Controlled Fusion **43** (2001) 1747.

[80] MANTSINEN, M. J., MAYORAL, M.-L., KIPTILY, V. G., et al., Phys. Rev. Lett. **88** (2002) 105002.

[81] NOTERDAEME, J.-M. et al., Nucl. Fusion **43** (2003) 202.

[82] ROSENBERG, A. L., MENARD, J. E., WILSON, J. R., et al., **11** (2004) 2441.

[83] IVANOV, N. V., KOVAN, I. A., and SOKOLOV, Y. A., Sov. Phys.-JETP **24** (1976) 316.

[84] CHRIEN, R. E., COLESTOCK, P. L., EUBANK, H. P., et al., Phys. Rev. Lett. **46** (1981) 535.

[85] COTTRELL, G. A. and START, D. F. H., Nucl. Fusion **31** (1991) 61.

[86] DARROW, D. S., CHANG, C.-S., ZWEBEN, S. J., et al.

[87] KIPTILY, V. G., CECIL, F. E., et al., Nucl. Fusion **42** (2002) 999.

[88] KIPTILY, V. G. et al., Nucl. Fusion **45** (2005) L21.

[89] BINDSLEV, H., NIELSEN, S. K., PORTE, L., et al., Phys. Rev. Lett. **97** (2006) 205005.

[90] BERNABEI, S., BELL, M. G., BUDNY, R. V., et al., Phys. Rev. Lett. **84** (2000) 1212.

[91] BERNABEI, S., BUDNY, R. V., FREDRICKSON, E. D., et al., Nucl. Fusion **41** (2001) 513.

[92] PINSKER, R. I., PORKOLAB, M., and HEIDBRINK, W. W., E. A., Nucl. Fusion **46** (2006).

[93] CAMPBELL, D. J., START, D. F. H., WESSON, J. A., et al., Phys. Rev. Lett. **60** (1988) 2148.

[94] PHILIPONA, R., DOYLE, E. J., LUHMANN, JR., N. C., et al., Rev. Sci. Instrum. **61** (1990) 3007.

[95] HEIDBRINK, W. W., RUSKOV, E., CAROLIPIO, E. M., et al., **6** (1999) 1147.

[96] HARVEY, R. W. and MCCOY, M. G., in *Proceedings of IAEA Technical Committee Meeting on Advances in Simulation and Modeling of Thermonuclear Plasmas*, Montreal, 1992, IAEA.

[97] CHAN, V. S., CHIU, S. C., and OMELCHENKO, Y. A., **9** (2002) 501.

[98] CHENG, C. Z., CHEN, L., and CHANCE, M., Annals Physics **161** (1985) 21.

[99] SHARAPOV, S. E., ALPER, B., BERK, H. L., et al., **9** (2002) 2027.

[100] DUONG, H. H., HEIDBRINK, W. W., STRAIT, E. J., et al., Nucl. Fusion **33** (1993) 749.

[101] WHITE, R. B., FREDRICKSON, E., and DARROW, D., E. A., Phys. Plasma **2** 2871.

[102] CAROLIPIO, E. M., HEIDBRINK, W. W., CHENG, C. Z., et al., **8** (2001) 3391.

[103] TODO, Y., BERK, H. L., BREIZMAN, B. N., et al., **10** (2003) 2888.

[104] NAZIKIAN, R., BERK, H. L., BUDNY, R. V., et al., Phys. Rev. Lett. **96** (2006) 105006.

[105] VAN ZEELAND, M. A., KRAMER, G. J., NAZIKIAN, R., et al., Plasma Phys. Controlled Fusion **47** (2005) L31.

[106] VAN ZEELAND, M. A., KRAMER, G. J., AUSTIN, M. E., et al., Phys. Rev. Lett. **97** (2006) 135001.

[107] VAN ZEELAND, M. A. et al., **14** (2007) to be submitted.

[108] CHENG, C. Z., Phys. Reports **1** (1992) 211.

[109] WONG, K. L., BUDNY, R., NAZIKIAN, R., et al., Phys. Rev. Lett. **93** (2004) 085002.

[110] SIGMAR, D. J., HSU, C. T., WHITE, R., and CHENG, C. Z., Phys. Fluids B **4** (1992) 1506.

[111] WHITE, R. B. and CHANCE, M. S., Phys. Fluids **27** (1984) 2455.

[112] ISHIKAWA, M., NISHITANI, T., KUSAMA, Y., et al., Plasma and Fusion Research **2** (2007) 19.